Kinetically-Controlled Synthesis of Pd-Cu Janus Nanocrystals with Enriched Surface Structures and Enhanced Catalytic Activities toward CO₂ Reduction

Zhiheng Lyu,^{†,+} Shangqian Zhu,^{¥,+} Lang Xu,^{∥,+} Zitao Chen,[‡] Yu Zhang,^{‡,¥} Minghao Xie,[†] Tiehuai Li,[¥] Shan Zhou,[†] Jingyue Liu,[#] Miaofang Chi,[§] Minhua Shao,^{¥,*} Manos Mavrikakis,^{∥,*} and Younan Xia^{†,‡,*}

[†]School of Chemistry and Biochemistry, Georgia Institute of Technology, Atlanta, Georgia 30332, United States

*Department of Chemical and Biological Engineering, The Hong Kong University of Science and Technology, Clear Water Bay, Kowloon, Hong Kong, China

Department of Chemical and Biological Engineering, University of Wisconsin-Madison, Madison, Wisconsin 53706, United States

[‡]The Wallace H. Coulter Department of Biomedical Engineering, Georgia Institute of Technology and Emory University, Atlanta, Georgia 30332, United States

*Department of Physics, Arizona State University, Tempe, Arizona 85287, United States §Center for Nanophase Materials Science, Oak Ridge National Laboratory, Oak Ridge, Tennessee 37831, United States

^{*}Address correspondence to younan.xia@bme.gatech.edu (for synthesis), kemshao@ust.hk (for electrocatalytic measurement), and manos@engr.wisc.edu (for computational work)

*These authors contributed equally to this work.

Abstract

Bimetallic nanocrystals often outperform their monometallic counterparts in catalysis as a result of the electronic coupling and geometric effect arising from two different metals. Here we report a facile synthesis of Pd-Cu Janus nanocrystals with controlled shapes through site-selected growth by reducing the Cu(II) precursor with glucose in the presence of hexadecylamine and Pd icosahedral seeds. Specifically, at a slow reduction rate, the Cu atoms nucleate and grow from one vertex of the icosahedral seed to form a penta-twinned Janus nanocrystal in the shape of a pentagonal bipyramid or decahedron. At a fast reduction rate, in contrast, the Cu atoms can directly nucleate from or diffuse to the edge of the icosahedral seed for the generation of a singly twinned Janus nanocrystal in the shape of a truncated bitetrahedron. The segregation of two elements and the presence of twin boundaries on the surface make the Pd-Cu Janus nanocrystals effective catalysts for the electrochemical reduction of CO₂. An onset potential as low as -0.7 V_{RHE} (RHE: reversible hydrogen electrode) was achieved for C₂₊ products in 0.5 M KHCO₃ solution, together with a faradaic efficiency approaching 51.0% at -1.0 V_{RHE}. Density functional theory and Pourbaix phase diagram studies demonstrated that the high CO coverage on the Pd sites (either metallic or hydride form) during electrocatalysis enabled the spillover of CO to the Cu sites toward subsequent C-C coupling, promoting the formation of C₂₊ species. This work offers insights for the rational fabrication of bimetallic nanocrystals featuring desired compositions, shapes, and twin structures for catalytic applications.

Introduction

Bimetallic nanocrystals have received ever-increasing interest for their enriched properties and enhanced applications relative to a monometallic system.¹ The involvement of two metals, for example, allows one to enhance the catalytic activity of nanocrystals toward various reactions by leveraging the geometric and ligand effects. Among the different configurations, those with a Janus or side-by-side structure are particularly attractive because both of the metals are presented on the surface. In recent years, seed-mediated and site-selected growth has emerged as one of the most effective routes to the synthesis of bimetallic nanocrystals with a Janus structure.^{2,3} The success in synthesis has led to the development of catalysts with augmented performance. For example, Au nanorods bearing Pt tips at the ends showed a greatly enhanced activity toward the photocatalytic hydrogen evolution reaction (HER) relative to the Au–Pt bimetallic nanocrystals with a core–shell structure.⁴ By spatially confining Pt to the two ends of a Au nanorod, hot electrons could be effectively generated via the excitation of surface plasmons in the Au component and then transferred to the Pt tips for reducing H⁺ to H₂.

While seed-mediated synthesis can be easily and conveniently implemented, it is nontrivial to achieve site-selected growth. In many cases, the lack of an internal or external driving force makes it rather difficult to ensure that the incoming atoms only nucleate and grow from one of the multiple equivalent sites on a seed.² From the point of thermodynamics, it is not favorable to generate the high-index facets and large surface areas typically associated with the products of site-selected growth.⁵ In addition, surface diffusion tends to move the deposited atoms to other regions on the surface of a seed, ruining the pattern of site-selected growth.⁶ A number of strategies have been developed to address these issues, including manipulation of the reduction kinetics of the precursor,^{7,8} partial passivation of the surface of a seed through the use of a capping agent,^{9,10} introduction of oxidative etching,¹¹ and leverage of lattice mismatch between the two metals.¹²

Copper (Cu) and Cu-based nanocrystals have received considerable interest in recent years owing to their outstanding performance in catalysis, as well as the excellent electric conductivity,

high abundance in the Earth's crust, and the low price of Cu.¹³ They have been extensively explored as catalysts toward the electrochemical reduction of CO₂, and Cu is one of the few metals capable of generating appreciable amounts of hydrocarbons, in particular, multicarbon (C₂₊) species such as ethylene and ethanol with high values and large markets.^{14,15} However, current Cu-based catalysts are plagued by problems such as high overpotential, low selectivity, and poor stability. Some of these issues can be addressed by maneuvering the composition, shape, and twin structure of the Cu-based catalysts. For example, it was reported that the presence of planar defects on the surface could strengthen the binding of CO and thereby increase the CO coverage density to promote C–C coupling.¹⁶ Such a modification has led to a high selectivity (52.4%) toward ethylene at –1.0 V_{RHE} (RHE: reversible hydrogen electrode) in 0.1 M KHCO₃ electrolyte. On the other hand, introducing Pd or Ag into Cu in the form of segregated, nanoscale domains was able to improve the selectivity toward ethylene relative to a catalyst based on Cu nanoparticles, demonstrating the important role of both the composition and spatial distribution in determining the performance of a Cu-based catalyst.^{17,18}

Considering the benefits from planar defects and a segregated, bimetallic composition, we sought to develop a class of effective catalysts toward CO₂ reduction by controlling the growth of Cu from Pd icosahedral seeds. The multiple twin defects intrinsic to an icosahedron would be able to direct the deposition of Cu atoms for the generation of twin boundaries on the surface of the resultant Cu nanocrystal.19 The large lattice mismatch (7.1%) between Pd and Cu would favor both site-selected nucleation and island growth, enabling the production of a Pd–Cu nanocrystal featuring a Janus structure.²⁰ It was envisioned that catalysts with such a favorable combination of twin boundaries and segregated composition would exhibit significantly improved activity, selectivity, and onset potential for the formation of C₂₊ products during the electrochemical reduction of CO₂.²¹

Here we report that we could obtain Pd–Cu Janus nanocrystals with different shapes for the Cu component by varying the experimental conditions used for seed-mediated growth involving Pd icosahedra. Specifically, by increasing the concentration of the precursor, the nucleation and

growth of Cu could be shifted from a vertex to an edge of the icosahedral seed for the formation of nanocrystals in the shape of a pentagonal bipyramid, decahedron, or truncated bitetrahedron. The concentration of hexadecylamine (HDA), a stabilizer and a coordination ligand, also played an important role in the seed-mediated synthesis. An increase in HDA concentration favored the formation of pentagonal bipyramids and decahedra, whereas truncated bitetrahedra were obtained at a reduced concentration. The as-synthesized Pd-Cu nanocrystals were evaluated as catalysts toward the electrochemical reduction of CO₂. An onset potential as low as -0.7 V_{RHE}, together with a high selectivity approaching 51.0% at -1.0 V_{RHE}, was achieved for the production of C₂₊ species in a 0.5 M KHCO₃ electrolyte. The performance was greatly improved relative to other catalysts based on Cu (Table S1).²²⁻²⁵ Furthermore, we performed density functional theory (DFT) calculations and constructed Pourbaix phase diagrams to investigate the role of Pd, in either its metallic or hydride form, in the bimetallic catalysts. We demonstrated that a CO coverage exceeding 6/9 monolayer (ML) on Pd(111) or 5/9 ML on the PdH surface was required for CO spillover from Pd to Cu, both clearly achievable under the experimental conditions of the present study. Upon migration to the Cu sites, the CO could undergo C-C coupling for the generation of C₂₊ products.

Results and Discussion

Pd-Cu Janus Nanocrystals with Three Different Shapes. As a highly symmetric object, the surface of an icosahedron is covered by 12 equiv of penta-twinned apexes as the vertices, 30 equiv of twin boundaries as the edges, and 20 equiv of $\{111\}$ facets as the side faces. Figure S1 shows a typical transmission electron microscopy (TEM) image of the as-prepared Pd icosahedral seeds, which had an average size of 12.7 ± 1.3 nm (see Figure S2a for the definition of size). As shown in Figure 1, with them serving as the seeds, we were able to obtain Pd–Cu Janus nanocrystals featuring three distinctive shapes for the Cu component by simply increasing the amount of the Cu(II) precursor involved in the synthesis. Specifically, at a fixed amount of 45 mg for HDA, we obtained Cu nanocrystals in the shapes of a pentagonal bipyramid, decahedron,

and truncated bitetrahedron, respectively, when 1.05, 5.25, and 10.5 mg of CuCl₂ were involved.

Structural characterizations of the Pd-Cu nanocrystals with different shapes are summarized in Figure 2. Analyses of about 180 particles for each shape on the TEM images gave a purity of 72% for the pentagonal bipyramids with an average size of 26.1 ± 2.5 nm, 79% for the decahedra with an average size of 39.3 ± 2.7 nm, and 84% for the truncated bitetrahedra with an average size of 48.2 ± 3.5 nm. The definition of size for each type of nanocrystal can be found in Figure S2, b-d. For the pentagonal bipyramid (Figure 2b), we were able to identify the borderline between Pd and Cu under bright-field scanning TEM (BF-STEM) imaging, confirming a Janus structure for the overall nanocrystal. We also resolved the twin boundaries in the Cu portion, as highlighted by the red dashed lines. A horizontal projection of this penta-twinned nanocrystal is shown in Figure S3, revealing its pentagonal base and twin boundaries. Taken together, it can be concluded that the Cu portion had a pentagonal-bipyramidal shape and a penta-twinned structure. Different from the conventional bipyramids where the two pyramidal portions are related by reflectional symmetry, one side of the as-prepared Cu bipyramid was elongated, while the other side could be hardly seen. In a sense, this new bipyramid had an asymmetric shape similar to that of a light bulb.²⁸ The segregation in composition was further supported by the dark-field (DF) STEM image and energy dispersive X-ray (EDX) mapping data shown in Figure 2, c and d, where the signals for Pd and Cu were spatially separated from each other.

Figure 2f shows a BF-STEM image of the decahedron, in which the five twin boundaries in Cu could be clearly resolved around the Pd seed. Interestingly, the locations of these twin defects were aligned with those in the original Pd icosahedral seed, suggesting that the twin boundaries intersecting the vertex of Pd icosahedron induced the formation of twin defects in Cu. The flat shape, pentagon projection, and penta-twinned structure all pointed toward a decahedral shape for the nanocrystal. According to the DF-STEM image in Figure S4, the Pd seed was located at one of the two axial vertices of the Cu decahedron instead of the center, suggesting that Cu was only grown from one side of the Pd seed to form a Janus structure similar to that of the pentagonal bipyramid. As for the truncated bitetrahedron shown in Figure 2j, the Pd seed was

positioned at one of the three vertices on the equatorial plane. From the side view of a truncated bitetrahedron (Figure S5a), the twin boundary is next to the center of a projected hexagon while passing through the Pd seed, illustrating the singly twinned structure of the nanocrystal. Severe truncation was also observed at two corners along the axis perpendicular to the triangular base. In the [011] direction, the angle of the corner next to the Pd seed was measured to be 55°, indicating that the bipyramid consisted of two truncated tetrahedra placed together by sharing one base. ^{29,30} A close examination of the flat triangular plane reveals that it was terminated in {111} facets, further confirming the truncated-bitetrahedral shape (Figure S5, b–d). Figure 2, h and l, shows EDX mapping of the decahedron and truncated bitetrahedron, confirming the spatial separation between the distributions of Pd and Cu.

Figure S6 shows the X-ray diffraction (XRD) patterns and X-ray photoelectron spectroscopy (XPS) spectra of the Pd–Cu nanocrystals. For the pentagonal bipyramids (Figure S6a), the product containing the highest proportion of Pd, the three peaks positioned at 43.4°, 50.5°, and 74.3° can be attributed to the diffraction from Cu(111), (200), and (220) planes, while the weak peak located at 40° can be assigned to the Pd(111) plane. The separation between the peaks of Cu and Pd further confirmed that these two elements were not mixed together to form an alloy. Different from the case of pentagonal bipyramids, no signal was observed for Pd in the XRD patterns of decahedra and truncated bitetrahedra due to its low content (Figure S6, c and e), while the peaks for Cu were obvious. In the XPS spectra of all three samples, the Cu 2p peaks were observed at 952.0 and 932.0 eV. In Figure S6f, two weak satellite peaks were found at 962.5 and 944.5 eV, which could be attributed to the Cu oxide layer on the surface of the truncated bitetrahedra, a phenomenon commonly observed for Cu-based nanocrystals. 31,32

Figure S7 shows the ultraviolet–visible (UV–vis) spectra recorded from aqueous suspensions of the Pd–Cu nanocrystals. All of them exhibited extinction peaks in the visible region owing to the localized surface plasmon resonance (LSPR) associated with Cu. The spectrum of the decahedra featured two resolvable peaks, corresponding to the transverse and longitudinal modes arising from the anisotropy of the decahedral shape.³³ Different from the

decahedra, only one peak was observed for both the pentagonal bipyramids and truncated bitetrahedra. The former can be attributed to their pseudospherical shape, while the latter might be caused by the high aspect ratio and thus relatively low intensity of the transverse dipole resonance. 32,34-36

Elucidation of the Growth Mechanism. To gain mechanistic insights into the formation of Pd-Cu nanocrystals with three different shapes, we analyzed the products obtained at different stages of each standard synthesis using TEM. Figure 3 shows the shape evolution in the synthesis of Pd-Cu pentagonal bipyramids. Specifically, Cu atoms were generated and initially deposited on one side of the Pd icosahedral seed to take an elliptical shape at t = 30 min (Figure 3a). Due to the large lattice mismatch (7.1%) between Pd and Cu, the Cu atoms preferred to grow from the already deposited Cu instead of the Pd surface, leading to the formation of one Cu bud on the Pd seed.²⁰ At t = 60 min (Figure 3b), more Cu atoms were generated and the Janus structure of the nanocrystals became more obvious. For some of the nanocrystals obtained at this stage, the twin defects could be clearly resolved during TEM imaging. After another 30 min, the majority of the nanocrystals grew into the pentagonal-bipyramidal shape, and further extension of the reaction time to 120 min did not cause additional changes to the shape and size of the nanocrystals (Figure 3, c and d). We also observed some Cu nanocrystals containing no Pd seeds in the products, which could be attributed to homogeneous rather than heterogeneous nucleation.³⁷ Since the nanocrystals made of pure Cu and the Pd-Cu nanocrystals were more or less similar in terms of size, both of them could prevail in the products owing to the suppression of Ostwald ripening.³⁸ From the penta-twinned structure of the bipyramid, it can be concluded that the Cu atoms initially nucleated from one of the vertices of an icosahedral seed, followed by gradual growth into an elongated, pentagonal bipyramid.

Similar to the case of pentagonal bipyramids, the Cu atoms were also selectively deposited on one side of the Pd seed during the synthesis of Pd–Cu decahedra, with Figure 4a showing a TEM image of the sample obtained at t = 10 min. There were also some hollow nanocrystals bearing voids next to the surface, and their formation could be attributed to the oxidation of Cu

by the Kirkendall effect when washing the sample with water. The faster outward diffusion of Cu compared to the inward diffusion of oxygen led to the generation of voids next to the surface. This phenomenon was commonly observed during the storage of Cu particles,³⁹ and similar hollow structures were also found in the early stage of truncated bitetrahedra. At t = 20 min (Figure 4b), more Cu atoms were generated to increase the dimension of the Cu portion, together with the appearance of twin boundaries. Interestingly, the shape of the nanocrystals at this stage was quite similar to that of the pentagonal bipyramids, indicating that the pentagonal bipyramid might be an intermediate involved in the formation of a decahedron. When extending the time to t = 60 min, the nanocrystals were found to grow laterally and their decahedral shape became obvious (Figure 4c). Finally, most of the nanocrystals evolved into a decahedral shape at t = 120 min (Figure 4d). Taken together, it can be concluded that the Cu atoms also selectively nucleated from one of the vertices of an icosahedral seed at the beginning of a synthesis for the formation of pentagonal bipyramids. In the presence of an adequate supply of Cu atoms, they finally evolved into decahedra.

For the synthesis of Pd-Cu truncated bitetrahedra, the growth took a pathway different from the other two shapes. As shown in Figure 5a, we observed intermediates with a rod-like shape in the initial stage (t = 30 min) of a synthesis. The Pd icosahedral seed could be found at one of the two ends of the rod, with a single twin boundary passing through it. There were also small, pseudo-spherical Cu particles in the sample, and they disappeared after another 30-min into the synthesis due to Ostwald ripening (Figure 5b). With the supply of more Cu atoms, the rods evolved into a singly-twinned, bitetrahedral structure with truncation at axial corners. When the reaction time was extended to 90 and 120 min, respectively, the average edge length of the truncated bitetrahedra increased to 45.6 and 46.1 nm, together with a slight increase in sharpness for the corners at the equilateral plane (Figure 5, c and d). In addition to the Pd-Cu truncated bitetrahedra, we observed some Pd-Cu decahedra and pure Cu particles in a cubic or irregular shape in the product, which could be attributed to the growth of a small proportion of Cu atoms from vertices or the presence of homogeneous nucleation. Based on the TEM images and the

singly-twinned structure, it can be concluded that Cu was initially deposited onto one edge, instead of one vertex, of the Pd icosahedral seed, followed by growth into a truncated bitetrahedron as the reaction proceeded.

The Role of the Cu(II) Precursor. For the syntheses of Pd–Cu Janus nanocrystals with different shapes, the only variance is the amount of the Cu(II) precursor involved. When a small amount of CuCl₂ was used, the newly formed Cu atoms tended to nucleate and grow from one of the vertices of an icosahedral seed due to the low coordination number and high surface strain at this site.⁴⁰ The as-obtained Cu nanocrystals would take a penta-twinned structure because of the influence from the five twin planes intersecting at the vertex of the icosahedral seed. Upon increasing the amount of CuCl₂, the increased supply of Cu atoms would drive them to either diffuse to or directly nucleate from the edge.¹⁹ As a result of the twin boundary at the edge, the deposited Cu took a singly twinned structure.

The Role of HDA. When the concentration of the Cu(II) precursor was fixed, varying the concentration of HDA also resulted in the formation of Cu nanocrystals with distinctive shapes. With reference to the standard protocol for the synthesis of Pd-Cu decahedra, the product was dominated by truncated bitetrahedra when 22.5 mg instead of 45 mg of HDA was used, as shown in Figure 6a. A small fraction of Pd-Cu decahedra and pseudo-spherical Cu nanocrystals was also observed as the byproducts. When increasing the amount of HDA to 90 mg, Pd-Cu decahedral nanocrystals were again obtained, together with a few large, irregular-shaped Cu nanoparticles or Pd-Cu nanorods with Pd seed located at one end (Figure 6b). Relative to the standard protocol for the synthesis of Pd-Cu truncated bitetrahedra, if 35 mg instead of 45 mg of HDA was used, the majority of the product was still singly-twinned bitetrahedra, together with a small portion of Pd-Cu nanorods (Figure 6c). When 90 mg of HDA was used, which was twice as much as the amount of HDA used in the standard protocol, Pd-Cu decahedra in high purity were obtained, together with an average size of 46.8 nm (Figure 6d). These observations indicate that the concentration of HDA had a major impact on the shape evolution of the nanocrystals.

To make the trends more obvious, we did a set of experiments by varying the amounts of

CuCl₂ and HDA, and their dominant products are summarized in Table 1, with the corresponding TEM images shown in Figure S8. It is worth mentioning that, when 22.5 mg of HDA and 10.5 mg of CuCl₂ were used, no Cu nanocrystals were obtained. The main reason might be the lack of an adequate amount of HDA to protect the relatively large number of Cu atoms on the surface from being oxidized.⁴¹

Fixing the concentration of the Cu(II) precursor, we observed the switching from truncated bitetrahedra to decahedra and pentagonal bipyramids as the amount of HDA was increased, opposite to the trend observed for the Cu(II) precursor. To address this issue, we first looked into the role played by HDA in the synthesis of Cu nanocrystals. Typically, the influence of HDA can be understood from two different angles. Firstly, HDA can coordinate to Cu(II) ions to generate Cu(II)-HDA complexes, slowing down the reduction of the Cu(II) precursor. As a reference, after coordinating with NH₃, the standard reduction potential of Cu(NH₃)₄²⁺/Cu pair is reduced from 0.34 to 0 V_{SHE} (SHE: standard hydrogen electrode), making it more difficult to reduce the Cu(II) ions. 42,43 Secondly, HDA can serve as a capping agent and a colloidal stabilizer for Cu nanocrystals, preventing the Cu atoms from being oxidized by the oxygen from air.⁴¹ In our previous work on the synthesis of Pd@Cu core-shell nanocubes, a double layer of HDA was found to cover the Cu nanocrystals and it was believed to improve the chemical stability of the nanocubes.²⁰ Although HDA used to be considered as a selective capping agent for the Cu {100} facets, it should be mentioned that this assumption was recently challenged by several reports. 44-46 In one report, it was demonstrated that the HDA-Cu(0) interaction would be weakened when increasing the HDA packing density on the surface of Cu nanocrystals, which was attributed to a rapid exchange between the bound HDA on Cu and free HDA in solution.⁴⁵ In another report, based on the DFT calculation, the authors pointed out that the difference between the binding energies of HDA to Cu(100) and (111) surfaces was too small (0.12 eV) to enable HDA to selectively block Cu(100) surface. 44,46 In our case, we believe that the shape evolution of Cu nanocrystals was mainly dictated by the Pd icosahedral seeds. As a result, products mostly covered by {111} facets were produced regardless of the facet-selective capping effect from

HDA.

Considering all the influential factors, we proposed that the coordination to Cu(II) ions and thus the lowering in reduction potential was the major reason why penta-twinned structures were preferred at a high concentration of HDA. In the standard protocol for the synthesis of Pd-Cu truncated bitetrahedra, the molar concentration of HDA (37.3 mM) was only 3 times that of CuCl₂ (12.3 mM), comparing to 6 times for decahedra and 30 times for pentagonal bipyramids. With more HDA for coordination to Cu(II) ions, the reduction potential of the Cu(II) precursor was further lowered along with a decrease in the amount of Cu atoms generated in the initial stage of the reaction.⁴³ In this case, the Cu atoms preferentially nucleated from one of the vertices of the icosahedral seed, similar to the case where the concentration of the Cu(II) precursor was reduced. It was also reported that HDA could bind to the surface of Pd nanoparticles.⁴⁷ Thus, increasing the concentration of HDA would increase its packing density on the Pd seed and thus increase the steric hindrance for the surface diffusion of Cu atoms. Once the Cu atoms had been deposited on a vertex, their diffusion to adjacent edges and side faces would be largely blocked, resulting in the prevalence of penta-twinned Cu nanocrystals. In addition to HDA, appropriate concentrations of glucose (Table S2 and Figure S9) and Cl⁻ ions (Figure S10) are also critical in controlling the reduction rate of Cu(II) precursor and thus generating Janus nanocrystals with well-defined shapes and high purity. The size of the Pd-Cu nanocrystals could also be tuned by simply varying the amount of Pd seeds introduced (Figure S11). More detailed discussion on the roles of glucose and Cl⁻ions, as well as size control, can be found in the Supporting Information.

Catalytic Activity toward the Electrochemical Reduction of CO₂. Considering the bimetallic composition and Janus structure of the Pd-Cu nanocrystals, we evaluated them as catalysts for the electrochemical reduction of CO₂ and paid special attention to their selectivity toward C₂₊ products. The results are summarized in Figure 7, a–d, with the details provided in Table S3–S5. At -0.7 V_{RHE} in a 0.5 M KHCO₃ electrolyte, we observed the generation of C₂₊ products, including ethylene and ethanol, for all the three catalysts at 11.6, 11.2, and 9.4% for the

pentagonal bipyramids, decahedra, and truncated bitetrahedra, respectively. The onset potential was relatively low compared to other types of Cu-based catalysts reported in literature (Table S1).²²⁻²⁵ As the potential was further decreased, an increase in the selectivity toward C₂₊ products was observed. Specifically, at -1.0 V_{RHE}, the faradaic efficiencies (FEs) of C₂₊ species reached 50.3, 51.0, and 38.5% for the pentagonal bipyramids, decahedra, and truncated bitetrahedra, respectively, demonstrating superior performance relative to other Cu catalysts in 0.5 M KHCO₃ electrolyte (Table S1). The three Janus catalysts showed similar activities toward C₂₊ products, with the geometric current densities approaching 17.6, 15.3, and 15.6 mA/cm² for the pentagonal bipyramids, decahedra, and truncated bitetrahedra, respectively (Figure 7d). Their mass activities are also close to each other (Figure S12, 310.5, 290.6, and 305.1 mA/mg, respectively).

The high C₂₊ selectivity of the Pd-Cu Janus nanocrystals could be largely attributed to the separation between Pd and Cu, the involvement of Pd surface in the catalysis, and the twin boundaries on Cu surface. Since Pd can actively generate CO during the electrochemical reduction of CO₂ in the potential range of -0.7 to -1.0 V_{RHE}, the excess amount of CO on Pd surface is expected to migrate to the adjacent Cu surface and then undergo C-C coupling for the formation of C₂₊ products. ^{17,18,48,49} To support this argument, we also measured the catalytic performance of Pd icosahedra (Figure S13) and Cu twinned nanoparticles (Figure S14), both supported on carbon, in the electrochemical reduction of CO₂. As shown in Figure 7, e and f, all the three Pd-Cu Janus nanocrystals exhibited greater C2+ selectivity and activities at -1.0 VRHE compared to pure Pd (0% for C₂₊ FE) and Cu references (37.6% for C₂₊ FE and 273.1 mA/mg for mass activity), suggesting the importance of Pd in promoting the production of C₂₊ species. With regard to the CO production rate (Figure 7f), the highest mass activity was achieved by Pd icosahedra (33.3 mA/mg), which was much greater than either those of the Janus nanocrystals (12.2, 7.8, and 12.2 mA/mg for pentagonal bipyramids, decahedra, and truncated bitetrahedra, respectively) or that of Cu nanoparticles (20.8 mA/mg), indicating the involvement of CO spillover from Pd to Cu. These results suggest that the large amount of CO generated on the Pd surface migrated to the neighboring Cu surface, leading to an increased CO coverage density on Cu for enhanced C-C coupling and augmented C₂₊ production. Furthermore, the as-prepared Pd-Cu nanocrystals were all characterized by a twin structure. The presence of planar defects might also attract the C₁ intermediates and contribute to the production of C₂₊ species.²¹ It was previously reported that the existence of twin defects and stacking faults could enhance the adsorption of CO on the surface of Cu nanocrystals, leading to a higher CO coverage density for the promotion of C-C coupling.¹⁶

When normalized to the electrochemically active surface area (ECSA, Figure S15 and Table S6), the truncated bitetrahedra gave a much higher current density (76.4 mA/cm²) than those of pentagonal bipyramids (32.8 mA/cm²) and decahedra (41.5 mA/cm²), although they exhibited a lower C2+ selectivity. This trend can be ascribed to the detrimental impact of twin defects and under-coordinated atoms if they are presented at a very high density on the Cu surface. Though these defects can enhance the adsorption of CO intermediates and facilitate the C-C coupling, too many low-coordinated sites might result in strong binding of intermediates and even products, slowing down their desorption from the catalyst surface and thus lowering the activity. Besides, it is worth noting that, in the present study, the difference in ECSA for the three Pd-Cu catalysts had nearly no influence on their selectivity. Taking the Pd-Cu pentagonal bipyramids as an example, negligible changes were observed when decreasing the loading amount of Cu from 40 to 20 µg (Table S7), indicating the reliability in comparing the selectivity among the three different Pd-Cu catalysts.

We further evaluated the shape and compositional stability of the Pd-Cu Janus nanocrystals during CO₂ reduction. As shown in Figure S16, a–f, after 1 h of electrolysis at -1.0 V_{RHE}, the twin defects and well-defined facets of the nanocrystals were largely preserved. We also found some dissolution of Cu from the edges and corners, together with the formation of small Cu particles around the Pd-Cu nanocrystals, as marked by circles in Figure S16, d–f. Similar phenomena were also reported for Cu nanocubes,⁵¹ which can be ascribed to the adsorption of H and CO on Cu nanoparticles and the induced shape degradation under negative potentials. In Figure S16, d–f, the Pd and Cu portions of the nanocrystals could be easily distinguished by their

contrasts and we could clearly resolve the boundaries between them, suggesting the maintenance of separation between Pd and Cu during electrolysis. This conclusion was further supported by the XRD data (Figure S16, g–i). The missing of shift to the Cu peaks indicated the absence of Pd-Cu alloying or interphase mixing between Pd and Cu. Taking Pd-Cu decahedra, which exhibited the highest C₂₊ selectivity, as an example, we evaluated their long-term stability toward the electrochemical CO₂ reduction. After 15 h of electrolysis at -1.0 V_{RHE}, a decrease of 19.9% was observed for the FE toward ethylene, together with an increase of 14.0% for the total current density (Figure S17). Combining with the TEM images after 3 and 5 h of electrolysis (Figure S18), where fragmentation and sintering of the nanocrystals were observed, we could infer that the shape deformation contributed most significantly to the degradation in C₂₊ selectivity. Further endeavors should be devoted to improving the stability of Janus nanocrystals by maintaining their shapes and structures during long-term electrolysis.

Detection of *CO Intermediates Using Infrared (IR) Absorption Spectroscopy in an Attenuated Total Reflection (ATR) Mode. We also conducted *in situ* ATR-IR measurements on the Pd–Cu decahedra and Cu twinned nanoparticles, with the latter serving as a reference, during CO₂ reduction. The results are presented in Figure S19. It should be pointed out that no IR band related to the *CO adsorbed on Pd could be detected on the Pd–Cu decahedra due to the extremely low (<7%) coverage of Pd on the surface of a Janus nanocrystal. For both the Pd–Cu decahedra and Cu twinned nanoparticles, we observed an IR band at around 1800 cm⁻¹. According to the literature, ^{52,53} this band could be assigned to the bridge- or multiple-adsorbed *CO on the Cu surface. As the applied potential became more negative, the red-shift of the band could be attributed to a combination of the Stark tuning effect (red-shift) and the increase in *CO coverage (blue-shift). During the cathodic sweep, the *CO band started to appear on the Pd–Cu decahedra at a potential around -0.6 V_{RHE}, which was 100 mV more positive than that on Cu twinned nanoparticles. This observation indicated that *CO was more easily formed on the Janus catalyst, offering a piece of evidence to support our argument about the role of Pd in promoting the formation of CO, which could then migrate to the Cu surface. Compared to the Cu twinned

particles, the *CO band was much stronger on the Pd–Cu decahedra, which might be related to the higher *CO coverage on the surface of the Janus catalyst. However, it is difficult to quantitatively compare the band intensities between two individually prepared electrodes due to the variations in optical conditions.

Theoretical Study of CO Spillover from Pd to Cu. To demonstrate that CO can form on the Pd surface and then migrate to the Cu surface for subsequent C-C coupling, we performed a series of DFT-based calculations on Pd(111) and Cu(111), the two extended facets exposed on the Pd-Cu Janus nanocrystals. The details of the calculations can be found in the Supporting Information. We first investigated the conditions under which CO spillover from Pd(111) to Cu(111) would occur. To this end, we calculated the binding energies and structures of CO adsorbed on Pd(111) and Cu(111) at various CO coverages up to 1 ML, with an increment of 1/9 ML. The preferred CO adsorption structures are summarized in Figure S20, and the average and differential binding energies (abbreviated as BE_{avg} and dBE, respectively) of CO are graphically shown in Figure 8, a and b, as a function of CO coverage. A general trend can be observed in which both the BE_{avg} and dBE values remain relatively unchanged at low CO coverages and rapidly become less negative at higher CO coverages. This trend indicates that the CO-CO lateral interactions are generally repulsive, resulting in destabilization of CO adsorption at higher CO coverages. As shown in Figure 8b, the differential binding energies of CO on Pd(111) and Cu(111) are positive (i.e., adsorption of additional CO is energetically unfavorable) when the CO coverage reaches 8/9 ML and 6/9 ML, respectively. Therefore, the CO saturation coverages at 0 K and under vacuum are approximately 7/9 ML on Pd(111) and 5/9 ML on Cu(111), which are in good agreement with the experimentally measured CO saturation coverages of 0.75 and 0.52 ML on Pd(111) and Cu(111), respectively, under ultra-high-vacuum (UHV) condition. 55,56

From Figure 8b, it can also be observed that CO binds more strongly to Pd(111) than to Cu(111). The differential binding energy of CO on Pd(111) remains more negative than -0.98 eV (the binding energy of CO on clean Cu(111) at 1/9 ML coverage; indicated by the red dashed line in Figure 8b) until the CO coverage on Pd(111) increases up to 6/9 ML. These results can be

interpreted as follows: initially, when the Pd-Cu nanocrystal surface is empty, CO is mostly generated from and also prefers to bind to the Pd surface due to the stronger binding strength. The CO coverage on Pd(111) starts to build up while the Cu(111) surface remains to be largely free of CO. ^{16,49} Even with the increasing coverage, additional CO molecules still prefer binding to the Pd surface until the CO coverage on Pd(111) reaches 6/9 ML. Since then, the binding energy of an additional CO molecule (*i.e.*, the differential binding energy at 7/9 ML CO coverage) becomes -0.33 eV, which is 0.65 eV more positive than the binding energy of CO on clean Cu(111). As a result, the additional CO molecules generated on the 6/9 ML CO-covered Pd(111) surface would have a thermochemical driving force to migrate to the Cu(111) surface. We thus conclude that CO spillover from Pd(111) to Cu(111) becomes thermodynamically favorable when the CO coverage on Pd(111) exceeds 6/9 ML. To sustain that reactive pattern, one would need to keep the CO coverage on Cu(111) below 4/9 ML. We argue that the rate of the reaction for consuming CO on Cu(111) facets of the Janus nanocrystals is sufficient to keep up with the migration of CO from Pd, so that the CO coverage on Cu(111) can be kept at that critical level or below.

We also explored the impact of potential palladium hydride (PdH) formation on our proposed CO spillover mechanism. Past experimental studies suggested that PdH could be formed on metallic Pd catalysts under the electrochemical conditions relevant to CO₂ reduction due to the competing HER.^{57–59} Although we do not have direct evidence in our experiments, the possibility of PdH formation on the Pd portion of our Pd-Cu Janus nanocrystals during the measurements could not be eliminated. To this end, we considered an extensive list of possible surface/bulk PdH models, including: (1) the PdH(111) surface with its optimized lattice constant, (2) pseudomorphic PdH overlayers on a Pd(111) substrate (denoted PdH_{xL}/Pd(111); x = 1–3 denotes the number of Pd-H bilayers) as models for thin-layer surface hydride, whereby the optimized lattice constant of pure Pd is used, and (3) a compressed PdH(111) slab at the bulk lattice constant of metallic Pd (compressed by approximately 5%; denoted PdH_{comp}(111)). The last one serves as a model for the limiting case of a surface hydride grown on Pd(111), when the

PdH layer thickness is sufficiently large so that the PdH surface barely experiences the electronic effect from the Pd(111) substrate, and yet the lattice confinement is preserved. The structural details of all the PdH slab models adopted in this study are shown in Figure S20. In the absence of any adsorbate, all these surfaces prefer a H-terminated geometry. On each PdH slab model, we evaluated the binding structures and energies for CO at surface coverages from 1/9 to 1 ML. The calculated BE_{avg} and dBE values on PdH(111) and PdH_{1L}/Pd(111) are graphically shown in Figure 8, a and b, as a function of the CO surface coverage. The corresponding values on the other PdH slab models are shown in Figure S21. The preferred CO adsorption structures are summarized in Figure S22–S26.

On all the PdH slab models, similar nonmonotonic trends were observed for the dBE of CO as a function of CO coverage (Figure 8b and S21). At 1/9 ML coverage, CO binds more weakly to all the PdH surfaces than both Cu(111) and Pd(111); e.g., the BEs of CO at 1/9 ML coverage are -0.76 eV and -0.40 eV on PdH(111) and PdH_{1L}/Pd(111), respectively, compared to -0.98 eV on Cu(111) and -2.28 eV on Pd(111). As the CO coverage increases to 3/9 ML, its dBE value rapidly becomes more negative on all the PdH slab models we studied. Importantly, our calculations suggest that the weak and increasing binding strength of CO at low coverage on the PdH surfaces is attributed to a CO-induced transition from the H termination to Pd termination of the PdH surfaces, as illustrated in Figure 8, c and d. The strong Pd-CO interaction draws Pd atoms to the surface, further stabilizing the subsequent CO binding. On PdH(111), this transition occurs when the CO coverage increases from 1/9 to 2/9 ML (Figure 8c). On all the PdH_{xL}/Pd(111) (x = 1-3) surfaces, the Pd-terminated surface becomes energetically preferred when CO coverage increases from 2/9 to 3/9 ML (see Figure 8d for PdH₁L/Pd(111), Figure S24 and S25 for PdH_{2L}/Pd(111) and PdH_{3L}/Pd(111), respectively). Interestingly, a CO coverage of 1/9 ML is sufficient to cause the H-to-Pd surface termination transition on the PdH_{comp}(111) surface (Figure S26).

Once the transition is accomplished, the Pd termination remains to be preferred at higher CO coverages, and the PdH surfaces can thus be viewed as a Pd(111) over PdH substrates. The

presence of a Pd-terminated surface has also been evidenced in a previous study by Gao et al.⁵⁸ They demonstrated that a β-PdH_x@Pd phase (i.e., metallic Pd shell outside a PdH core) was formed during the electrochemical reduction of CO₂ at applied potentials more negative than -0.5 V_{RHE}, when CO started to dominate the surface. At CO coverages of 3/9–5/9 ML, the dBE of CO reaches its most negative value on every PdH model slab we studied. Within this surface coverage range, CO adsorption on any CO-covered PdH surface is thermodynamically preferred over its adsorption on clean Cu(111) (BE = -0.98 eV; red dashed line in Figure 8b and S21). Above 5/9 ML CO coverage on PdH, the effect of lateral CO-CO repulsion becomes more potent, and the adsorption of additional CO molecules is significantly destabilized. On PdH(111), when the CO coverage increases from 5/9 ML to 6/9 ML, the dBE of CO changes from -1.56 eV (0.58 eV more negative than BEco on clean Cu(111)) to -0.73 eV (0.25 eV more positive than BEco on clean Cu(111)). Therefore, similar to the previously discussed case of CO spillover from 6/9 ML CO-covered Pd(111) to Cu(111), there exists a thermochemical driving force for additional CO molecules produced on the 5/9 ML CO-covered PdH(111) surface to migrate to Cu(111). Despite the variance in dBE values, the same 5/9 ML threshold CO coverage for CO spillover to Cu(111) is observed on all the other PdH slab models (Figure 8b and S21). We conclude that, as long as a CO coverage of above 5/9 ML can be reached, PdH surfaces can also serve as a source of CO for its spillover to the adjacent Cu(111) surface of the Janus nanocrystals.

Next, we sought to address the following question: is the required CO coverages for CO spillover to Cu(111) (6/9 ML or above for Pd(111), 5/9 ML or above for PdH surfaces) achievable under the electrochemical conditions for CO₂ reduction? To tackle this question, we constructed theoretical Pourbaix phase diagrams using the DFT results from our CO coverage study on Pd(111) and PdH slab models. The procedures for the Pourbaix phase diagram construction were adapted from the work by Zeng and co-workers⁶⁰ and are detailed in the Supporting Information. The Pourbaix phase diagrams for CO adsorption on Pd(111), PdH(111), and PdH_{1L}/Pd(111) are shown in Figure 9. Those for PdH_{2L}/Pd(111), PdH_{3L}/Pd(111) and PdH_{comp}(111) are shown in Figure S27, S28, and S29, respectively. These phase diagrams allow

us to predict the most stable CO coverage on Pd(111), including hydride phases, under any given applied potential. In general, as shown in Figure 9, the CO coverage gradually increases as the applied potential becomes more negative. Based on these Pourbaix phase diagrams, the predicted CO coverages under the experimental conditions of interest in this work (-0.7 to -1.0 V_{RHE}) are identified and summarized in Table 2. On Pd(111), the predicted CO coverage under these applied potentials is either 7/9 ML or 1 ML (Figure 9b), which is clearly above the 6/9 ML threshold for CO spillover from Pd(111) to Cu(111). On all the PdH surfaces, the predicted CO coverages under the CO₂ reduction conditions are at least 6/9 ML, which are also greater than the 5/9 ML threshold established above for CO spillover from PdH surfaces to Cu(111). Therefore, we conclude that, under the electrochemical conditions for CO₂ reduction, a sufficiently high CO coverage can be attained on the Pd surface on our Pd-Cu Janus nanocrystals, regardless of its nature being metallic Pd, bulk hydride, or surface hydride, to enable the continuous migration of CO to Cu(111).

We also explored the catalytic role of twin boundaries on the Cu surface by comparing the binding energies of common CO_2 reduction intermediates on the twin boundary with those on the Cu(111) terrace (Figure S31 and Table S9). DFT calculations demonstrated the stronger binding of OH, CH, and CH_xO_y species on the undercoordinated Cu sites as compared to the Cu(111) terrace, and such strong binding might restrict the desorption of intermediates and even products, suggesting the detrimental effect of undercoordination atoms if they were in an extremely high proportion. A more detailed discussion can be found in the Supporting Information.

Conclusions

In summary, we have demonstrated a facile, seed-mediated synthesis of Pd–Cu nanocrystals with a twinned, Janus structure while taking different shapes. Due to the large lattice mismatch between Cu and Pd, the Cu atoms prefer to nucleate and grow from one site on a Pd icosahedral seed for the generation of Pd–Cu nanocrystals with a Janus structure. By simply controlling the concentrations of the Cu(II) precursor and HDA, the deposition of Cu atoms could be selectively

confined to either a vertex or an edge of the Pd icosahedral seed, leading to the formation of nanocrystals in the shapes of pentagonal bipyramid, decahedron, and truncated bitetrahedron, respectively. Specifically, decreasing the reduction rate of the Cu(II) precursor would result in the growth of Cu from the vertex for the generation of a penta-twinned nanocrystal, while a faster reduction would favor the growth from the edge for the formation of a singly twinned product. When applied as catalysts for the electrochemical reduction of CO₂ in a 0.5 M KHCO₃ electrolyte, an onset potential as low as -0.7 V_{RHE} was observed for the formation of C₂₊ products, together with high C₂₊ selectivity approaching 51.0% at -1.0 V_{RHE} for the Pd-Cu decahedra. The high yields of C₂₊ species could be attributed to the presence of Pd on the surface and the twin boundaries on Cu. The former feature facilitated the generation of CO, followed by its spillover to the Cu surface, while the latter enhanced the adsorption of CO. During the in situ ATR-IR measurements, the appearance of CO on the Cu surface was observed at a lower overpotential on the Pd-Cu decahedra than a reference based on pure Cu, suggesting the important role of Pd in promoting the formation of CO. Based on DFT calculations and Pourbaix phase diagrams, CO spillover from Pd(111) to Cu(111) is thermodynamically favored if the CO coverage on Pd(111) exceeds 6/9 ML. On the (111) facets of bulk/surface PdH, CO spillover to Cu(111) requires a CO coverage above 5/9 ML. Under the experimental conditions of the present study, the CO coverage can reach 7/9 or 1 ML on Pd(111) and at least 6/9 ML on the PdH surface, suggesting that CO can readily form on the Pd or PdH surface and subsequently migrate to the Cu surface for participation in the coupling reactions. This work not only sheds light on the site-selected growth of bimetallic nanocrystals with novel shapes and structures but also allows for the rational development of bimetallic catalysts toward the CO₂ reduction reaction.

Author Information

Corresponding Authors

- *younan.xia@bme.gatech.edu
- *kemshao@ust.hk
- *manos@engr.wisc.edu

Notes

The authors declare no competing financial interest.

Acknowledgements

This work was supported in part by a grant from the NSF (CHE 1804970) and start-up funds from the Georgia Institute of Technology. The electrocatalytic measurements were supported by two grants from the Research Grant Council of Hong Kong SAR (26206115 and 16309418) and one grant from the Hong Kong Branch of Southern Marine Science and Engineering Guangdong Laboratory (SMSEGL20SC01). S.Z. thanks the financial support from the Research Grant Council Postdoctoral Fellowship Scheme (PDFS2021-6S08). The TEM imaging and EDX mapping were performed at the Materials Characterization Facilities of the GT's Institute of Electronics and Nanotechnology (IEN), a member of the National Nanotechnology Coordinated Infrastructure (NNCI), which is supported by the National Science Foundation (ECCS-1542174). The STEM imaging was conducted at the Center for Nanophase Materials Sciences, which is a DOE Office of Science User Facility, and Arizona State University. J.L. acknowledges funding from the NSF (CHE-1465057) and the use of the John M. Cowley Center for High-Resolution Electron Microscopy at Arizona State University. L.X. and M.M. thank the computing resources at the National Energy Research Scientific Computing Center (NERSC), a DOE Office of Science User Facility supported by DOE contract DE-AC02-05CH11231. We thank Legna Figueroa-Cosme for XRD measurements, Ming Zhao for ICP-MS measurements, Zachary D. Hood, Mengkun Tian, and Zhenming Cao for STEM imaging, and Prof. Mingjie Zhang and Rui Feng from HKUST for NMR measurements.

References

- (1) Gilroy, K. D.; Ruditskiy, A.; Peng, H. C.; Qin, D.; Xia, Y. Bimetallic Nanocrystals: Syntheses, Properties, and Applications. *Chem. Rev.* **2016**, *116*, 10414–10472.
- (2) Gilroy, K. D.; Peng, H. C.; Yang, X.; Ruditskiy, A.; Xia, Y. Symmetry Breaking during Nanocrystal Growth. *Chem. Commun.* **2017**, *53*, 4530–4541.
- (3) Zhu, C.; Zeng, J.; Tao, J.; Johnson, M. C.; Schmidt-Krey, I.; Blubaugh, L.; Zhu, Y.; Gu, Z.; Xia, Y. Kinetically Controlled Overgrowth of Ag or Au on Pd Nanocrystal Seeds: From Hybrid Dimers to Nonconcentric and Concentric Bimetallic Nanocrystals. *J. Am. Chem. Soc.* **2012**, *134*, 15822–15831.
- (4) Zheng, Z.; Tachikawa, T.; Majima, T. Single-Particle Study of Pt-Modified Au Nanorods for Plasmon-Enhanced Hydrogen Generation in Visible to Near-Infrared Region. *J. Am. Chem. Soc.* **2014**, *136*, 6870–6873.
- (5) Xia, Y.; Xia, X.; Peng, H. C. Shape-Controlled Synthesis of Colloidal Metal Nanocrystals: Thermodynamic versus Kinetic Products. *J. Am. Chem. Soc.* **2015**, *137*, 7947–7966.
- (6) Xia, X.; Xie, S.; Liu, M.; Peng, H. C.; Lu, N.; Wang, J.; Kim, M. J.; Xia, Y. On the Role of Surface Diffusion in Determining the Shape or Morphology of Noble-Metal Nanocrystals. *Proc. Natl. Acad. Sci. U.S.A.* **2013**, *110*, 6669–6673.
- (7) Peng, H. C.; Park, J.; Zhang, L.; Xia, Y. Toward a Quantitative Understanding of Symmetry Reduction Involved in the Seed-Mediated Growth of Pd Nanocrystals. *J. Am. Chem. Soc.* **2015**, *137*, 6643–6652.
- (8) Yang, Y.; Wang, W.; Li, X.; Chen, W.; Fan, N.; Zou, C.; Chen, X.; Xu, X.; Zhang, L.; Huang, S. Controlled Growth of Ag/Au Bimetallic Nanorods through Kinetics Control. *Chem. Mater.* **2013**, *25*, 34–41.
- (9) Cathcart, N.; Kitaev, V. Symmetry Breaking by Surface Blocking: Synthesis of Bimorphic Silver Nanoparticles, Nanoscale Fishes and Apples. *Sci. Rep.* **2016**, *6*, 32561.
- (10) Liu, M.; Gilroy, K. D.; Peng, H. C.; Chi, M.; Guo, L.; Xia, Y. The Effect of Surface Capping on the Diffusion of Adatoms in the Synthesis of Pd@Au Core-Shell Nanocrystals. *Chem.*

- Commun. 2016, 52, 13159–13162.
- (11) Cobley, C. M.; Rycenga, M.; Zhou, F.; Li, Z. Y.; Xia, Y. Etching and Growth: An Intertwined Pathway to Silver Nanocrystals with Exotic Shapes. *Angew. Chem. Int. Ed.* **2009**, *48*, 4824–4827.
- (12) Luo, M.; Ruditskiy, A.; Peng, H. C.; Tao, J.; Figueroa-Cosme, L.; He, Z.; Xia, Y. Penta-Twinned Copper Nanorods: Facile Synthesis via Seed-Mediated Growth and Their Tunable Plasmonic Properties. *Adv. Funct. Mater.* **2016**, *26*, 1209–1216.
- (13) Gawande, M. B.; Goswami, A.; Felpin, F. X.; Asefa, T.; Huang, X.; Silva, R.; Zou, X.; Zboril, R.; Varma, R. S. Cu and Cu-Based Nanoparticles: Synthesis and Applications in Catalysis. *Chem. Rev.* **2016**, *116*, 3722–3811.
- (14) Loiudice, A.; Lobaccaro, P.; Kamali, E. A.; Thao, T.; Huang, B. H.; Ager, J. W.; Buonsanti, R. Tailoring Copper Nanocrystals towards C₂ Products in Electrochemical CO₂ Reduction. *Angew. Chem. Int. Ed.* **2016**, *55*, 5789–5792.
- (15) Nitopi, S.; Bertheussen, E.; Scott, S. B.; Liu, X.; Engstfeld, A. K.; Horch, S.; Seger, B.; Stephens, I. E. L.; Chan, K.; Hahn, C.; Nørskov, J. K.; Jaramillo, T. F.; Chorkendorff, I. Progress and Perspectives of Electrochemical CO₂ Reduction on Copper in Aqueous Electrolyte. *Chem. Rev.* **2019**, *119*, 7610–7672.
- (16) Choi, C.; Cheng, T.; Flores Espinosa, M.; Fei, H.; Duan, X.; Goddard, W. A.; Huang, Y. A Highly Active Star Decahedron Cu Nanocatalyst for Hydrocarbon Production at Low Overpotentials. *Adv. Mater.* **2019**, *31*, 1805405.
- (17) Ma, S.; Sadakiyo, M.; Heim, M.; Luo, R.; Haasch, R. T.; Gold, J. I.; Yamauchi, M.; Kenis, P. J. A. Electroreduction of Carbon Dioxide to Hydrocarbons Using Bimetallic Cu-Pd Catalysts with Different Mixing Patterns. *J. Am. Chem. Soc.* **2017**, *139*, 47–50.
- (18) Huang, J.; Mensi, M.; Oveisi, E.; Mantella, V.; Buonsanti, R. Structural Sensitivities in Bimetallic Catalysts for Electrochemical CO₂ Reduction Revealed by Ag-Cu Nanodimers. *J. Am. Chem. Soc.* **2019**, *141*, 2490–2499.
- (19) Lv, T.; Yang, X.; Zheng, Y.; Huang, H.; Zhang, L.; Tao, J.; Pan, L.; Xia, Y. Controlling the

- Growth of Au on Icosahedral Seeds of Pd by Manipulating the Reduction Kinetics. *J. Phys. Chem. C* **2016**, *120*, 20768–20774.
- (20) Jin, M.; Zhang, H.; Wang, J.; Zhong, X.; Lu, N.; Li, Z.; Xie, Z.; Kim, M. J.; Xia, Y. Copper Can Still Be Epitaxially Deposited on Palladium Nanocrystals to Generate Core-Shell Nanocubes Despite Their Large Lattice Mismatch. *ACS Nano* **2012**, *6*, 2566–2573.
- (21) Zheng, Y.; Vasileff, A.; Zhou, X.; Jiao, Y.; Jaroniec, M.; Qiao, S. Z. Understanding the Roadmap for Electrochemical Reduction of CO₂ to Multi-Carbon Oxygenates and Hydrocarbons on Copper-Based Catalysts. *J. Am. Chem. Soc.* **2019**, *141*, 7646–7659.
- (22) Kim, J.; Choi, W.; Park, J. W.; Kim, C.; Kim, M.; Song, H. Branched Copper Oxide Nanoparticles Induce Highly Selective Ethylene Production by Electrochemical Carbon Dioxide Reduction. *J. Am. Chem. Soc.* **2019**, *141*, 6986–6994.
- (23) Suen, N. T.; Kong, Z. R.; Hsu, C. S.; Chen, H. C.; Tung, C. W.; Lu, Y. R.; Dong, C. L.; Shen, C. C.; Chung, J. C.; Chen, H. M. Morphology Manipulation of Copper Nanocrystals and Product Selectivity in the Electrocatalytic Reduction of Carbon Dioxide. *ACS Catal.* **2019**, *9*, 5217–5222.
- (24) Liu, H.; Xiang, K.; Liu, Y.; Zhu, F.; Zou, M.; Yan, X.; Chai, L. Polydopamine Functionalized Cu Nanowires for Enhanced CO₂ Electroreduction Towards Methane. *ChemElectroChem* **2018**, *5*, 3991–3999.
- (25) Weng, Z.; Zhang, X.; Wu, Y.; Huo, S.; Jiang, J.; Liu, W.; He, G.; Liang, Y.; Wang, H. Self-Cleaning Catalyst Electrodes for Stabilized CO₂ Reduction to Hydrocarbons. *Angew. Chem. Int. Ed.* **2017**, *56*, 13135–13139.
- (26) Wang, X.; Choi, S. Il; Roling, L. T.; Luo, M.; Ma, C.; Zhang, L.; Chi, M.; Liu, J.; Xie, Z.; Herron, J. A.; Mavrikakis, M.; Xia, Y. Palladium-Platinum Core-Shell Icosahedra with Substantially Enhanced Activity and Durability towards Oxygen Reduction. *Nat. Commun.* **2015**, *6*, 7594.
- (27) Wang, H.; Zhou, S.; Gilroy, K. D.; Cai, Z.; Xia, Y. Icosahedral Nanocrystals of Noble Metals: Synthesis and Applications. *Nano Today.* **2017**, *15*, 121–144.
- (28) Wang, Z.; Chen, Z.; Zhang, H.; Zhang, Z.; Wu, H.; Jin, M.; Wu, C.; Yang, D.; Yin, Y.

- Lattice-Mismatch-Induced Twinning for Seeded Growth of Anisotropic Nanostructures. *ACS Nano* **2015**, *9*, 3307–3313.
- (29) Wu, D.; Cao, M.; Cao, R. Ru-Assisted Synthesis of {111}-Faceted Pd Truncated Bipyramids: A Highly Reactive, Stable and Restorable Catalyst for Formic Acid Oxidation. *Chem. Commun.* **2014**, *50*, 12970–12972.
- (30) Zhang, J.; Langille, M. R.; Mirkin, C. A. Photomediated Synthesis of Silver Triangular Bipyramids and Prisms: The Effect of pH and BSPP. *J. Am. Chem. Soc.* **2010**, *132*, 12502–12510.
- (31) Biesinger, M. C.; Payne, B. P.; Grosvenor, A. P.; Lau, L. W. M.; Gerson, A. R.; Smart, R. S. C. Resolving Surface Chemical States in XPS Analysis of First Row Transition Metals, Oxides and Hydroxides: Sc, Ti, V, Cu and Zn. *Appl. Surf. Sci.* **2010**, *257*, 887–898.
- (32) Lyu, Z.; Xie, M.; Gilroy, K. D.; Hood, Z. D.; Zhao, M.; Zhou, S.; Liu, J.; Xia, Y. A Rationally Designed Route to the One-Pot Synthesis of Right Bipyramidal Nanocrystals of Copper. *Chem. Mater.* **2018**, *30*, 6469–6477.
- (33) Pietrobon, B.; Kitaev, V. Photochemical Synthesis of Monodisperse Size-Controlled Silver Decahedral Nanoparticles and Their Remarkable Optical Properties. *Chem. Mater.* **2008**, *20*, 5186–5190.
- (34) Pastoriza-Santos, I.; Sánchez-Iglesias, A.; Rodríguez-González, B.; Liz-Marzán, L. M. Aerobic Synthesis of Cu Nanoplates with Intense Plasmon Resonances. *Small* **2009**, *5*, 440–443.
- (35) Sherry, L. J.; Jin, R.; Mirkin, C. A.; Schatz, G. C.; Van Duyne, R. P. Localized Surface Plasmon Resonance Spectroscopy of Single Silver Triangular Nanoprisms. *Nano Lett.* **2006**, *6*, 2060–2065.
- (36) Ringe, E.; Zhang, J.; Langille, M. R.; Mirkin, C. A.; Marks, L. D.; Van Duyne, R. P. Correlating the Structure and Localized Surface Plasmon Resonance of Single Silver Right Bipyramids. *Nanotechnology* **2012**, *23*, 444005.
- (37) Lyu, Z.; Xie, M.; Aldama, E.; Zhao, M.; Qiu, J.; Zhou, S.; Xia, Y. Au@Cu Core-Shell Nanocubes with Controllable Sizes in the Range of 20–30 nm for Applications in Catalysis and

- Plasmonics. ACS Appl. Nano Mater. 2019, 2, 1533–1540.
- (38) Dai, Y.; Lu, P.; Cao, Z.; Campbell, C. T.; Xia, Y. The Physical Chemistry and Materials Science behind Sinter-Resistant Catalysts. *Chem. Soc. Rev.* **2018**, *47*, 4314–4331.
- (39) Hung, L. L.; Tsung, C. K.; Huang, W.; Yang, P. Room-Temperature Formation of Hollow Cu₂O Nanoparticles. *Adv. Mater.* **2010**, *22*, 1910–1914.
- (40) Yang, T. H.; Zhou, S.; Gilroy, K. D.; Figueroa-Cosme, L.; Lee, Y. H.; Wu, J. M.; Xia, Y. Autocatalytic Surface Reduction and Its Role in Controlling Seed-Mediated Growth of Colloidal Metal Nanocrystals. *Proc. Natl. Acad. Sci. U.S.A.* **2017**, *114*, 13619–13624.
- (41) Liu, S. H.; Fichthorn, K. A. Interaction of Alkylamines with Cu Surfaces: A Metal-Organic Many-Body Force Field. *J. Phys. Chem. C* **2017**, 121, 22531–22541.
- (42) Meng, M.; Fang, Z.; Zhang, C.; Su, H.; He, R.; Zhang, R.; Li, H.; Li, Z. Y.; Wu, X.; Ma, C.; Zeng, J. Integration of Kinetic Control and Lattice Mismatch to Synthesize Pd@AuCu Core-Shell Planar Tetrapods with Size-Dependent Optical Properties. *Nano Lett.* **2016**, *16*, 3036–3041.
- (43) Bard, A. J.; Faulkner, L. R. *Electrochemical Methods: Fundamentals and Applications 2nd Ed*; Wiley: New York, **2001**.
- (44) Liu, S. H.; Balankura, T.; Fichthorn, K. A. Self-Assembled Monolayer Structures of Hexadecylamine on Cu Surfaces: Density-Functional Theory. *Phys. Chem. Chem. Phys.* **2016**, *18*, 32753–32761.
- (45) Glaria, A.; Cure, J.; Piettre, K.; Coppel, Y.; Turrin, C. O.; Chaudret, B.; Fau, P. Deciphering Ligands' Interaction with Cu and Cu₂O Nanocrystal Surfaces by NMR Solution Tools. *Chem. Eur. J.* **2015**, *21*, 1169–1178.
- (46) Kim, M. J.; Alvarez, S.; Chen, Z.; Fichthorn, K. A.; Wiley, B. J. Single-Crystal Electrochemistry Reveals Why Metal Nanowires Grow. *J. Am. Chem. Soc.* **2018**, *140*, 14740–14746.
- (47) Sun, H.; Jiao, X.; Wang, H.; Jiang, Z.; Chen, D. Solvothermal Preparation of Pd Nanostructures under Nitrogen and Air Atmospheres and Electrocatalytic Activities for the

- Oxidation of Methanol. ACS Appl. Mater. Interfaces 2011, 3, 2425–2430.
- (48) Gao, D.; Zhou, H.; Cai, F.; Wang, J.; Wang, G.; Bao, X. Pd-Containing Nanostructures for Electrochemical CO₂ Reduction Reaction. *ACS Catal.* **2018**, *8*, 1510–1519.
- (49) Huang, H.; Jia, H.; Liu, Z.; Gao, P.; Zhao, J.; Luo, Z.; Yang, J.; Zeng, J. Understanding of Strain Effects in the Electrochemical Reduction of CO₂: Using Pd Nanostructures as an Ideal Platform. *Angew. Chem. Int. Ed.* **2017**, *56*, 3594–3598.
- (50) Reske, R.; Mistry, H.; Behafarid, F.; Roldan Cuenya, B; Strasser, P. Particle Size Effects in the Catalytic Electroreduction of CO₂ on Cu Nanoparticles. *J. Am. Chem. Soc.* **2014**, *136*, 6978–6986.
- (51) Huang, J.; Hörmann, N.; Oveisi, E.; Loiudice, A.; De Gregorio, G. L.; Andreussi, O., Marzari, N.; and Buonsanti, R. Potential-Induced Nanoclustering of Metallic Catalysts during Electrochemical CO₂ Reduction. *Nat. Commun.* **2018**, *9*, 3117.
- (52) Zhu, S.; Li, T.; Cai, W. B.; Shao, M. CO₂ Electrochemical Reduction as Probed through Infrared Spectroscopy. *ACS Energy Lett.* **2019**, *4*, 682–689.
- (53) Hayden, B. E.; Kretzschmar, K.; Bradshaw, A. M. An Infrared Spectroscopic Study of CO on Cu(111): the Linear, Bridging and Physisorbed Species. *Surf. Sci.* **1985**, *155*, 553–566.
- (54) Zhu, S.; Jiang, B.; Cai, W. B.; Shao, M. Direct Observation on Reaction Intermediates and the Role of Bicarbonate Anions in CO₂ Electrochemical Reduction Reaction on Cu Surfaces. *J. Am. Chem. Soc.* **2017**, *139*, 15664–15667.
- (55) Rupprechter, G.; Unterhalt, H.; Morkel, M.; Galletto, P.; Dellwig, T.; Freund, H. J. Extending UHV Studies to the Mbar Range: Vibrational SFG Spectroscopy of High-Pressure CO Adsorption on Pt(111) and Pd(111). *Vacuum* **2003**, *71*, 83–87.
- (56) Hollins, P.; Pritchard, J. Interactions of CO Molecules Adsorbed on Cu(111). *Surf. Sci* **1979**, 89, 486–495.
- (57) Sheng, W.; Kattel, S.; Yao, S.; Yan, B.; Liang, Z.; Hawxhurst, C. J.; Wu, Q.; Chen, J. G. Electrochemical Reduction of CO₂ to Synthesis Gas with Controlled CO/H₂ Ratios. *Energy Environ. Sci.* **2017**, *10*, 1180–1185.

- (58) Gao, D.; Zhou, H.; Cai, F.; Wang, D.; Hu, Y.; Jiang, B.; Cai, W.-B.; Chen, X.; Si, R.; Yang, F.; Miao, S.; Wang, J.; Wang, G.; Bao, X. Switchable CO₂ Electroreduction via Engineering Active Phases of Pd Nanoparticles. *Nano Res.* **2017**, *10*, 2181–2191.
- (59) Zhu, W.; Kattel, S.; Jiao, F.; Chen, J. G. Shape-Controlled CO₂ Electrochemical Reduction on Nanosized Pd Hydride Cubes and Octahedra. *Adv. Energy Mater.* **2019**, *9*, 1802840.
- (60) Zeng, Z.; Chang, K. C.; Kubal, J.; Markovic, N. M.; Greeley, J. Stabilization of Ultrathin (Hydroxy)oxide Films on Transition Metal Substrates for Electrochemical Energy Conversion. *Nat. Energy* **2017**, *2*, 17070.

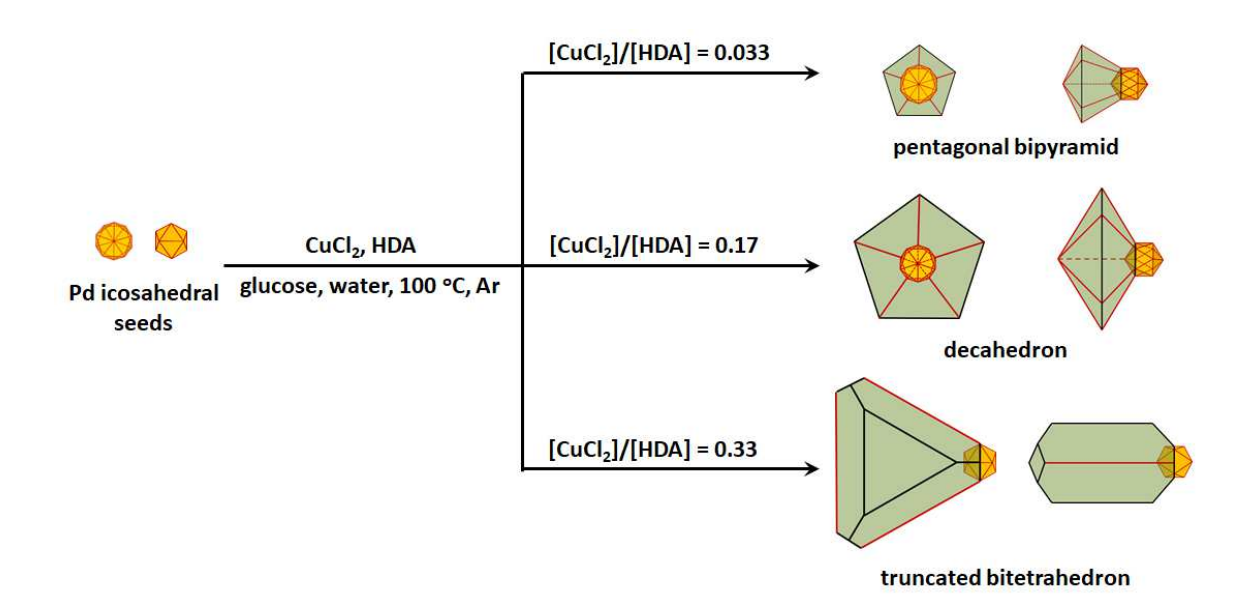


Figure 1. Summary of the experimental conditions corresponding to the formation of Pd-Cu Janus nanocrystals with three distinctive shapes for the Cu component: pentagonal bipyramid, decahedron, and truncated bitetrahedron. The Pd and Cu components are shown in yellow and green colors, respectively. The red lines indicate the twin boundaries on the nanocrystal.

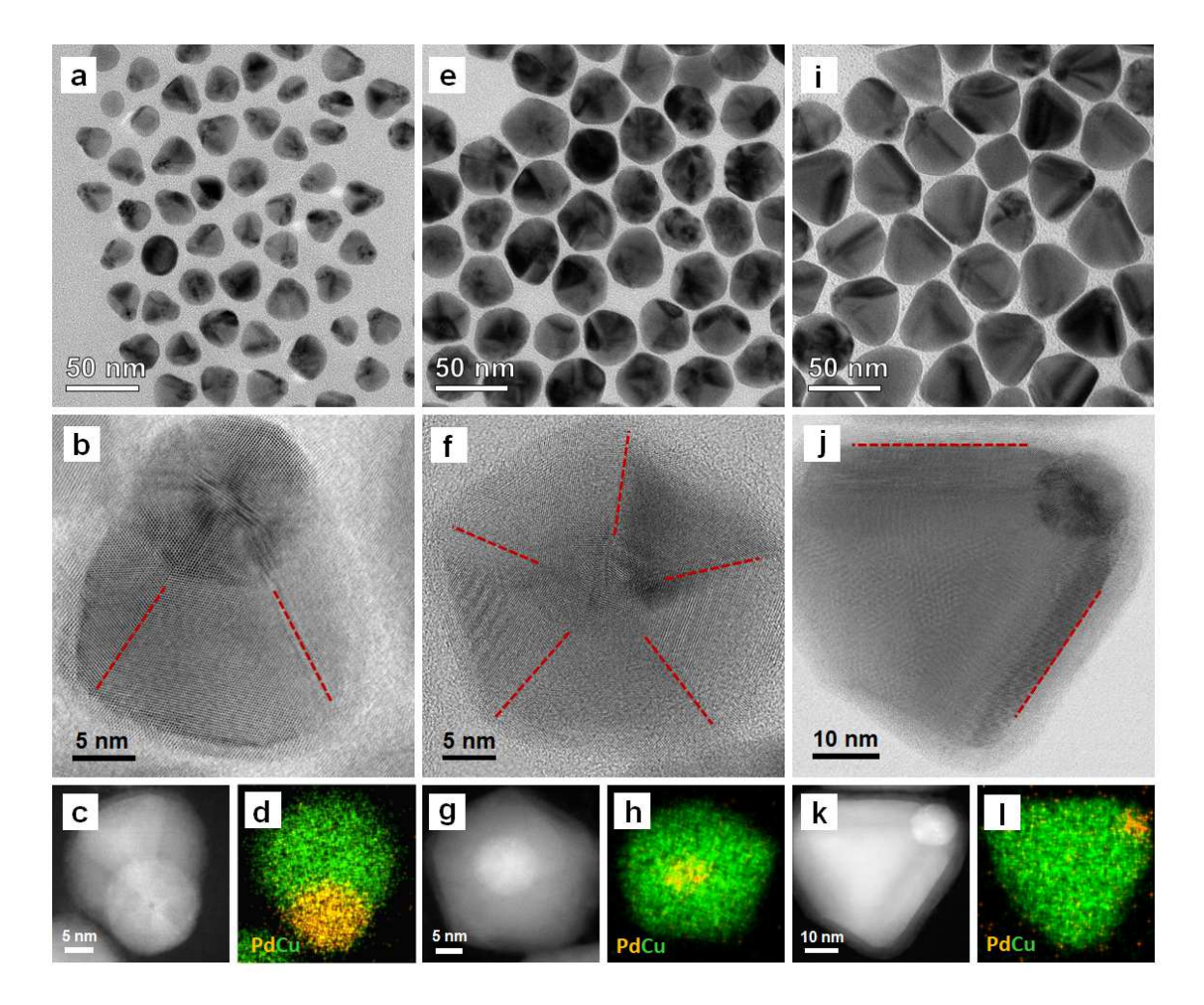


Figure 2. Characterizations of the Pd-Cu Janus nanocrystals prepared using the standard protocols: (a) TEM, (b) BF-, (c) DF-STEM, and (d) EDX mapping images of the pentagonal bipyramids; (e) TEM, (f) BF-, (g) DF-STEM, and (h) EDX mapping images of the decahedra; (i) TEM, (j) BF-, (k) DF-STEM, and (l) EDX mapping images of the truncated bitetrahedra. The yellow and green colors in (d), (h), and (l) correspond to Pd and Cu, respectively. The red dashed lines indicate the twin boundaries.

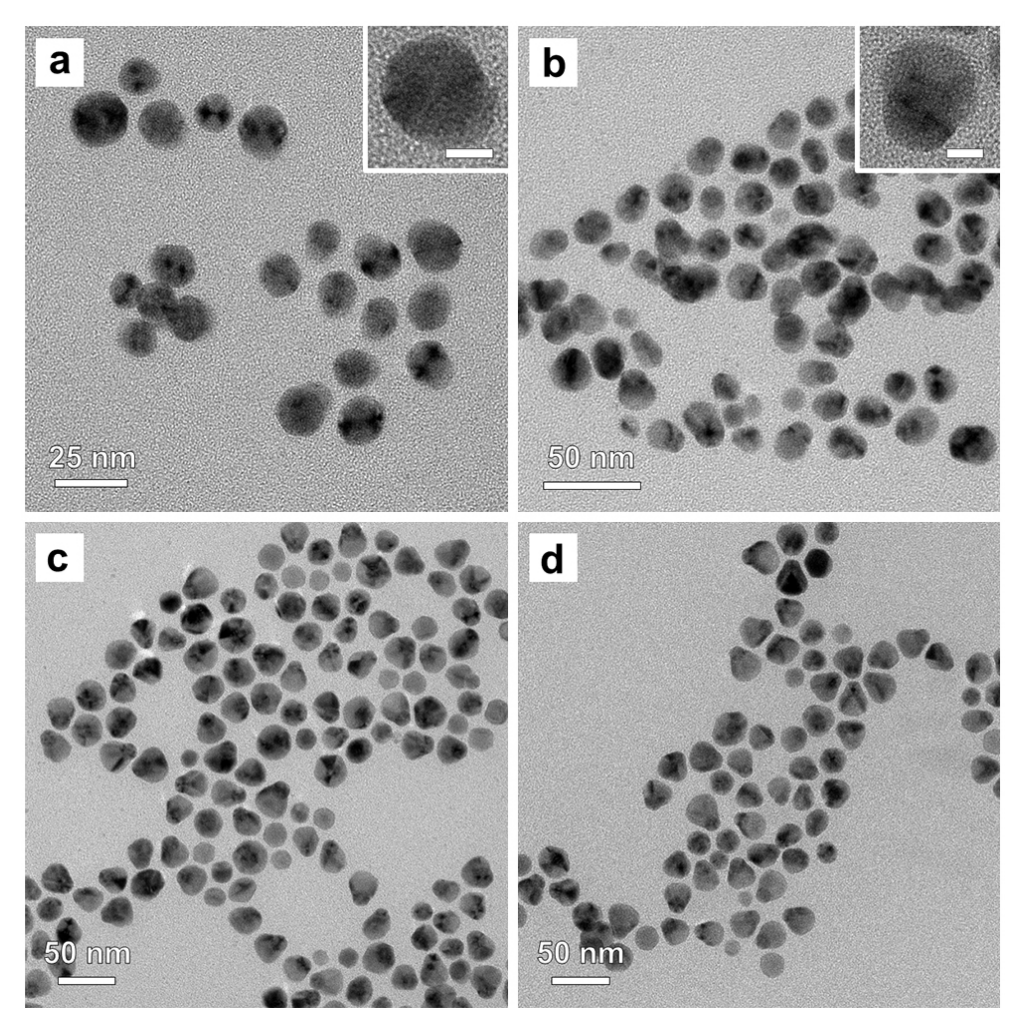


Figure 3. TEM images of the Pd-Cu pentagonal bipyramids prepared using the standard protocol except for the variation in reaction time: (a) 30, (b) 60, (c) 90, and (d) 120 min, respectively. The scale bars in the inset of (a) and (b) are 8 nm.

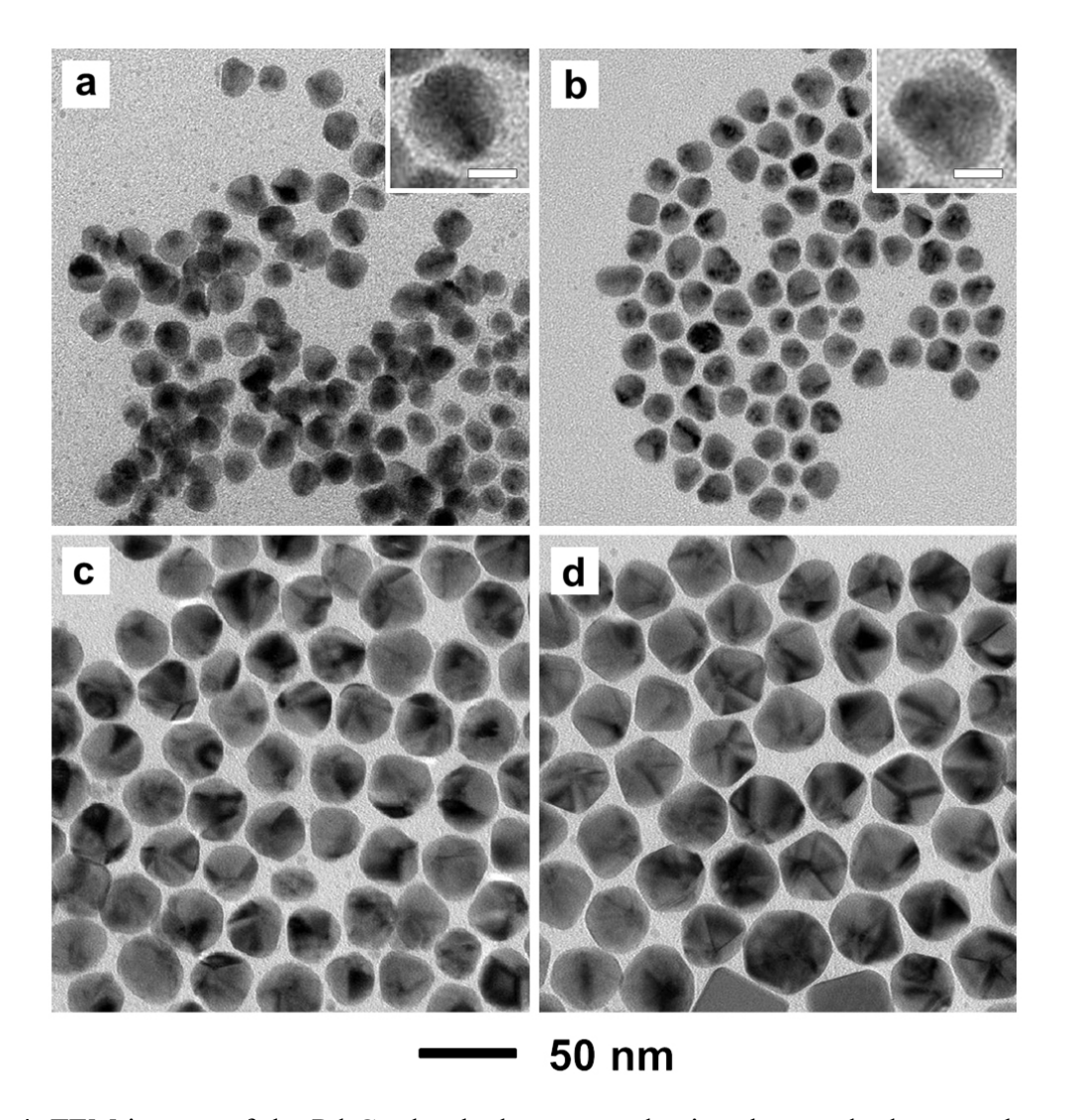


Figure 4. TEM images of the Pd-Cu decahedra prepared using the standard protocol except for the variation in reaction time: (a) 10, (b) 20, (c) 60, and (d) 120 min, respectively. The scale bars in the insets of (a) and (b) are 10 nm.

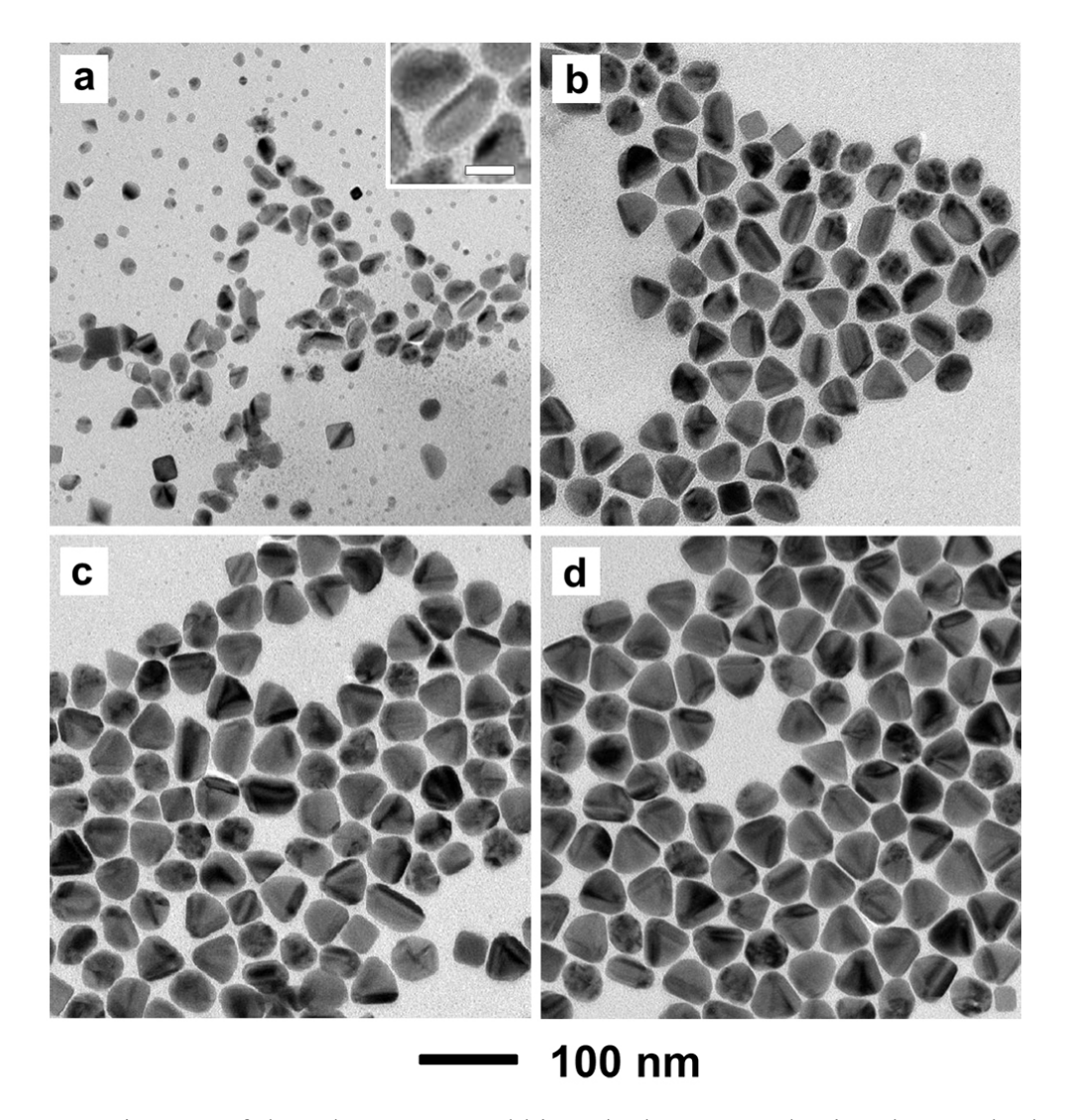


Figure 5. TEM images of the Pd-Cu truncated bitetrahedra prepared using the standard protocol except for the variation in reaction time: (a) 30, (b) 60, (c) 90, and (d) 120 min, respectively. The scale bars in the inset of (a) is 20 nm.

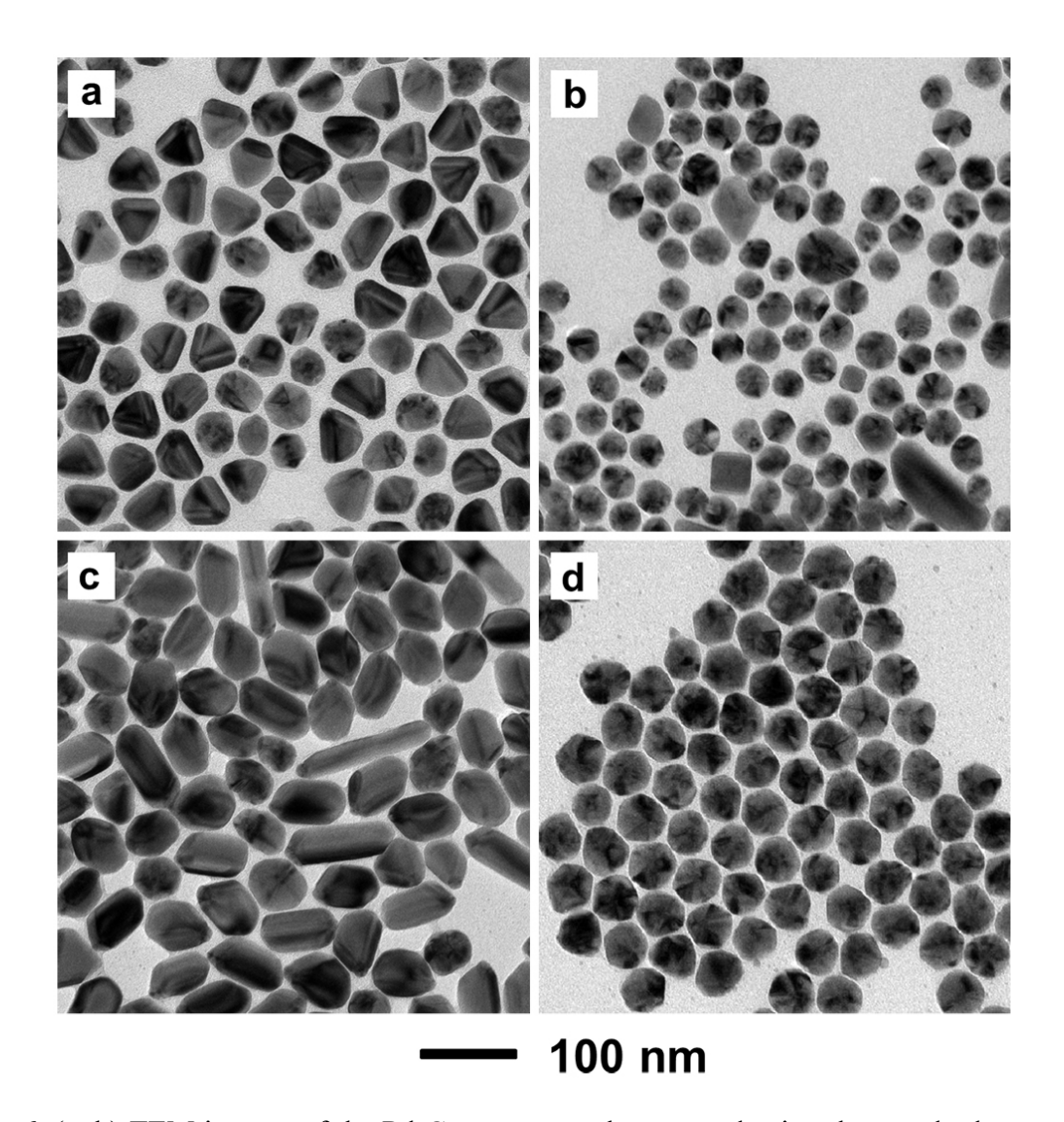


Figure 6. (a, b) TEM images of the Pd-Cu nanocrystals prepared using the standard protocol for decahedra except for the variation in the amount of HDA from 45 mg to (a) 22.5 and (b) 90 mg; (c, d) TEM images of the Pd-Cu nanocrystals prepared using the standard protocol for truncated bitetrahedra except for the variation in the amount of HDA from 45 mg to (c) 35 and (d) 90 mg.

Table 1. The dominant shapes of Pd-Cu nanocrystals prepared using different amounts of CuCl₂ and HDA (pentagonal bipyramid and truncated bitetrahedron are abbreviated as pBP and tBT, respectively; N/A represents no product obtained).

| CuCl ₂ (mg) | 1.05 | 2.1 | 5.25 | 10.5 |
|------------------------|------|------------|------------|------------|
| HDA (mg) | | | | |
| 22.5 | pBP | decahedron | tBT | N/A |
| 45 | рВР | pBP | decahedron | tBT |
| 90 | рВР | pBP | decahedron | decahedron |

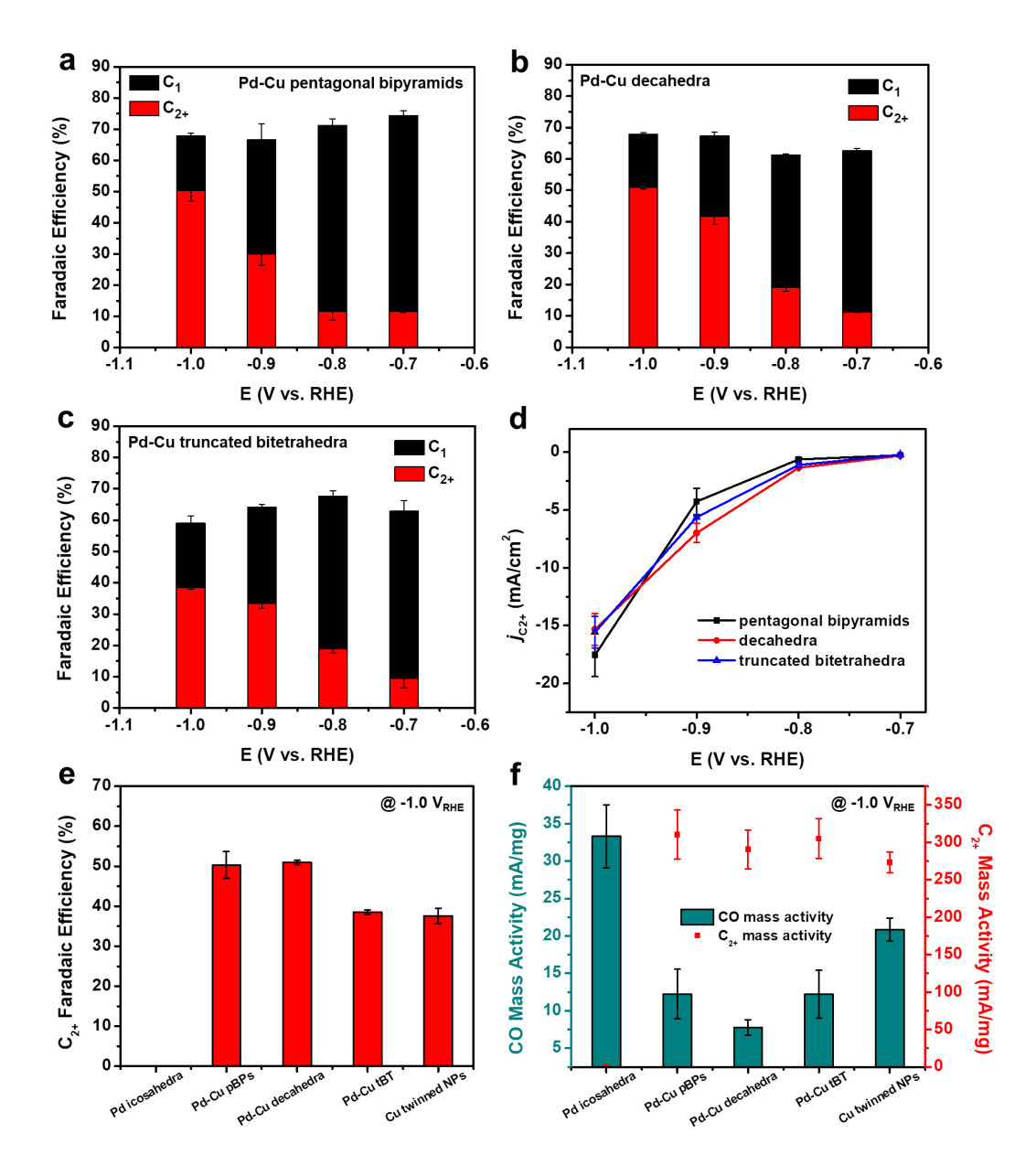


Figure 7. Products for the electrochemical reduction of CO₂ in the presence of catalysts based on the different types of Pd-Cu nanocrystals: (a–c) FEs of (a) pentagonal bipyramids, (b) decahedra, (c) truncated bitetrahedra, and (d) partial current density toward C₂₊ products normalized to the geometric area of the electrode. (e) The FEs of C₂₊ products and (f) the mass activities toward the production of CO and C₂₊ species at -1.0 V_{RHE} with Pd-Cu Janus nanocrystals, Pd icosahedra, and Cu twinned nanoparticles serving as the catalysts. In (e) and (f), the pentagonal bipyramids, truncated bitetrahedra, and nanoparticles are abbreviated as pBPs, tBT, and NPs, respectively.

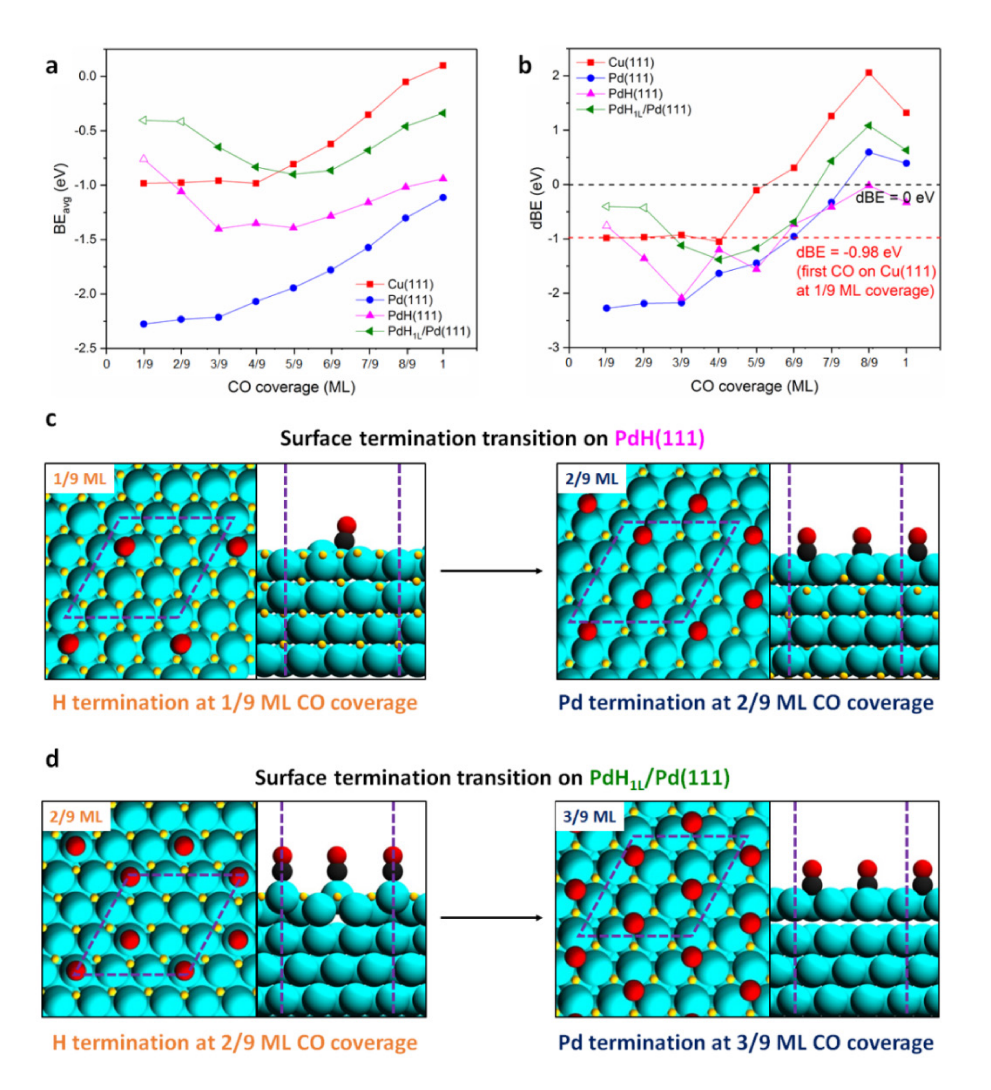


Figure 8. Calculated (a) average and (b) differential binding energies of CO on Cu(111) (red), Pd(111) (blue), PdH(111) (pink), and PdH_{1L}/Pd(111) (green) as a function of CO coverage. Black dashed line in (b) indicates a dBE value of 0 eV (thermal-neutral adsorption). Red dashed line in (b) indicates a dBE value of -0.98 eV (BE of CO on a clean Cu(111) surface at 1/9 ML coverage). For PdH(111) and PdH_{1L}/Pd(111), open symbol indicates that H termination is preferred; solid symbol indicates that Pd termination is preferred. (c) Illustration of transition from H termination to Pd termination on PdH(111) when CO coverage increases from 1/9 to 2/9 ML. (d) Illustration of transition from H termination to Pd termination on PdH_{1L}/Pd(111) when CO coverage increases from 2/9 to 3/9 ML. In (c) and (d), top and side views are shown side by side in each pair of images. Color code: cyan – Pd; yellow – H; black – C; red – O. Dashed lines denote the (3 × 3) surface unit cell.

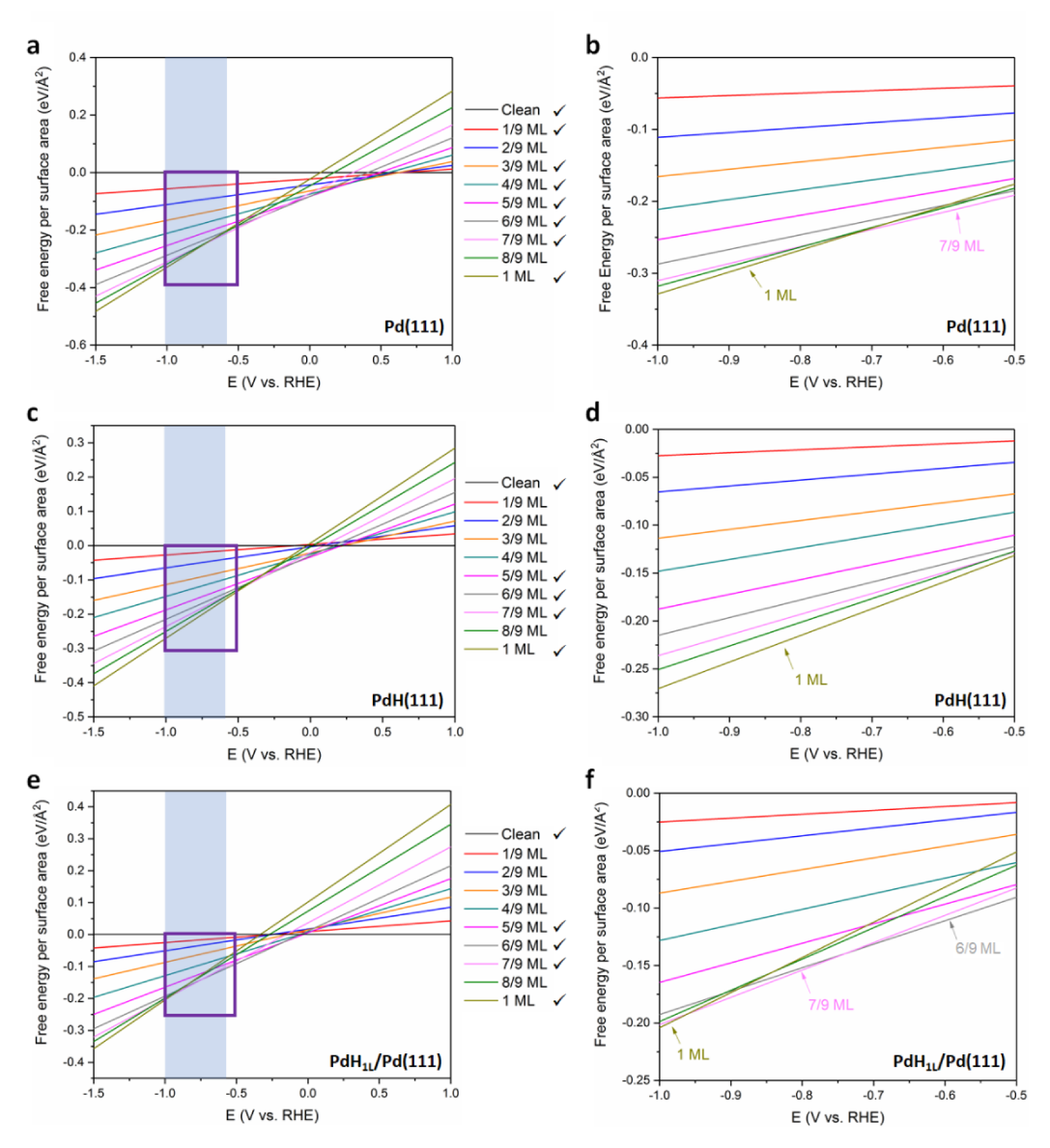
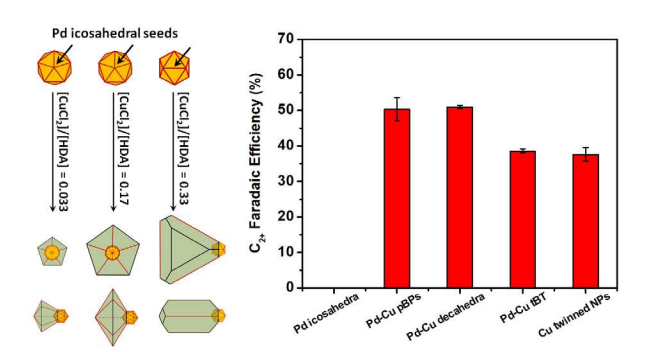


Figure 9. Calculated Pourbaix phase diagram for (a, b) CO on Pd(111), (c, d) CO on PdH(111), and (e, f) CO on PdH_{1L}/Pd(111) at room temperature under the electrochemical conditions for CO₂ reduction. The free energy per surface area for each CO coverage up to 1 ML is plotted as a function of the applied potential. At each potential, the most stable surface coverage is the one with the lowest free energy value. In the legend, those coverages marked with tick marks appear as the most stable phases under certain potentials; the remaining phases are not expected to be observable. The range of applied potential evaluated experimentally in this work (-0.7 to -1.0 V_{RHE}) is denoted by the shaded area on (a), (c), and (e). Enlarged views of the boxed area in (a), (c), and (e) are shown in (b), (d), and (f), respectively.

Table 2. Phase-diagram-predicted CO coverage under electrochemical CO_2 reduction conditions (room temperature, -0.7 to -1.0 V_{RHE}) on Pd(111) and PdH surfaces and comparison with the CO coverage required for CO spillover to Cu(111).

| Same a co | Predicted CO coverage under | CO coverage required for CO |
|----------------------------|---|-----------------------------|
| Surface | CO ₂ reduction conditions (ML) | spillover to Cu(111) (ML) |
| Pd(111) | 7/9 or 1 | 6/9 |
| PdH(111) | 1 | 5/9 |
| PdH _{1L} /Pd(111) | 6/9, 7/9, or 1 | 5/9 |
| $PdH_{2L}/Pd(111)$ | 7/9 or 1 | 5/9 |
| $PdH_{3L}/Pd(111)$ | 7/9 or 1 | 5/9 |
| PdH _{comp} (111) | 6/9, 7/9, or 1 | 5/9 |

Table of Contents



Supporting Information for

Kinetically-Controlled Synthesis of Pd-Cu Janus Nanocrystals with Enriched Surface Structures and Enhanced Catalytic Activities toward CO₂ Reduction

Zhiheng Lyu,^{†,+} Shangqian Zhu,^{¥,+} Lang Xu,^{∥,+} Zitao Chen,[‡] Yu Zhang,^{‡,¥} Minghao Xie,[†] Tiehuai Li,[¥] Shan Zhou,[†] Jingyue Liu,[#] Miaofang Chi,[§] Minhua Shao,^{¥,⊥},* Manos Mavrikakis,^{∥,*} and Younan Xia^{†,‡,*}

[†]School of Chemistry and Biochemistry, Georgia Institute of Technology, Atlanta, Georgia 30332, United States

*Department of Chemical and Biological Engineering, The Hong Kong University of Science and Technology, Clear Water Bay, Kowloon, Hong Kong, China

Department of Chemical and Biological Engineering, University of Wisconsin-Madison, Madison, Wisconsin 53706, United States

[‡]The Wallace H. Coulter Department of Biomedical Engineering, Georgia Institute of Technology and Emory University, Atlanta, Georgia 30332, United States

*Department of Physics, Arizona State University, Tempe, Arizona 85287, United States *Center for Nanophase Materials Science, Oak Ridge National Laboratory, Oak Ridge, Tennessee 37831, United States

¹Hong Kong Branch of the Southern Marine Science and Engineering Guangdong Laboratory,
The Hong Kong University of Science and Technology, Clear Water Bay, Kowloon, Hong Kong,
China

^{*}Address correspondence to younan.xia@bme.gatech.edu (for synthesis), kemshao@ust.hk (for electrocatalytic measurement), and manos@engr.wisc.edu (for computational work)

*These authors contributed equally to this work.

Experimental Section

Chemicals and Materials. Sodium tetrachloropalladate(II) (Na₂PdCl₄, 98%), copper(II) chloride dihydrate (CuCl₂·2H₂O, 99.0%), copper(II) acetate (Cu(ac)₂, 98%), hexadecylamine (HDA, 98%), D-(+)-glucose (C₆H₁₂O₆, 99.5%), poly(vinyl pyrrolidone) (PVP, molecular weight \approx 55,000), sodium chloride (NaCl, >99%), diethylene glycol (DEG, lot no. BCBS2365V), potassium hydrogen carbonate (KHCO₃, 99.7%), 5% Nafion solution, and phenol were all obtained from Sigma-Aldrich. Ethanol (200 proof) was obtained from Pharmco Products. Throughout the experiments, we used deionized (DI) water with a resistivity of 18.2 M Ω ·cm at room temperature.

Synthesis of 12-nm Pd Icosahedral Seeds. The seeds were prepared using a protocol from our previous work.¹ Typically, 80 mg of PVP was dissolved in 2 mL of DEG hosted in a 20-mL vial and the solution was heated at 130 °C in an oil bath under magnetic stirring for 10 min. Afterwards, 1 mL of DEG containing 15.5 mg of Na₂PdCl₄ was injected in one shot with a pipette. The vial was then capped and continued with heating at 130 °C for 3 h. The solid product was collected by centrifugation at a speed of 26,500 x g, washed once with acetone and twice with water to remove DEG and excess PVP. The Pd icosahedra were finally dispersed in water at a concentration of 1.1 mg·mL⁻¹ for use as seeds in the synthesis of Pd-Cu nanocrystals.

Synthesis of Pd-Cu Janus Nanocrystals. In a standard synthesis of Pd-Cu pentagonal bipyramids, 50 μL of the suspension of Pd icosahedral seeds was added into a 5-mL aqueous solution containing 45 mg of HDA, 25 mg of glucose, and 1.05 mg of CuCl₂·2H₂O. The mixture was magnetically stirred overnight at room temperature. To remove the oxygen trapped in the vial, Ar was blown over the solution for 5 min before the vial was tightly capped, transferred into an oil bath set to 100 °C, and heated for 3 h under magnetic stirring. The solid product was collected by centrifugation at a speed of 13,300 x g, washed once with water and twice with ethanol to remove the excess HDA, and finally re-dispersed in ethanol for further characterization. For Pd-Cu decahedra and truncated bitetrahedra, similar protocols were used except that the amount of CuCl₂·2H₂O was increased by five and ten times to 5.25 and 10.5 mg, respectively.

Structural and Compositional Analysis. Transmission electron microscopy (TEM) images were taken using a Hitachi HT7700 microscope. A small drop of the particle suspension was placed on a carbon-coated Cu grid, followed by drying under ambient conditions. Scanning

transmission electron microscope (STEM) images were taken using an aberration-corrected FEI Titan 80–300 kV TEM/STEM microscope at an accelerating voltage of 300 kV, with a probe convergence angle of 30 mrad and a large inner collection angle of 65 mrad to provide a nominal image resolution of 0.7 Å. A portion of the aberration-corrected STEM imaging was performed on a JEM-ARM200F microscope with a spatial resolution of 0.08 nm. Energy dispersive X-ray (EDX) mapping was obtained using a Hitachi HD2700 STEM microscope at an acceleration voltage of 200 kV.

Ultraviolet-visible (UV-vis) extinction spectra were recorded on a Cary 60 spectrometer (Agilent Technologies, Santa Clara, CA). The samples were washed twice with water and then dispersed in water for UV-vis characterization. The Cu and Pd contents in the samples were determined using an inductively coupled plasma mass spectrometry (ICP-MS, NexION 300Q, Perkin-Elmer). X-ray diffraction (XRD) patterns were recorded using an X'Pert PRO Alpha-1 diffractometer equipped with a 1.8 kW ceramic copper tube source (PANalytical, Almelo, Netherlands). X-ray photoelectron spectroscopy (XPS) data were obtained on a Thermo K-Alpha spectrometer with an Al Kα source (hv = 1486.6 eV). For XRD and XPS measurements, the samples were washed twice with water, twice with ethanol, and then dropped onto glass slides and dried under ambient conditions.

Preparation of Working Electrode. The as-prepared Pd-Cu nanocrystals were loaded onto a carbon support (Vulcan XC72) at a Cu loading ratio of 20% w/w via ultrasonication in an ice bath for 30 min, followed by washing with ethanol twice. The concentrations of Cu and Pd in all three samples, together with the molar ratio of Cu to Pd, are listed in Table S3 (measured by ICP-MS). The catalysts were then re-dispersed in 0.95 mL of ethanol and 50 μL of 5% Nafion with a Cu concentration of 1 mg/mL. For each measurement, 40 μg of the catalyst (based on the mass of Cu) was dropped onto a pre-cleaned glassy carbon electrode (10 mm in diameter) and dried under ambient conditions. For the Pd icosahedra and Cu twinned nanoparticles, the same procedure was applied except for the loading of 40 μg of Pd or Cu onto the electrode.

Electrochemical Measurements and Sample Analysis. A gastight H-type cell separated by a Nafion 117 membrane (Sigma Aldrich) was used for analyzing the electrochemical reduction of CO₂. Each compartment was filled with 40 mL of 0.5 M KHCO₃ solution saturated with CO₂ (pH = 7.3). An Ag/AgCl electrode (Gaossunion) was used as the reference electrode while a Pt mesh served as the counter electrode. The potentials were later converted to values with a

reference to RHE using the equation of E (vs. RHE) = E (vs. Ag/AgCl) + $E_{Ag/AgCl}$ + 0.0591 × (7.3 – 1.1), where $E_{Ag/AgCl}$ is the potential of the Ag/AgCl electrode measured in the 0.1 M HClO₄ solution (pH = 1.1) with reference to RHE. Before carrying out the electrochemical measurement, CO₂ (99.999%, Asia Pacific Gas Enterprise Co., LTD) was purged into the KHCO₃ solution for 1 h. During the measurement, CO₂ was continuously purged into each compartment through mass flow controllers (Sevenstar) with a flow rate of 20 sccm. To release the bubbles trapped on the working electrode, the electrolyte solution was magnetically stirred at a rate of 700 rpm.

The gas products were analyzed using an online gas chromatography (GC2060, Ramiin, Shanghai) equipped with the flame ionization detector (FID) and thermal conductivity detector (TCD). Sampling was conducted sequentially at 15, 28, 41, and 54 min and the total charges collected in the 30 s prior to each sampling were used to calculate the current density. A series of standard gas mixtures were used to establish the calibration curves for H_2 , CO, CH4, and C_2H_4 (balanced with Ar; Shanghai Haizhou Special Gas Co., LTD). After 1 h of electrolysis, the liquid products in the KHCO3 solution were collected and analyzed using a Varian 500 MHz nuclear magnetic resonance (NMR) spectrometer. Specifically, 50 μ L of 500 \times 10⁻⁶ M phenol contained D2O (J&K Chemical) was added into 450 μ L of the KHCO3 solution and the mixture was then subjected to NMR characterization. The calibration curves were established from a series of standard solutions (0.5 M KHCO3 solutions containing 10, 20, and 100 \times 10⁻⁶ M of formate, methanol, ethanol, acetate, and n-propanol). The activity and selectivity of each catalyst were measured at least three times, from which the standard errors were derived.

The electrochemically active surface area (ECSA) of the Pd-Cu Janus nanocrystals in each catalyst was derived from the amount of charges required for the formation of a Cu_2O monolayer.² Cyclic voltammograms (CVs) were recorded in the electrolysis cell with Ar-purged 0.1 M aqueous KOH serving as the electrolyte. A potential range of -0.233 to 0.766 V_{RHE} was employed and the amount of catalyst used in each measurement was fixed to 40 μ g. The ECSA was estimated by dividing the amount of charges associated with the anodic peak at around 0.6 V_{RHE} with 360 μ C/cm², a value associated with the formation of a Cu_2O monolayer.

In Situ Attenuated Total Reflection Infrared (ATR-IR) Spectroscopy Measurements. Setups for in situ ATR-IR measurements were conducted using a protocol described previously.³ Real-time ATR-IR spectra were collected during linearly sweeping the catalyst-loaded Au/Si

prism working electrode at potentials from 0.1 to $-1.0~V_{RHE}$ with a scanning rate of 5 mV s⁻¹ in a CO_2 -saturated $0.5~M~KHCO_3$ solution. Each spectrum was collected with 44 scans (collection duration of 10~s) at a resolution of $8~cm^{-1}$ and named according to the end potential. The first spectrum was used as the IR background.

Table S1. Comparison of Pd-Cu Janus nanocrystals in this work with other Cu-based catalysts reported in literature, with 0.5 M KHCO₃ serving as the electrolyte for all the measurements listed below.

| Catalyat | E va DHE | Onset potential | Fa | aradaic 6 | Ref | | |
|---|-----------|-----------------|-------|-----------------|----------|-----------|-----------|
| Catalyst | E vs. RHE | for C_{2+} | H_2 | CH ₄ | C_2H_4 | C_{2^+} | Kei |
| Pd-Cu pentagonal bipyramids | -1.0 | -0.7 | 28.5 | 4.8 | 31.3 | 50.3 | This work |
| Pd-Cu decahedra | -1.0 | -0.7 | 25.9 | 6.2 | 34.0 | 51.0 | This work |
| Pd-Cu truncated bitetrahedra | -1.0 | -0.7 | 35.7 | 10.2 | 25.4 | 38.5 | This work |
| Cu octahedra | -1.0 | -0.85 | N/A | 15 | 7.5 | N/A | 4 |
| Cu cubes | -1.05 | -0.8 | N/A | 25 | 21 | N/A | 4 |
| Polydopamine-coated Cu nanowires | -0.93 | -0.7 | 10 | 29 | 17 | N/A | 5 |
| Pd-decorated Cu | -0.96 | -0.85 | 30 | 46 | 5 | N/A | 6 |
| Branched CuO | -1.0 | <-0.7 | 53 | 5 | 36 | ~36 | 7 |
| Cubic Cu ₂ O | -0.9 | <-0.7 | 75 | 2 | 25 | ~25 | 7 |
| Copper-porphyrin complex | -1.0 | -0.9 | N/A | 27 | 17 | N/A | 8 |
| Electrodeposited Cu ₂ O on carbon | -1.2 | -0.7 | 61 | ~0 | 25.5 | 25.5 | 9 |
| Oxide-derived Cu-foam ^(a) | -0.8 | -0.5 | 15 | 0 | 20 | 55 | 10 |
| Cu wafer ^(a) | -0.8 | -0.6 | 27 | 10 | 18 | 26 | 10 |
| Cu particles on pyridinic- N rich graphene | -0.9 | -0.9 | N/A | 0.9 | 19 | 20 | 11 |

⁽a) The electrolyte is 0.5 M NaHCO₃.

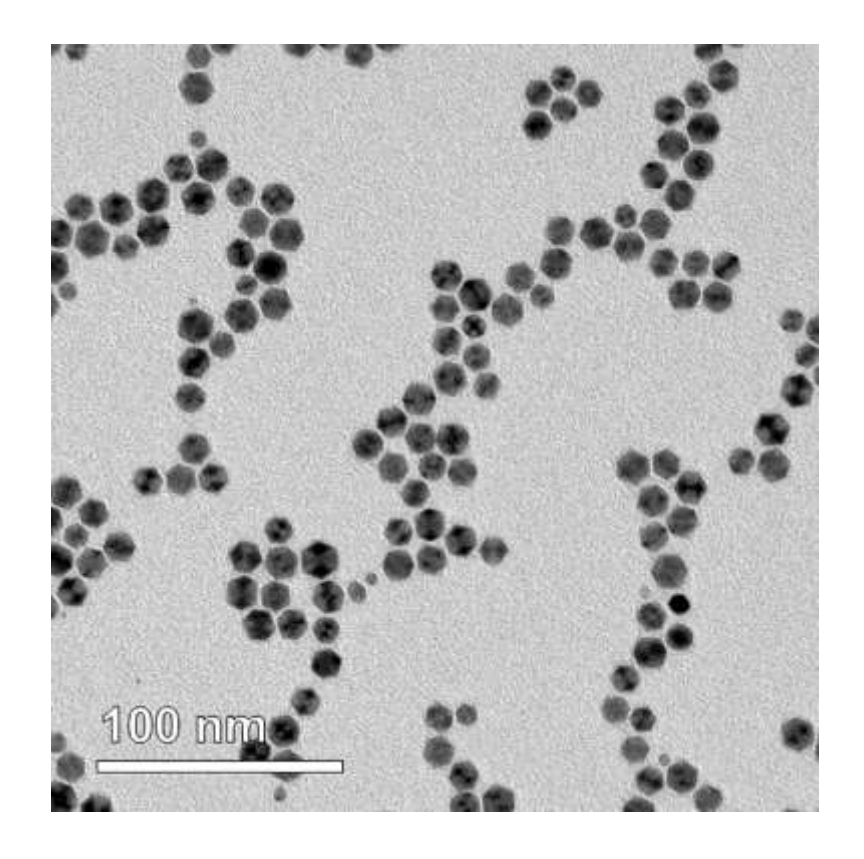


Figure S1. TEM image of the Pd icosahedra that served as seeds for the growth of Cu.

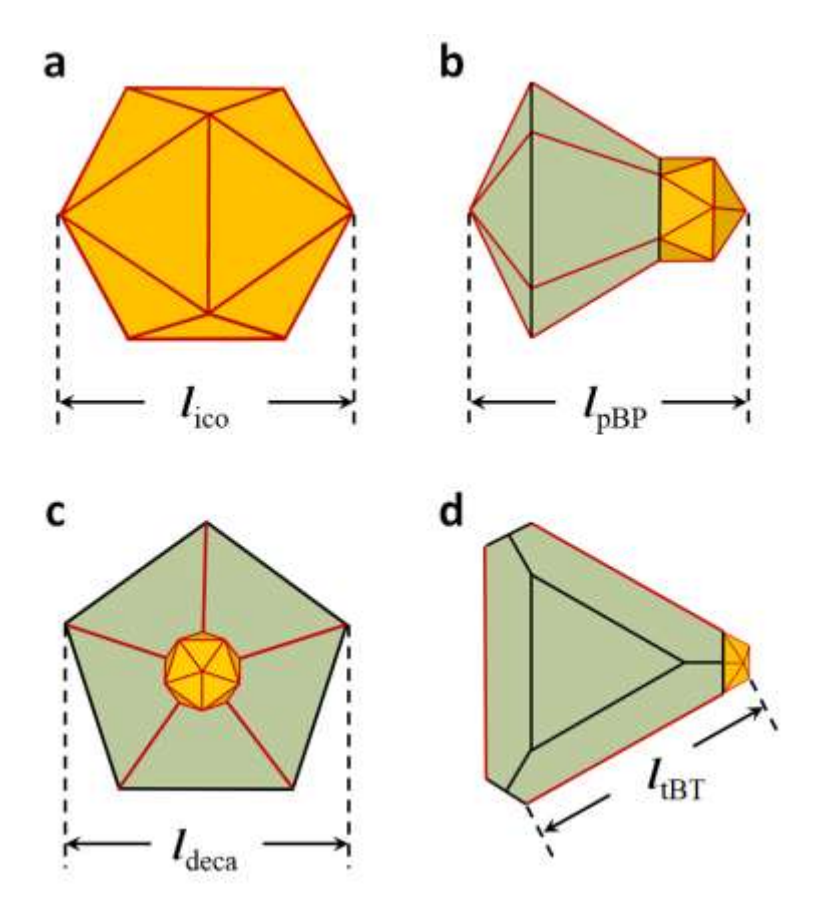


Figure S2. Definitions of the size or edge length of (a) an icosahedron (l_{ico}), (b) a pentagonal bipyramid (l_{pBP}) projected along the axis parallel to the pentagonal base, (c) a decahedron (l_{deca}) projected along the axis perpendicular to the pentagonal base, and (d) a truncated bitetrahedron (l_{tBT}) projected along the axis perpendicular to the triangular base.

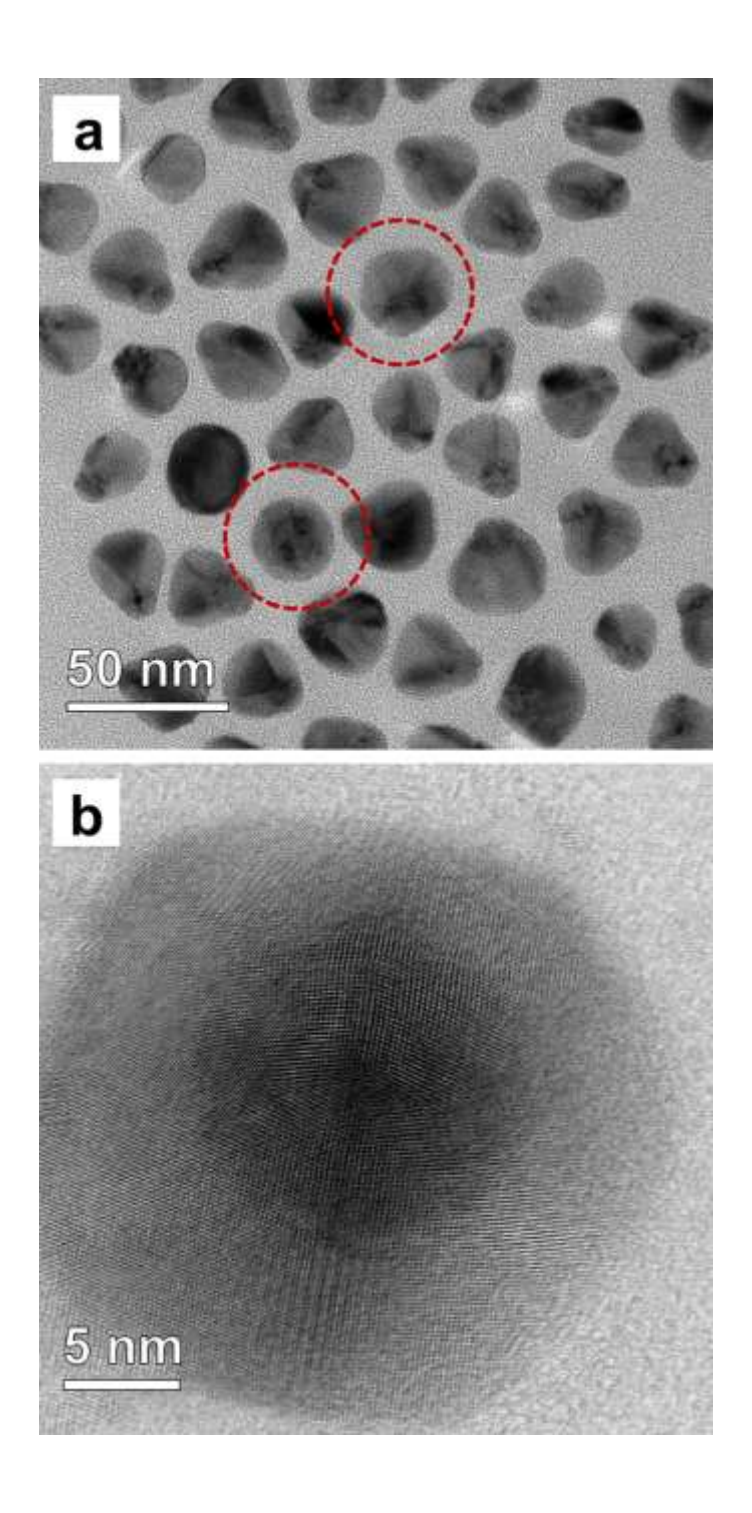


Figure S3. (a) TEM image of the Pd-Cu pentagonal bipyramids prepared using the standard protocol. The red circles indicate the nanocrystals projected along the axis perpendicular to the pentagonal base. (b) Bright-field (BF) STEM image showing a Pd-Cu pentagonal bipyramid projected along the axis perpendicular to the pentagonal base.

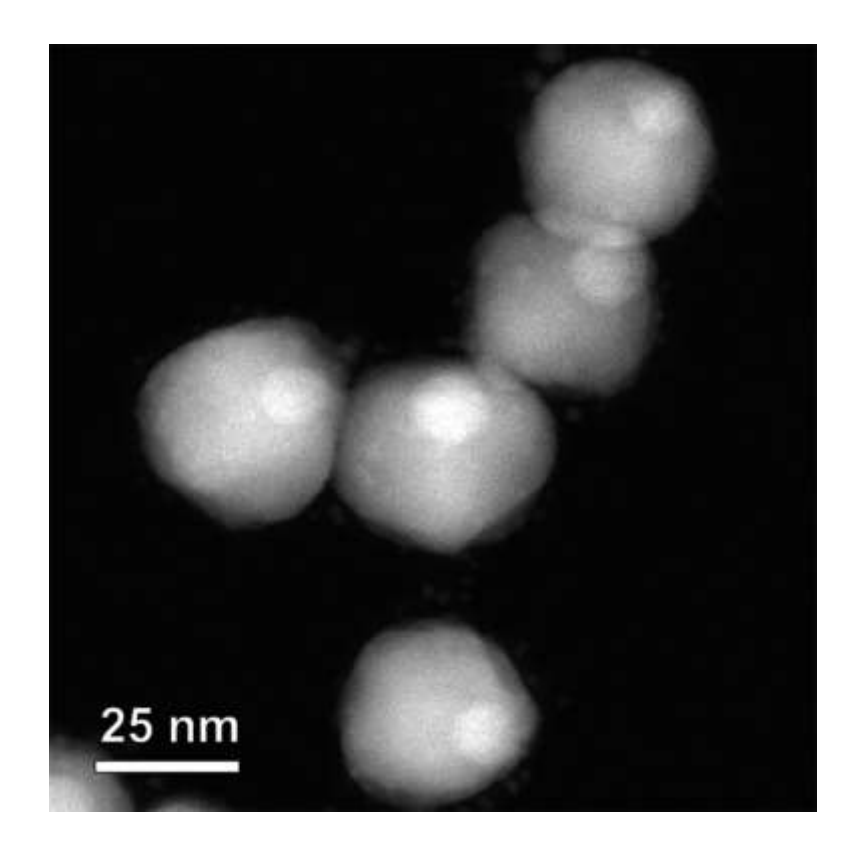


Figure S4. Dark-field (DF) STEM image showing the position of the Pd icosahedral seed (with a brighter contrast) in each Pd-Cu decahedron.

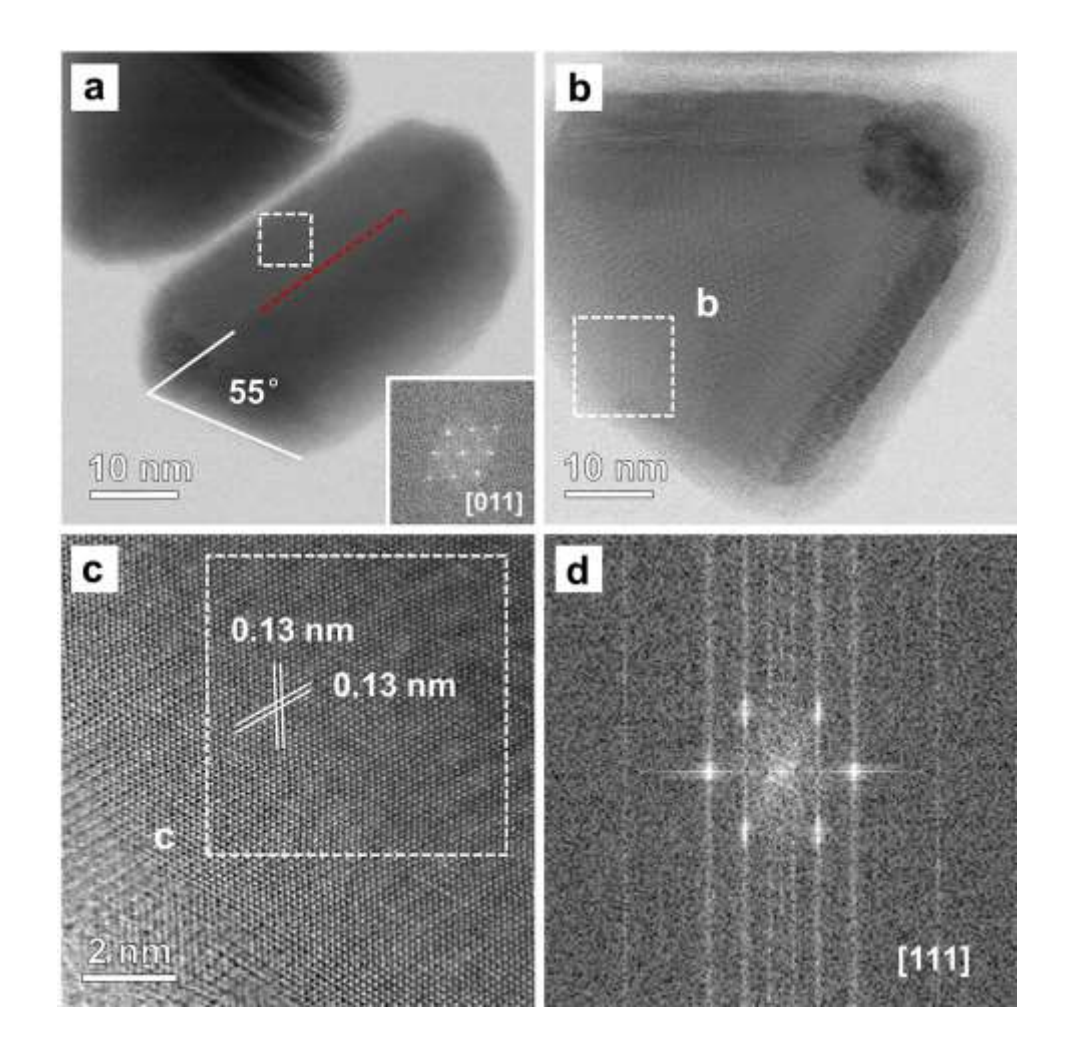


Figure S5. (a) BF-STEM image of a truncated bitetrahedron viewed along <011> zone axis. The angle between side face and triangular base was measured to be 55°. The twin boundary is marked by a red dashed line. (b) BF-STEM image of the truncated bitetrahedron shown in Figure 2j; (c) BF-STEM image taken from the region marked by a box in (b); (d) Fast Fourier transform (FFT) pattern of the region marked in (c).

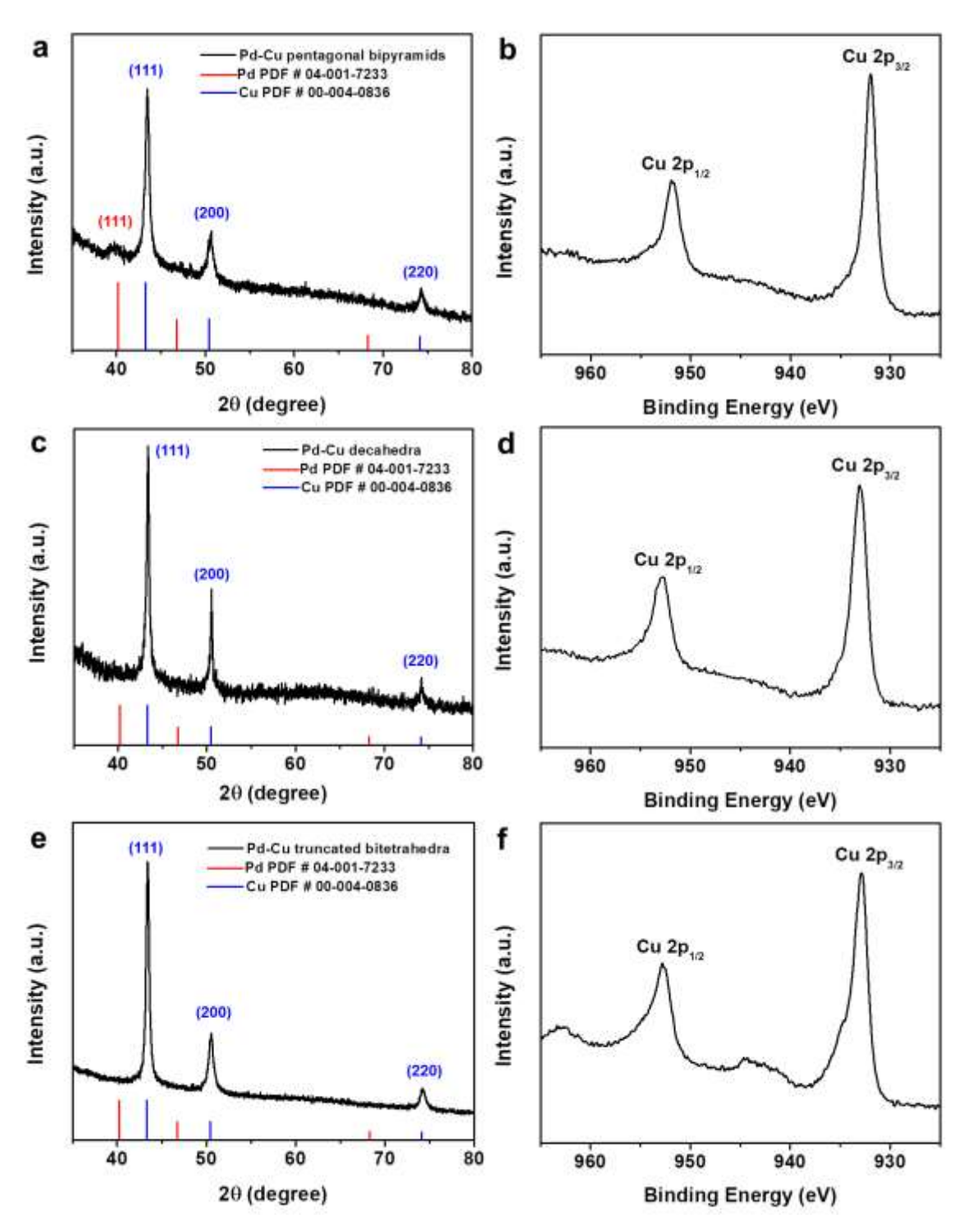


Figure S6. Powder XRD patterns and XPS spectra recorded from samples of Pd-Cu nanocrystals featuring the shapes of (a, b) pentagonal bipyramid, (c, d) decahedron, and (e, f) truncated bitetrahedron, respectively.

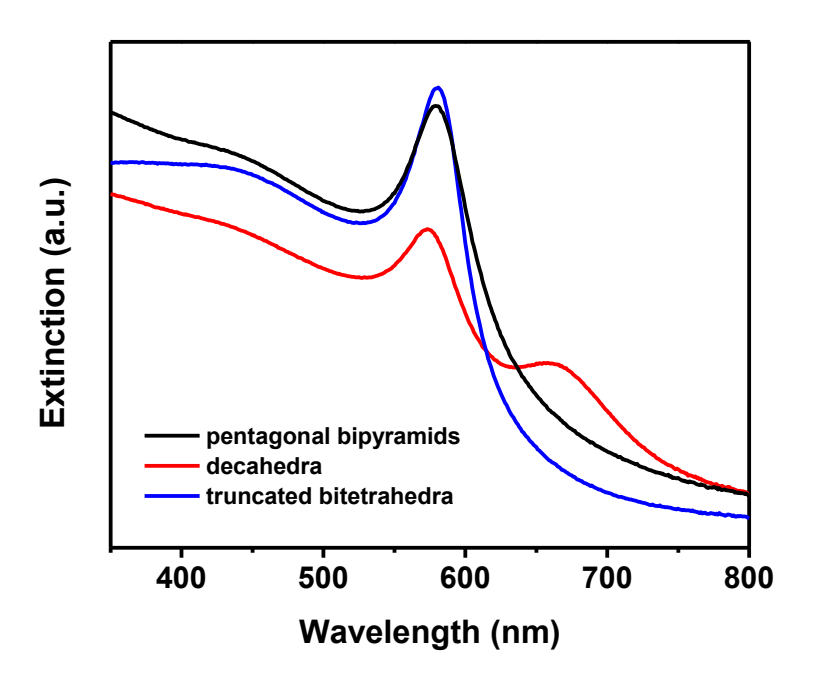


Figure S7. UV-vis spectra recorded from aqueous suspensions of the Pd-Cu nanocrystals with different shapes.

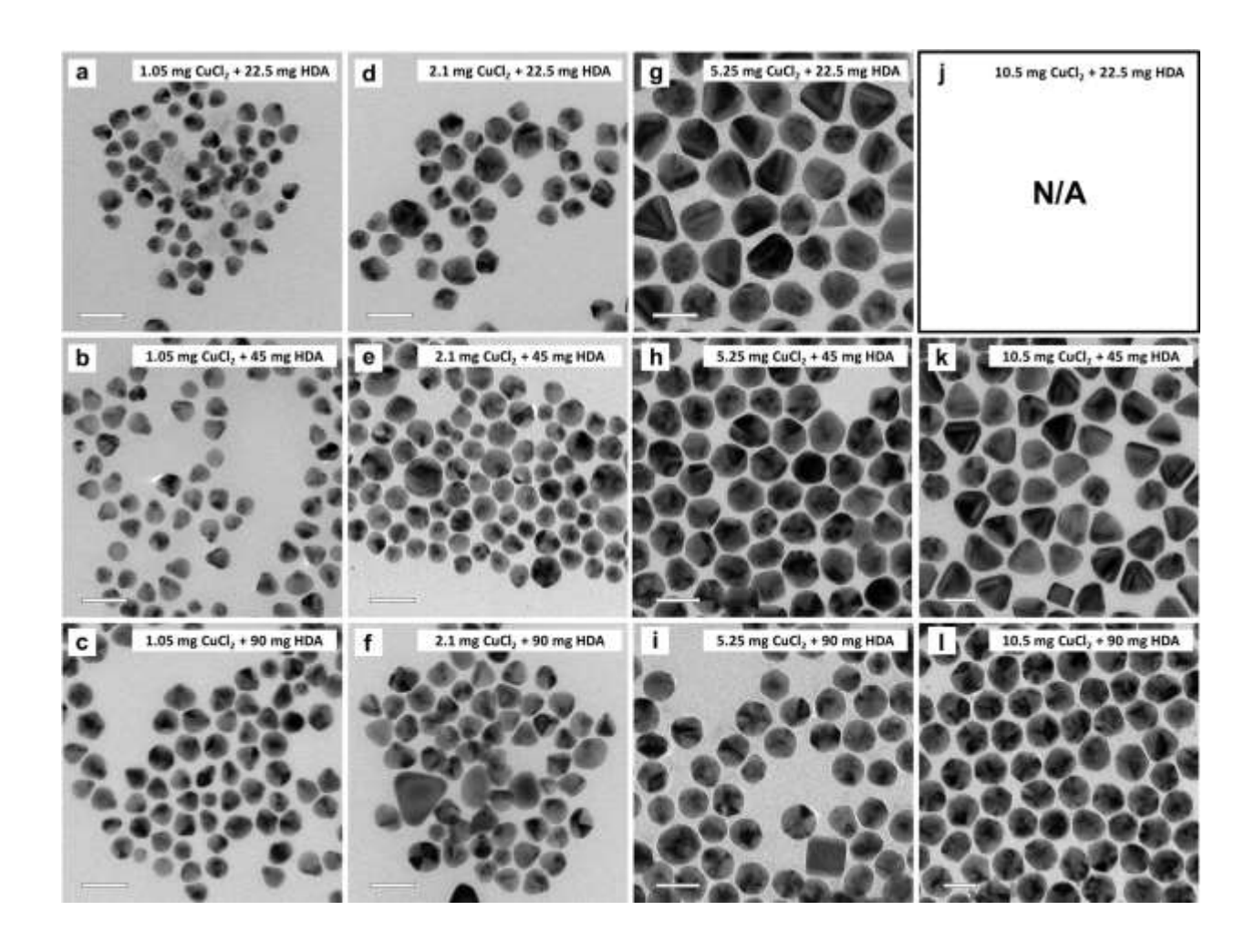


Figure S8. TEM images of the samples in Table 1, with N/A indicating that no product was obtained. The scale bars are 50 nm.

The Role of Glucose. In general, the reduction kinetics of the Cu(II) precursor depends on the concentrations of not only the coordination ligand and precursor but also the reductant. To look into the explicit role of glucose in the formation of Cu nanocrystals, we did another set of experiments by fixing the amount of HDA at 45 mg while varying the concentrations of the Cu(II) precursor and glucose (Table S2 and Figure S9). Surprisingly, increasing the concentration of glucose did not bring any change to the shape of the resultant nanocrystals. To be specific, when 1.05, 5.25, and 10.5 mg of CuCl₂ were used, the dominant shapes of the Pd-Cu nanocrystals were pentagonal bipyramid, decahedron, and truncate bitetrahedron, regardless of the amount of glucose added as long as it was controlled in the range of 13.9–111.0 mM. As the concentration of glucose was increased, we also observed an increase in proportion for the impurities, including cubes and right bipyramids purely made of Cu. Along with the acceleration in reduction for the Cu(II) precursor, the increase in homogeneous nucleation and thus the consumption of Cu atoms reduced the amount of Cu actually deposited on the Pd seeds, resulting in the formation of almost identical Pd-Cu products even though the concentration of reductant was increased.

Table S2. The dominant shapes of Pd-Cu nanocrystals in the samples prepared using different amounts of CuCl₂ and glucose, with pentagonal bipyramid and truncated bitetrahedron being abbreviated as pBP and tBT, respectively.

| CuCl ₂ (mg) | 1.05 | 5.25 | 10.5 |
|------------------------|------|------------|------|
| 12.5 | pBP | decahedron | tBT |
| 50 | рВР | decahedron | tBT |
| 100 | рВР | decahedron | tBT |

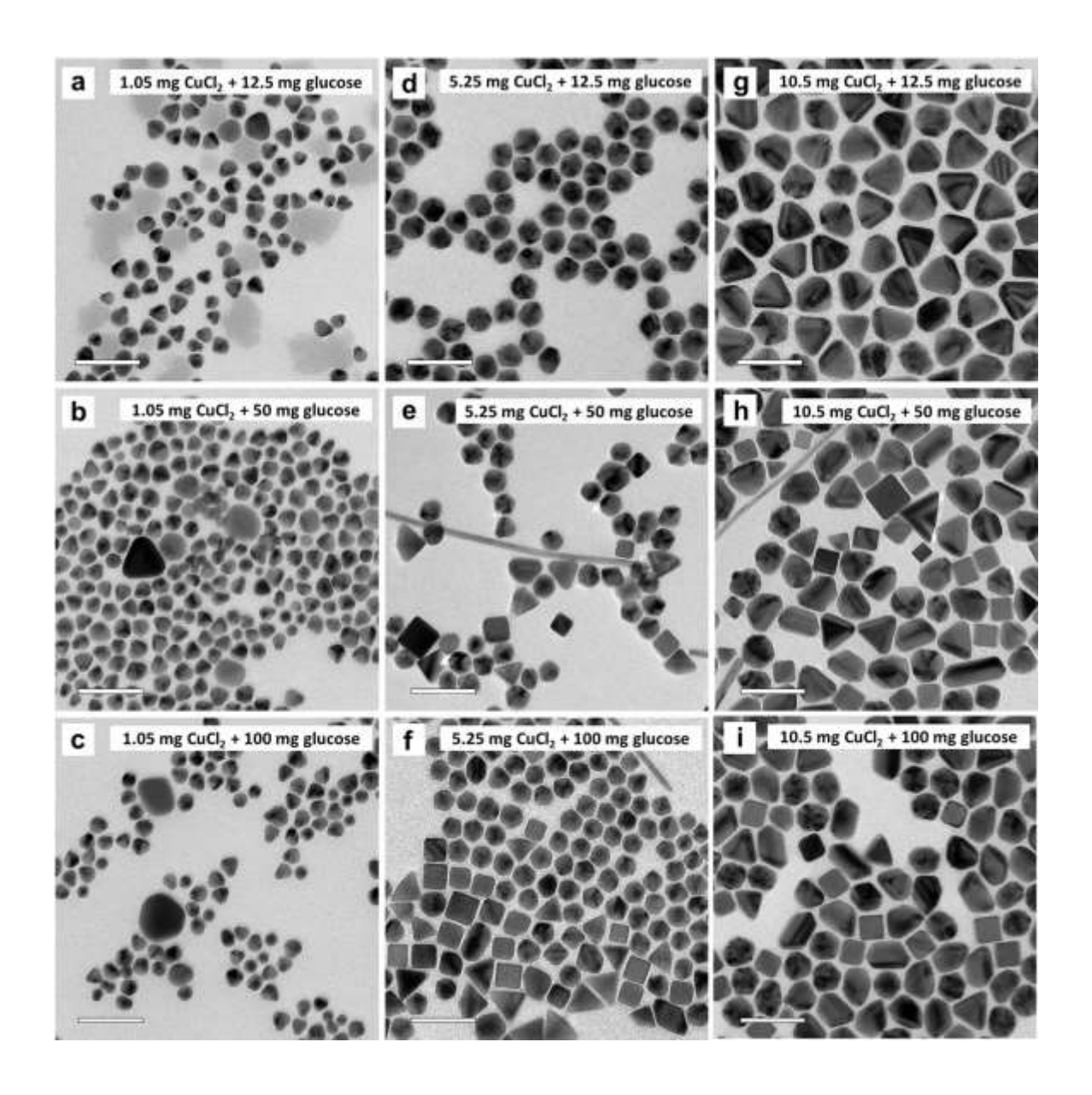


Figure S9. TEM images of the samples in Table S2. The scale bars are 100 nm.

The Role of Chloride. We also investigated the effect of Cl⁻ ions on the shape-controlled synthesis of Pd-Cu Janus nanocrystals. As shown in Figure S10, the Cu atoms were deposited as irregularly-shaped, polycrystalline shells around the Pd seeds when the precursor was switched from CuCl₂ to Cu(ac)₂ (ac: acetate). In this case, the fast reduction of the precursor led to the rapid deposition of Cu atoms onto the entire surface of each Pd seed. When NaCl was added into the reaction solution, however, Pd-Cu nanocrystals with well-defined shapes were obtained again, indicating the important role played by Cl⁻ ions in the formation of Cu nanocrystals. Similar to HDA, Cl⁻ ions can coordinate to Cu(II) ions and thus slow down their reduction rate, ¹² enabling the selective nucleation and growth of Cu from one site on the Pd seed for the generation of a Janus nanocrystal with a well-defined shape. ¹³

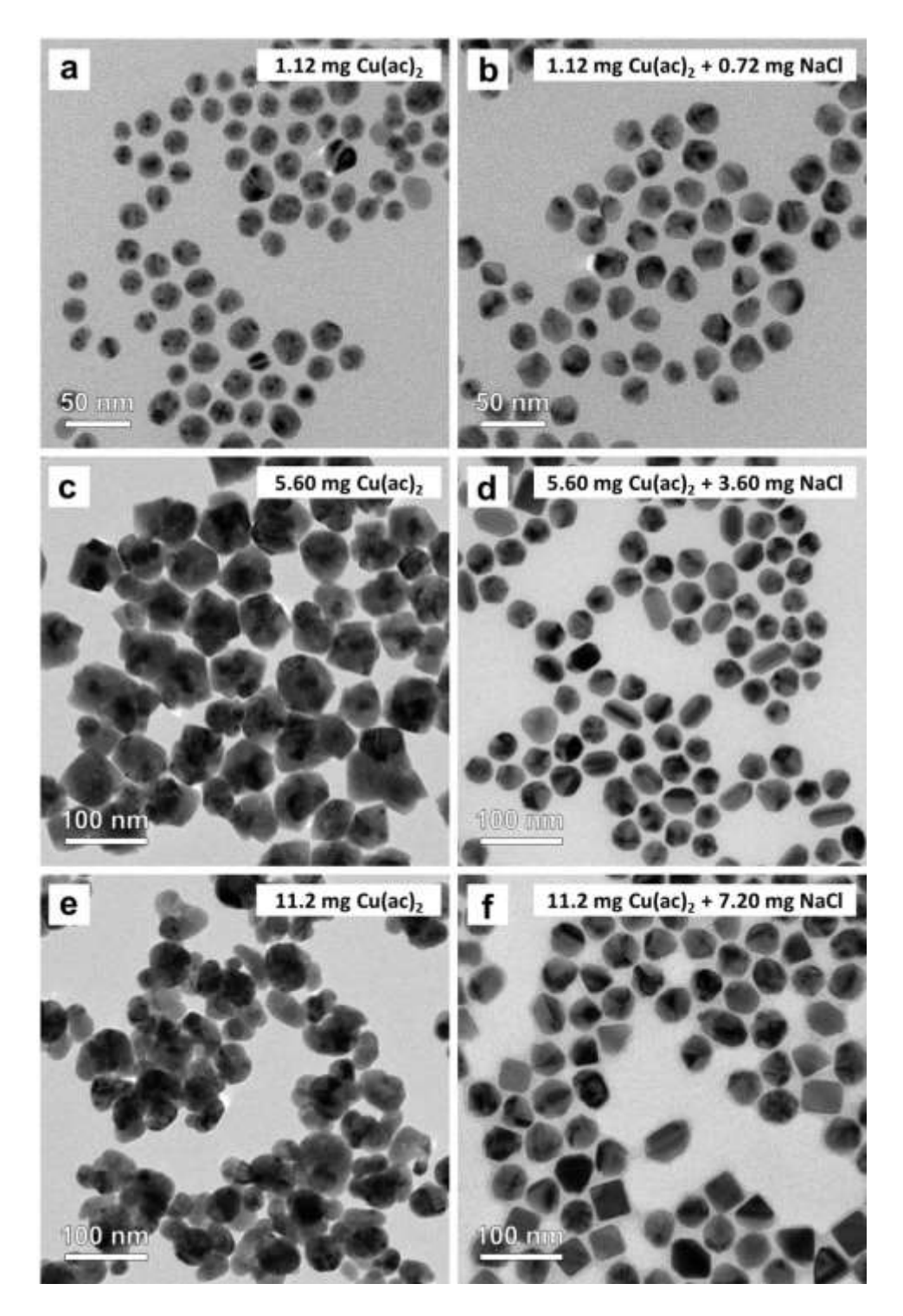


Figure S10. TEM images of the Pd-Cu nanocrystals prepared using the standard protocols for (a, b) pentagonal bipyramids, (c, d) decahedra, and (e, f) truncated bitetrahedra, respectively, except for the use of different Cu precursors: (a, c, e) Cu(ac)₂, and (b, d, f) Cu(ac)₂ plus NaCl.

Control of Size. Although the size of the Pd-Cu nanocrystals could not be tightly controlled by simply varying the amount of the Cu(II) precursor, it could be tuned by altering the amount of the Pd icosahedral seeds. In the case of Pd-Cu decahedra, when the amount of the Pd seeds was increased by 50 and 100%, the size of the as-obtained nanocrystals decreased from 39.3 to 32.7 and 31.7 nm (Figure S11, a and b). When more seeds were used with a fixed amount of the Cu(II) precursor, fewer Cu atoms were deposited on each Pd seed, leading to a smaller size for the decahedra. Similarly, the edge length of the Pd-Cu truncated bitetrahedra decreased from 48.2 to 46.4 and 41.3 nm when the amount of the Pd seeds was increased by 50 and 100% (Figure S11, c and d). It should be mentioned that the purity of the truncated bitetrahedra also slightly dropped, with the inclusion of an increased proportion of polycrystalline particles. Taken together, the size of both decahedra and truncated bitetrahedra could be controlled to a certain extent by varying the amount of the Pd seeds, but the use of a large amount of seeds might compromise the purity of the target products.

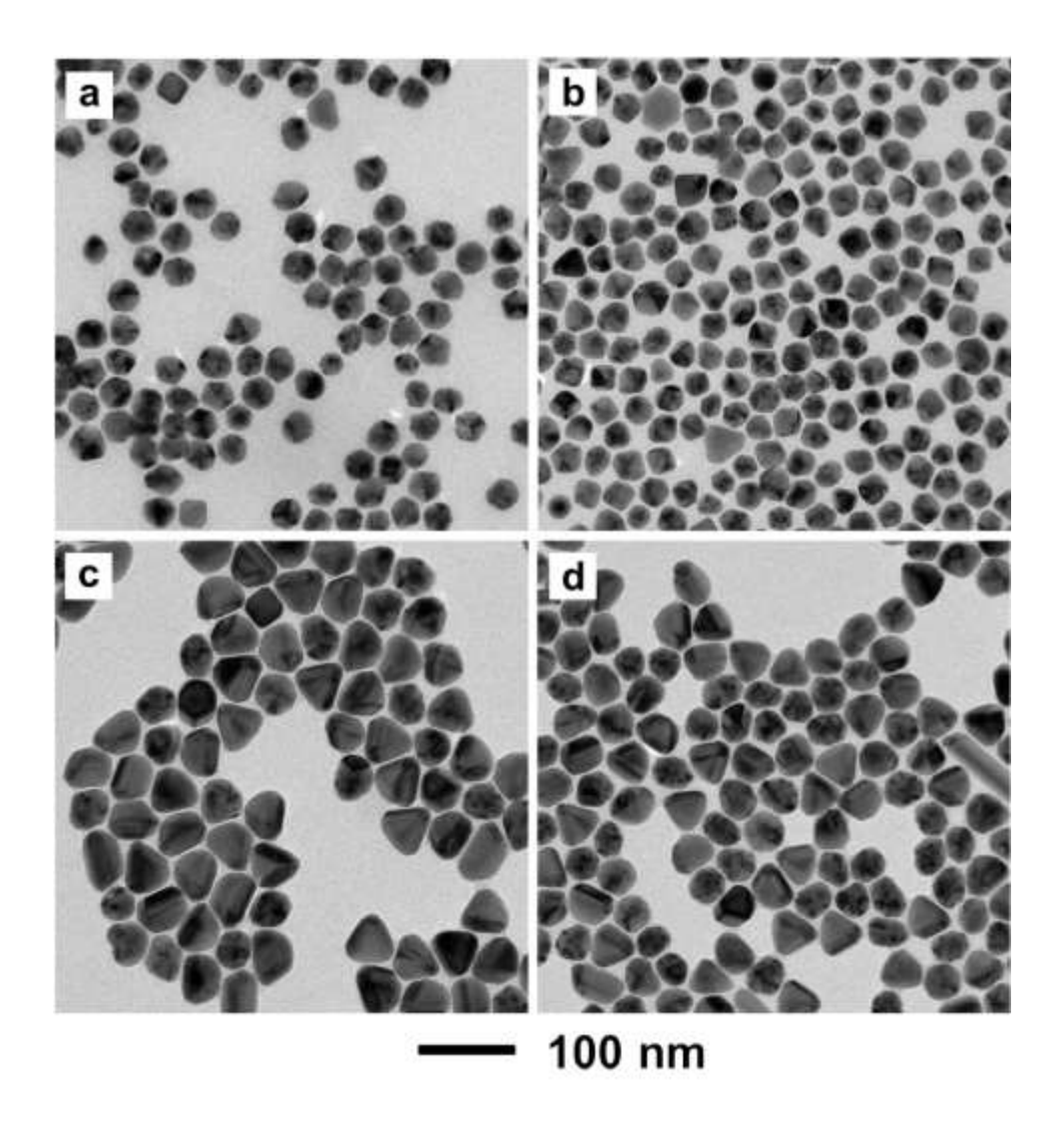


Figure S11. TEM images of (a, b) Pd-Cu decahedra and (c, d) truncated bitetrahedra prepared using the standard protocol, except for the use of the suspension of Pd icosahedral seeds (1.1 mg·mL⁻¹) at different volumes: (a, c) 75 and (b, d) 100 μ L, respectively.

Table S3. Concentrations of Cu and Pd in the inks prepared for the electrochemical tests.

| Samples | Conc. of Cu (mg/mL) | Conc. of Pd (mg/mL) | Ratio of Cu to Pd |
|------------------------|---------------------|---------------------|-------------------|
| pentagonal bipyramids | 0.19 | 0.021 | 15.2 |
| decahedra | 0.23 | 0.0083 | 46.2 |
| truncated bitetrahedra | 0.24 | 0.0048 | 83.7 |

Table S4. Details of the selectivity and geometric current density in CO₂ reduction using the Pd-Cu pentagonal bipyramids as the catalyst.

| E (V vs RHE) | H ₂ (%) | CO (%) | CH ₄ (%) | C ₂ H ₄ (%) | Ethanol (%) | 1-Propanol (%) | Formate (%) | Acetate (%) | Total (%) | jtotal (mA•cm-2) |
|--------------------|--------------------|----------------|---------------------|-----------------------------------|----------------|-------------------|----------------|---------------|----------------|---------------------|
| -0.7 | 29.9 ± 0.3 | 27.8 ± 0.9 | 0 ± 0 | 3.7 ± 0 | 7.9 ± 0.3 | 0 ± 0 | 34.8 ± 0.7 | 0 ± 0 | 104.1 ± 1.0 | -2.1 ± 0.1 |
| -0.8 | 27.2 ± 1.1 | 25.0 ± 2.2 | 0 ± 0 | 5.4 ± 1.2 | 4.4 ± 0.1 | 1.1 ± 2.0 | 34.7 ± 0.2 | 0.6 ± 0.5 | 98.5 ± 1.8 | -5.4 ± 0.2 |
| -0.9 | 27.7 ± 2.4 | 10.0 ± 1.6 | 0.3 ± 0.3 | 17.8 ± 3.9 | 6.6 ± 0.5 | 4.9 ± 0.4 | 26.4 ± 3.7 | 0.7 ± 0.2 | 94.4 ± 5.0 | -14.2 ± 2.5 |
| -1.0 | 28.5 ± 3.9 | 2.0 ± 0.5 | 4.8 ± 2.1 | 31.3 ± 0.9 | 12.6 ± 1.3 | 5.6 ± 0.9 | 10.9 ± 2.4 | 0.9 ± 0.1 | 96.5 ± 0.2 | -34.9 ± 1.4 |

Table S5. Details of the selectivity and geometric current density in CO₂ reduction using the Pd-Cu decahedra as the catalyst.

| E (V vs RHE) | H ₂ (%) | CO (%) | CH ₄ (%) | C ₂ H ₄ (%) | Ethanol (%) | 1-Propanol (%) | Formate (%) | Acetate (%) | Total (%) | jtotal (mA•cm-2) |
|--------------------|--|----------------|---------------------|-----------------------------------|----------------|-------------------|----------------|---------------|--------------------|---------------------|
| -0.7 | 37.7 ± 1.2 | 22.3 ± 0.6 | 0 ± 0 | 5.4 ± 0.1 | 5.8 ± 0 | 0 ± 0 | 29.2 ± 0.1 | 0 ± 0 | $100.4 \\ \pm 0.4$ | -2.7 ± 0 |
| -0.8 | 32.9 ± 0.3 | 15.0 ± 0.5 | 0 ± 0 | 11.4 ± 0.5 | 4.4 ± 0.6 | 2.8 ± 0.2 | 27.1 ± 0.1 | 0.5 ± 0.1 | 94.1 ± 1.4 | -7.0 ± 0 |
| -0.9 | $\begin{array}{c} 27.4 \pm \\ 0.2 \end{array}$ | 4.5 ± 0.2 | 0.8 ± 0 | 27.1 ± 0.8 | 7.8 ± 1.2 | 6.2 ± 0.6 | 20.3 ± 1.4 | 0.6 ± 0 | 94.8 ± 4.0 | -16.7 ± 1.0 |
| -1.0 | 25.9 ± 2.5 | 1.4 ± 0.1 | 6.2 ± 1.0 | 34.0 ± 0.5 | 11.6 ± 0.3 | 4.8 ± 0.4 | 9.4 ± 1.0 | 0.6 ± 0.1 | 95 ± 1.2 | -30.1 ± 2.3 |

Table S6. Details of the selectivity and geometric current density in CO₂ reduction using the Pd-Cu truncated bitetrahedra as the catalyst.

| E (V vs RHE) | H ₂ (%) | CO (%) | CH ₄ (%) | C ₂ H ₄ (%) | Ethanol (%) | 1-Propanol (%) | Formate (%) | Acetate (%) | Total (%) | jtotal (mA•cm ⁻²) |
|--------------------|--|----------------|---------------------|-----------------------------------|---------------|-------------------|---------------|---------------|----------------|----------------------------------|
| -0.7 | 30.4 ± 5.5 | 22.6 ± 1.5 | 0 ± 0 | 4.1 ± 0.5 | 5.4 ± 2.5 | 0 ± 0 | 30.8 ± 1.8 | 0 ± 0 | 93.2 ± 11.8 | -2.3 ± 0 |
| -0.8 | 30.3 ± 0.2 | 17.6 ± 0.4 | 0 ± 0 | 10.1 ± 0.7 | 5.3 ± 0.4 | 3.5 ± 0.2 | 31.1 ± 1.4 | 0 ± 0 | 98.0 ± 0.7 | -5.9 ± 0.4 |
| -0.9 | $\begin{array}{c} 29.8 \pm \\ 0.8 \end{array}$ | 7.2 ± 0.2 | 1.5 ± 0.1 | 20.2 ± 0 | 7.8 ± 1.6 | 4.9 ± 0.1 | 22.0 ± 1.3 | 0.5 ± 0.1 | 93.9 ± 1.7 | -16.9 ± 1.2 |
| -1.0 | 35.7 ± 1.5 | 1.5 ± 0.2 | 10.2 ± 2.2 | $25.4 \pm \\1.4$ | 9.1 ± 0.6 | 3.6 ± 0.2 | 8.8 ± 0.1 | 0.4 ± 0.1 | 94.8 ± 3.3 | -40.4 ± 4.1 |

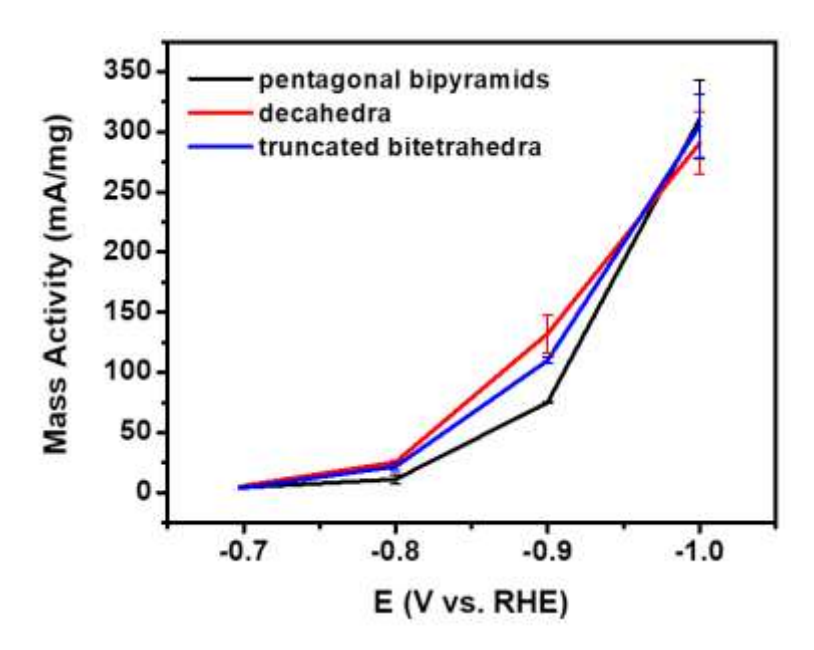


Figure S12. Mass activities toward C_{2+} products when different types of the Pd-Cu nanocrystals were used as catalysts. The results are based on the overall mass of Pd and Cu.

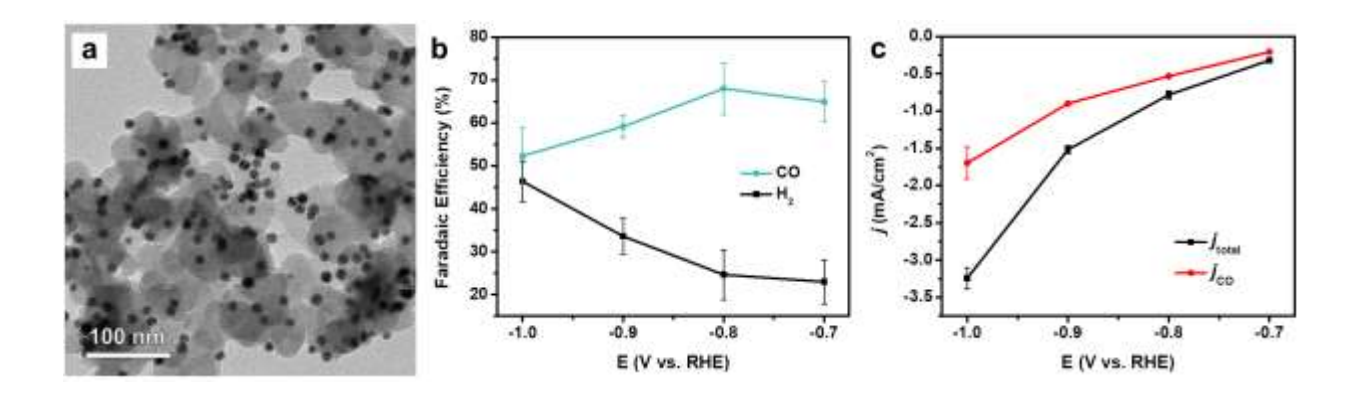


Figure S13. (a) TEM image of the Pd icosahedra supported on carbon. (b) FEs toward CO and H₂ and (c) geometric current density of the Pd icosahedra under different potentials in a 0.5 M KHCO₃ electrolyte.

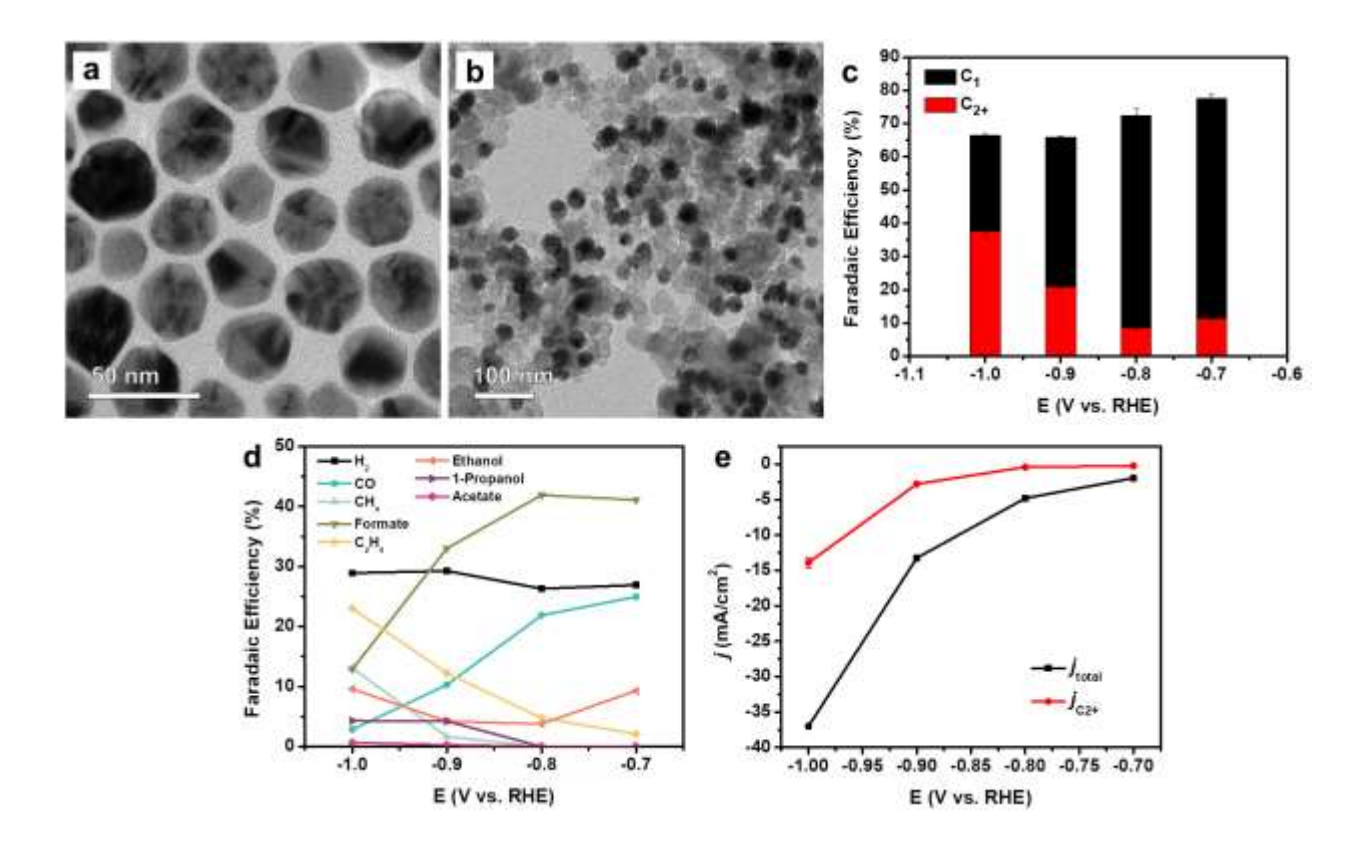


Figure S14. (a, b) TEM image of Cu twinned nanoparticles: (a) before, and (b) after deposition on carbon. (c, d) FEs and (e) geometric current density of the Cu twinned nanoparticles under different potentials in a 0.5 M KHCO₃ electrolyte.

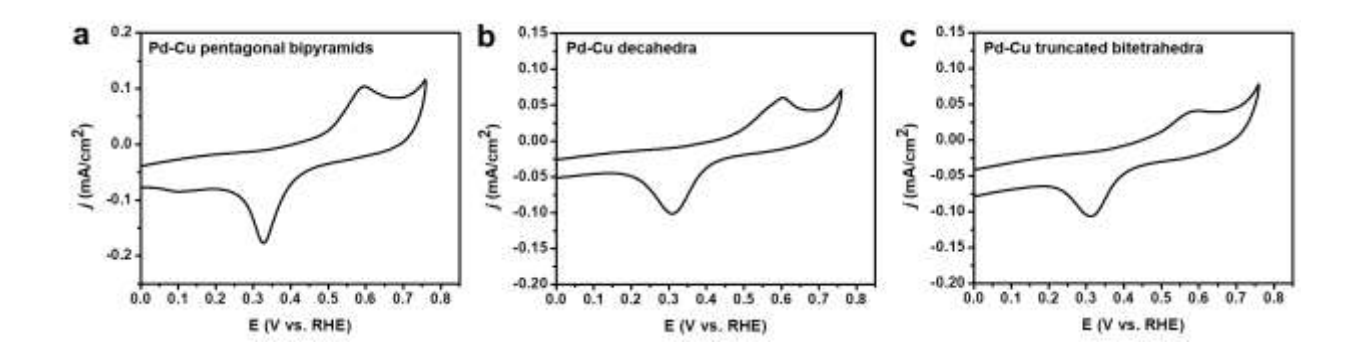


Figure S15. CVs recorded for the Pd-Cu Janus nanocrystals at 25 mV/s in 0.1 M KOH: (a) pentagonal bipyramids, (b) decahedra, and (c) truncated bitetrahedra, respectively.

Table S7. ECSAs and ECSA-normalized current densities at $-1.0 \text{ V}_{\text{RHE}}$ of the three different types of Pd-Cu Janus nanocrystals.

| Sample | ECSA (cm ²) | Mass-normalized ECSA (cm ² /mg) ^a | ECSA-normalized C ₂₊ current density (mA•cm ⁻²) |
|------------------------------|-------------------------|--|--|
| Pd-Cu pentagonal bipyramids | 0.42 | 10.5 | 32.8 |
| Pd-Cu decahedra | 0.29 | 7.25 | 41.5 |
| Pd-Cu truncated bitetrahedra | 0.16 | 4.0 | 76.4 |

^a The ECSAs were normalized to the mass of Cu.

Table S8. The selectivity and geometric current density in CO_2 reduction when 20 μg of the Pd-Cu pentagonal bipyramids were used as the catalyst.

| E (V vs RHE) | H ₂ (%) | CO (%) | CH ₄ (%) | C ₂ H ₄ (%) | Formate (%) | Acetate (%) | Ethanol (%) | 1-Propanol (%) | Total (%) | j (mA•cm ⁻ ²) |
|--------------------|--------------------|-----------|------------------------|-----------------------------------|-------------|-------------|-------------|-------------------|--------------|--------------------------------------|
| -0.9 | 26.9 | 12.7 | 0.8 | 17.8 | 27.2 | 0.5 | 5.2 | 4.5 | 95.6 | -9.4 |
| -1.0 | 23.0 | 3.3 | 8.7 | 30.1 | 13.3 | 1.0 | 11.2 | 4.5 | 95.0 | -20.0 |

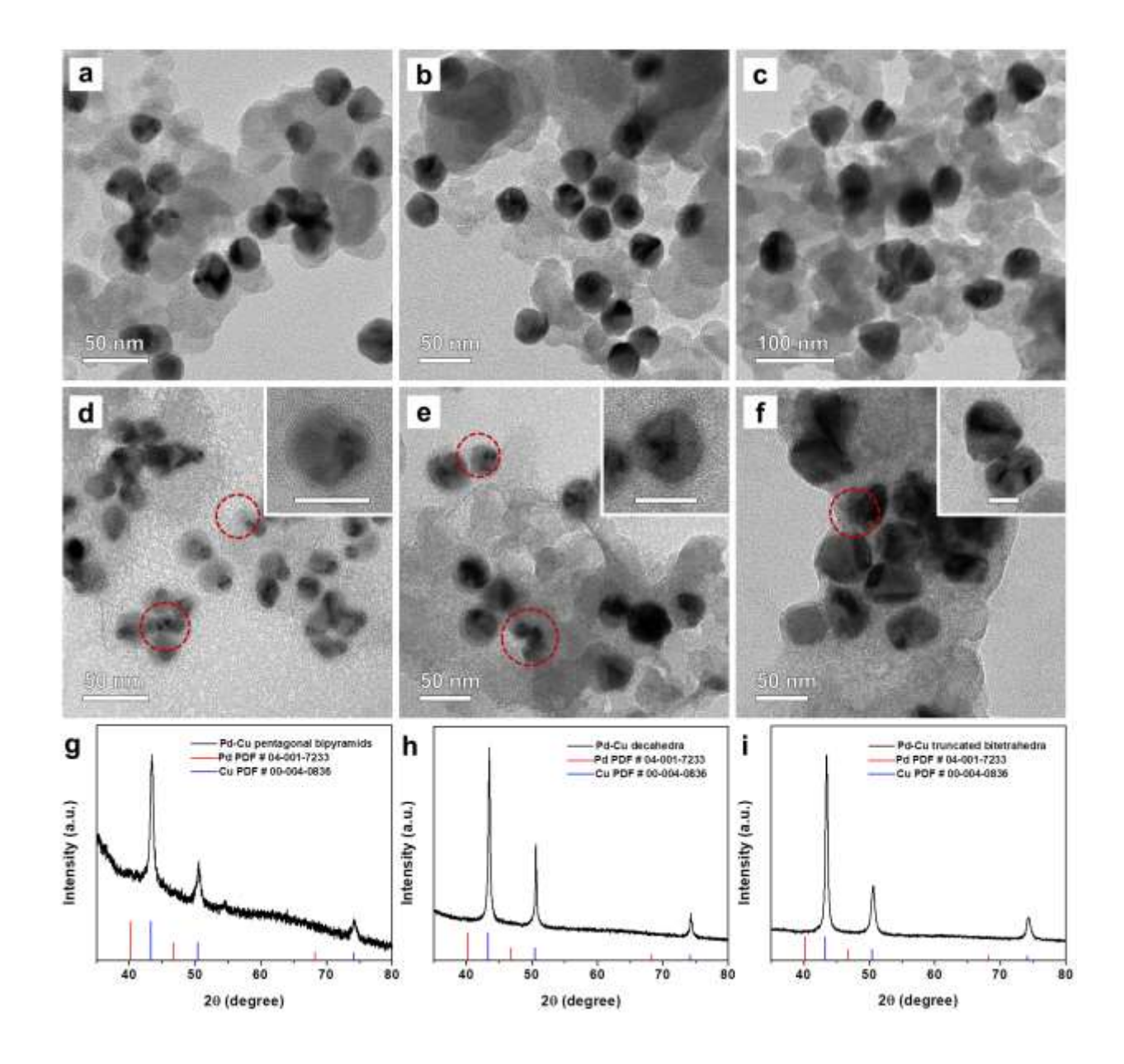


Figure S16. (a–c) TEM images of the Pd-Cu nanocrystals supported on carbon before electrolysis: (a) pentagonal bipyramids, (b) decahedra, and (c) truncated bitetrahedra. (d–f) TEM images and (g–i) XRD patterns of the Pd-Cu nanocrystals after 1 h of electrolysis at -1.0 V_{RHE}: (d, g) pentagonal bipyramids, (e, h) decahedra, and (f, i) truncated bitetrahedra. The scale bars in the insets of (d–f) are 30 nm. The places where dissolution of Cu or formation of small Cu nanoparticles occurred are marked by red circles.

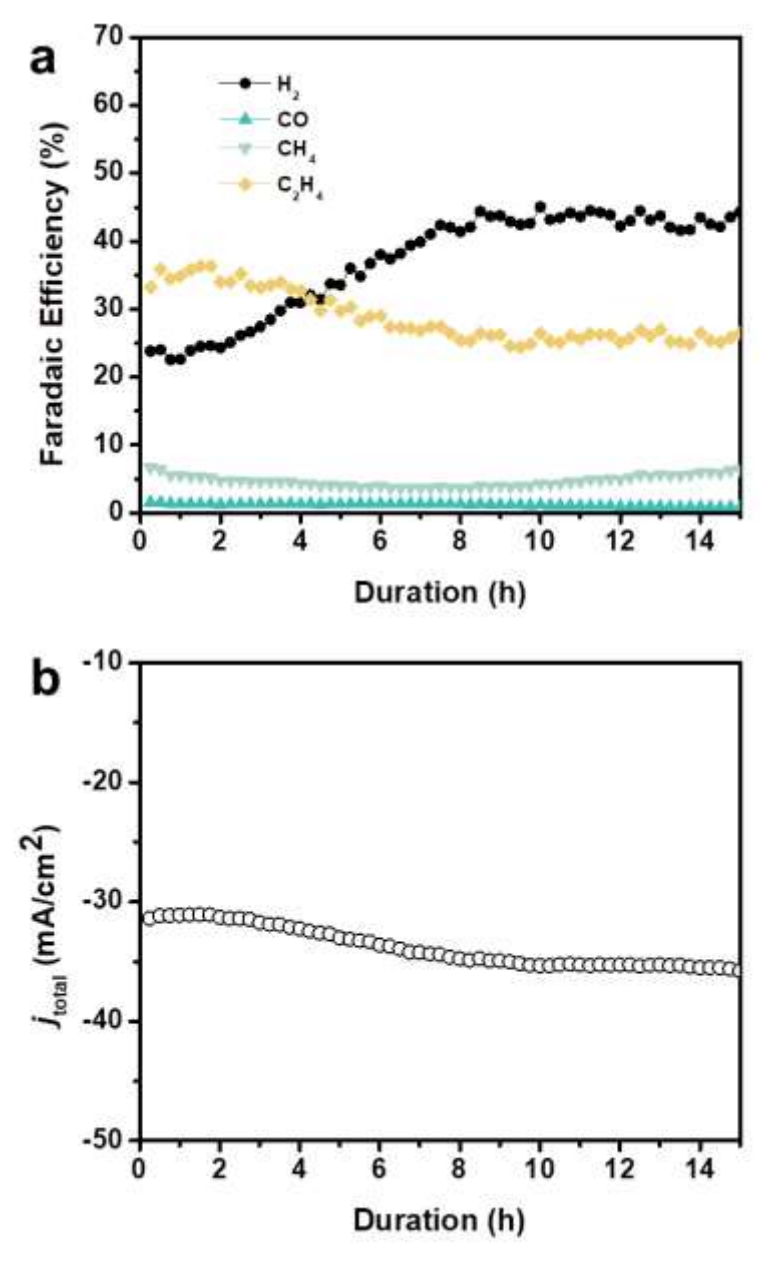


Figure S17. Stability test of the Pd-Cu decahedra at -1.0 V_{RHE} for 15 h: (a) FEs of gaseous products and (b) current density normalized to the geometric area.

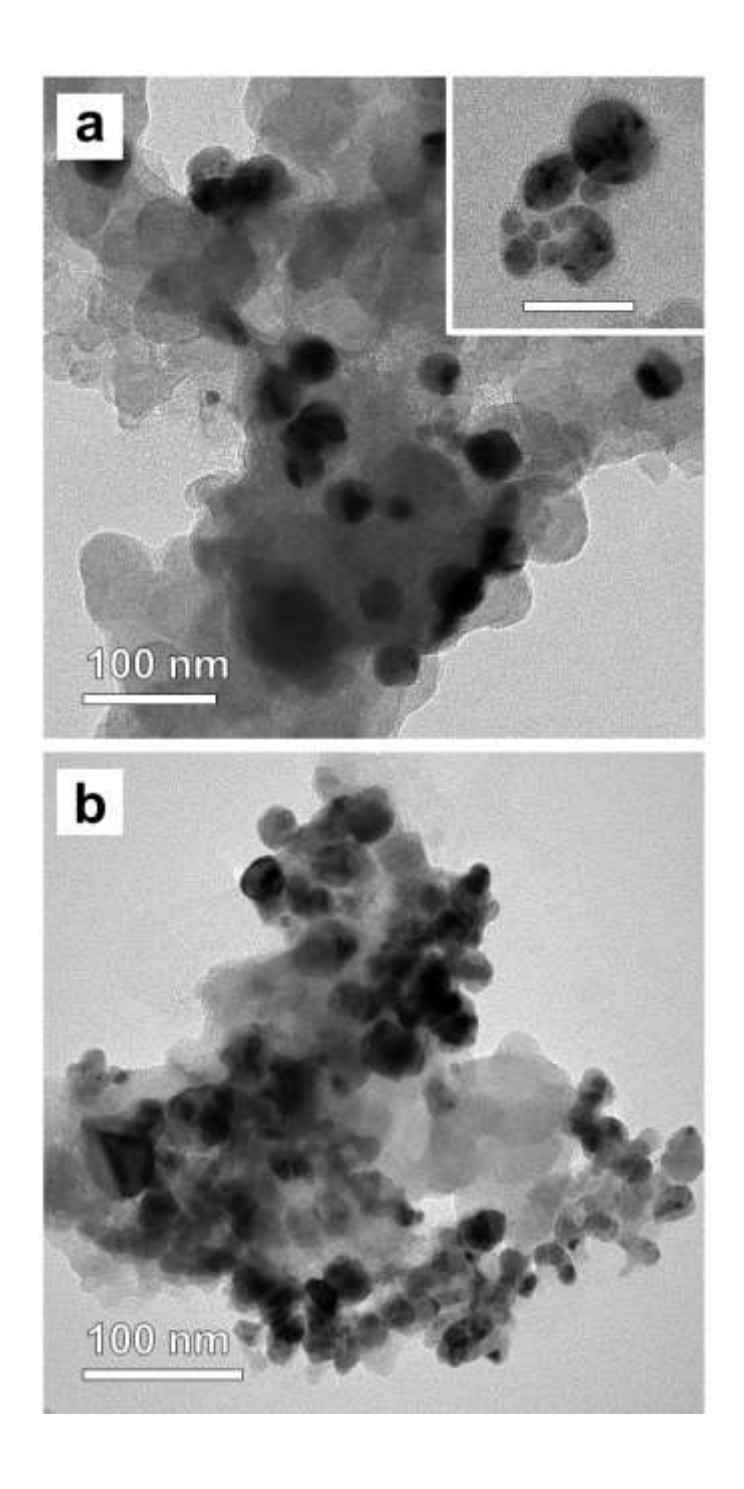


Figure S18. TEM images of the Pd-Cu decahedra after (a) 3 and (b) 5 h of electrolysis at -1.0 V_{RHE}, respectively. The scale bar in the inset of (a) is 50 nm.

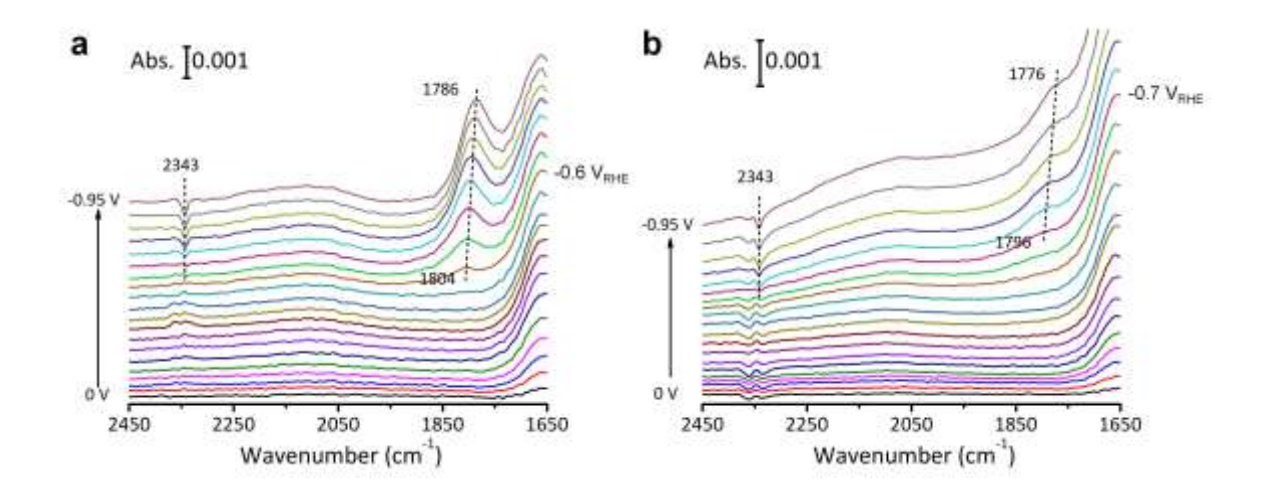


Figure S19. Real-time ATR-IR spectra recorded at potentials varying from 0 to -0.95 V_{RHE} on the (a) Pd-Cu decahedra and (b) Cu twinned nanoparticles in the CO₂-saturated 0.5 M KHCO₃ solution. The peak at 2343 cm⁻¹ can be assigned to the CO₂ in the aqueous solution, and the band located at around 1800 cm⁻¹ can be assigned to the bridge- or multiple-adsorbed *CO on Cu surface.

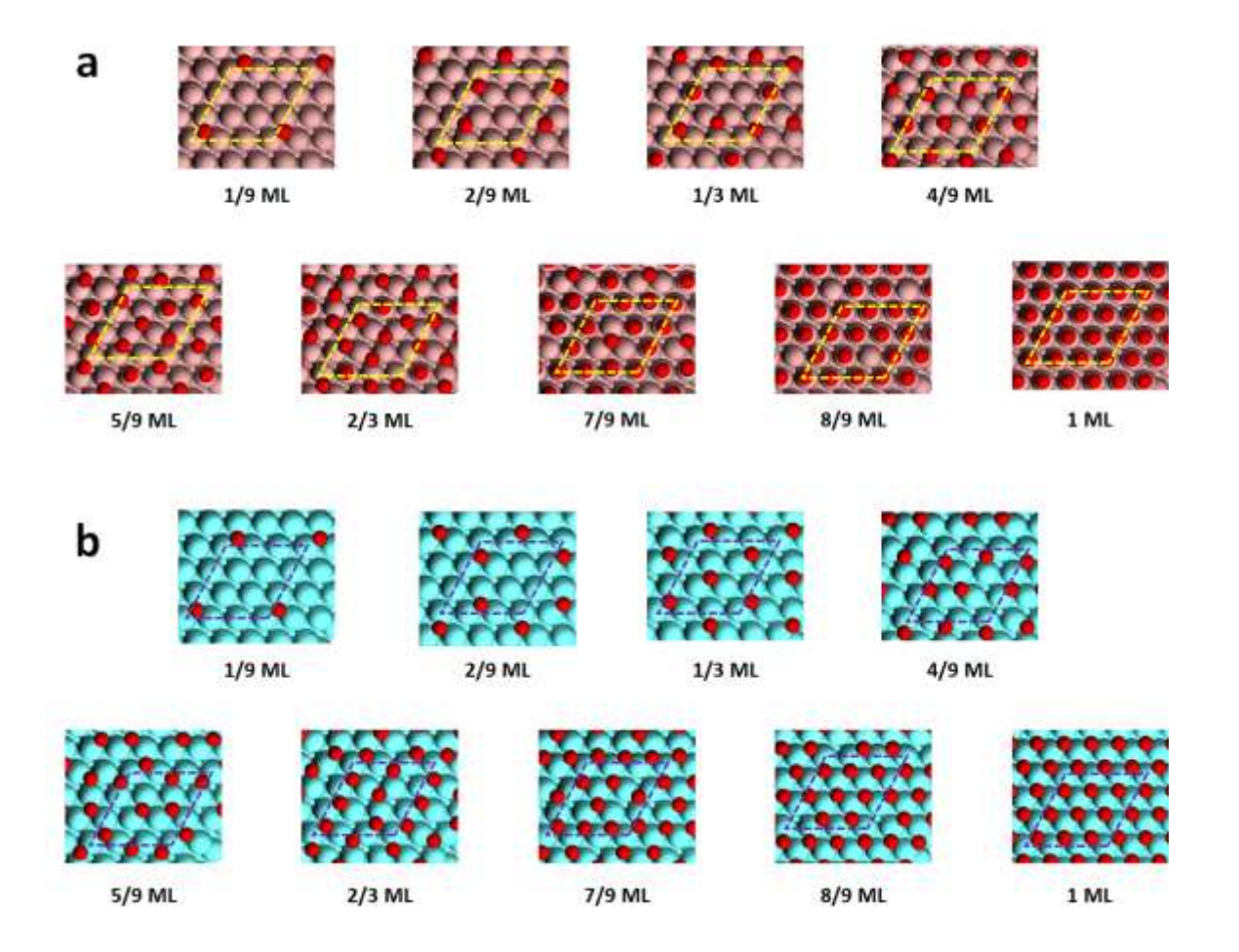


Figure S20. Minimum energy adsorption structures for CO adsorption on (a) Cu(111) and (b) Pd(111) at 1/9 ML to 1 ML CO coverage. Color code: pink – Cu; cyan – Pd; black – C; red – O. Dashed lines denote the (3×3) surface unit cell.

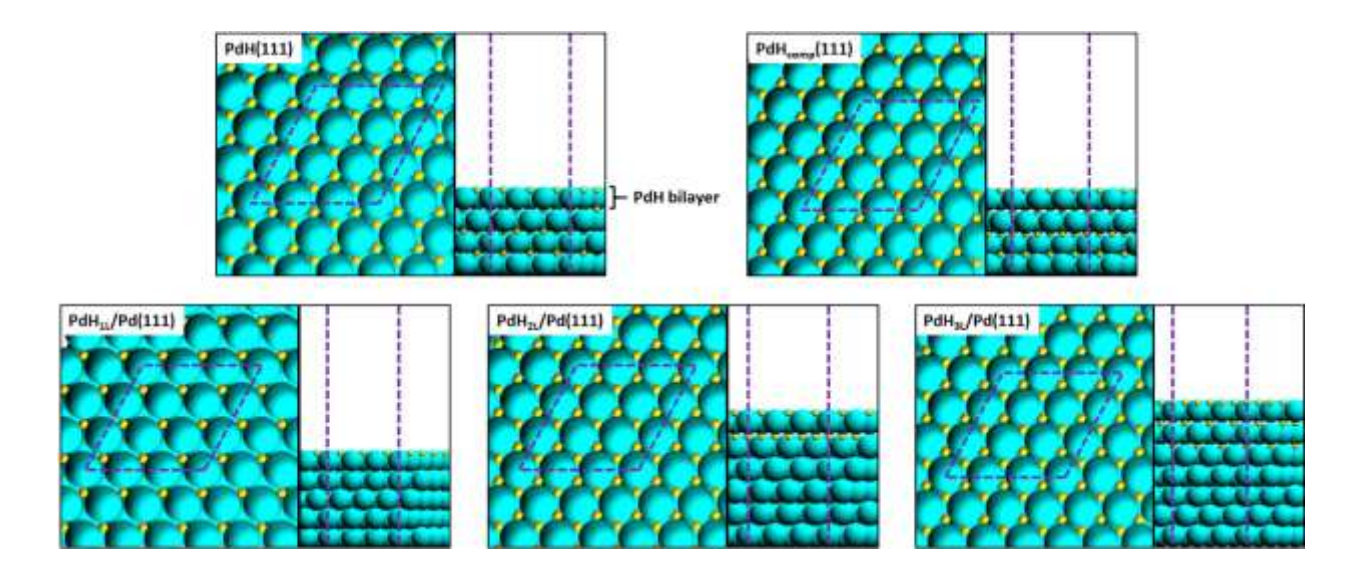


Figure S21. Top and cross-sectional views, side by side in each pair of images, for the minimum energy structures involving clean PdH(111), PdH_{comp}(111), PdH_{1L}/Pd(111), PdH_{2L}/Pd(111), and PdH_{3L}/Pd(111) slabs. The structure of a PdH bilayer is indicated in the cross-sectional view for PdH(111). Color code: cyan – Pd; yellow – H. Dashed lines denote the (3×3) surface unit cell.

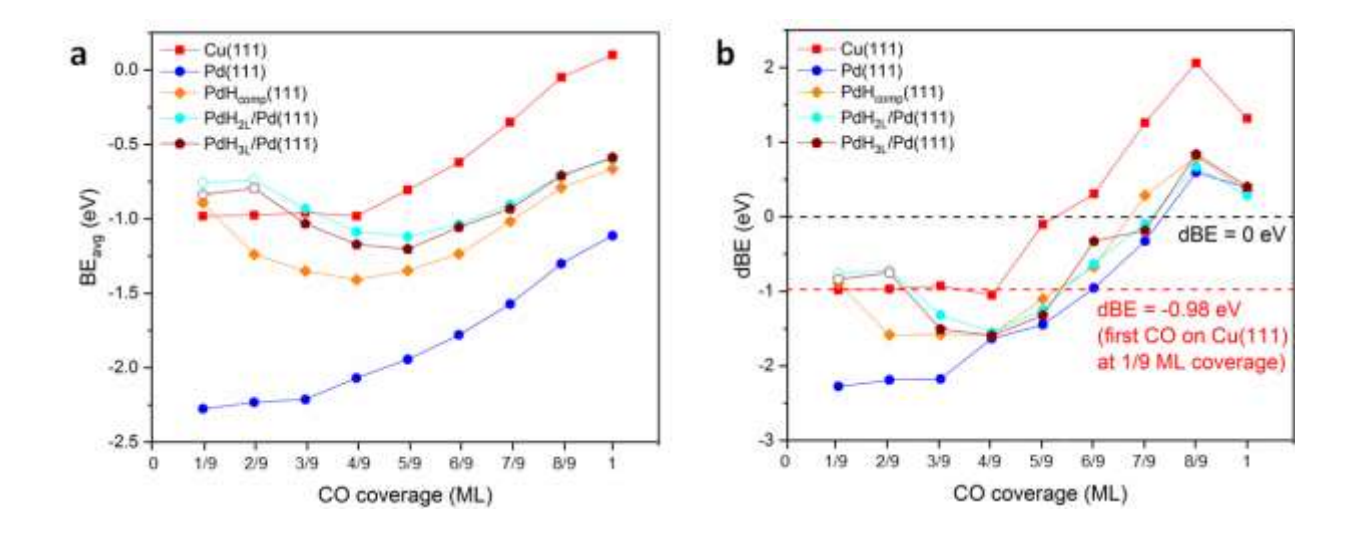


Figure S22. Calculated (a) average and (b) differential binding energies of CO on Cu(111) (red), Pd(111) (blue), PdH_{comp}(111) (orange), PdH_{2L}/Pd(111) (cyan), and PdH_{3L}/Pd(111) (wine) as a function of CO coverage. Black dashed line in (b) indicates a dBE value of 0 eV (thermal-neutral adsorption). Red dashed line in (b) indicates a dBE value of -0.98 eV (BE of CO on a clean Cu(111) surface at 1/9 ML coverage). For PdH_{comp}(111), PdH_{2L}/Pd(111), and PdH_{3L}/Pd(111), open symbol indicates that H termination is preferred; solid symbol indicates that Pd termination is preferred.

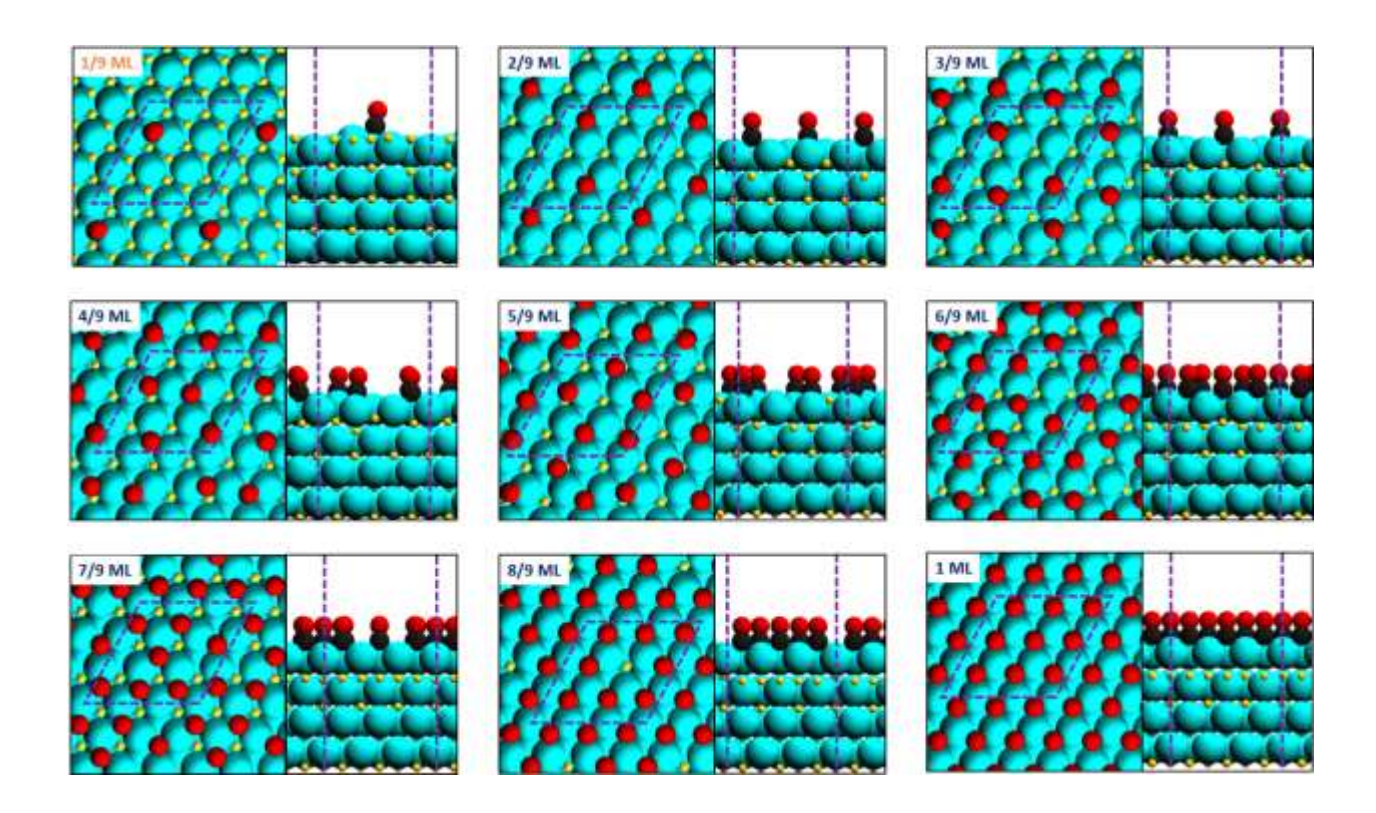


Figure S23. Minimum energy adsorption structures for CO adsorption on PdH(111) at 1/9 ML to 1 ML CO coverage, with top and side views being shown side by side in each pair of images. Color code: cyan – Pd; yellow – H; black – C; red – O. Dashed lines denote the (3×3) surface unit cell. On the top right corner of each image, orange label indicates that H termination is preferred; blue label indicates that Pd termination is preferred.

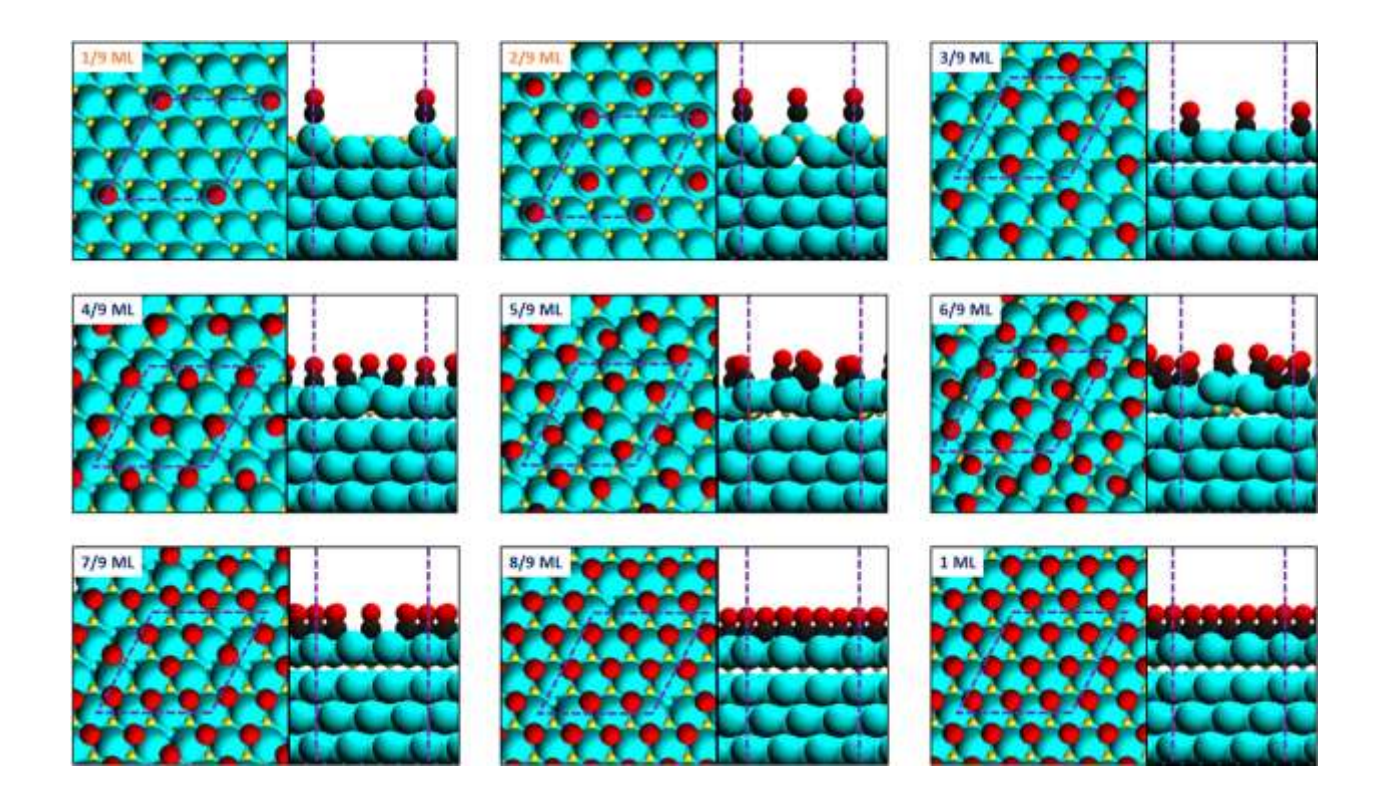


Figure S24. Minimum energy adsorption structures for CO adsorption on $PdH_{1L}/Pd(111)$ at 1/9 ML to 1 ML CO coverage, with top and side views being shown side by side in each pair of images. Color code: cyan – Pd; yellow – H; black – C; red – O. Dashed lines denote the (3 × 3) surface unit cell. On the top right corner of each image, orange label indicates that H termination is preferred; blue label indicates that Pd termination is preferred.

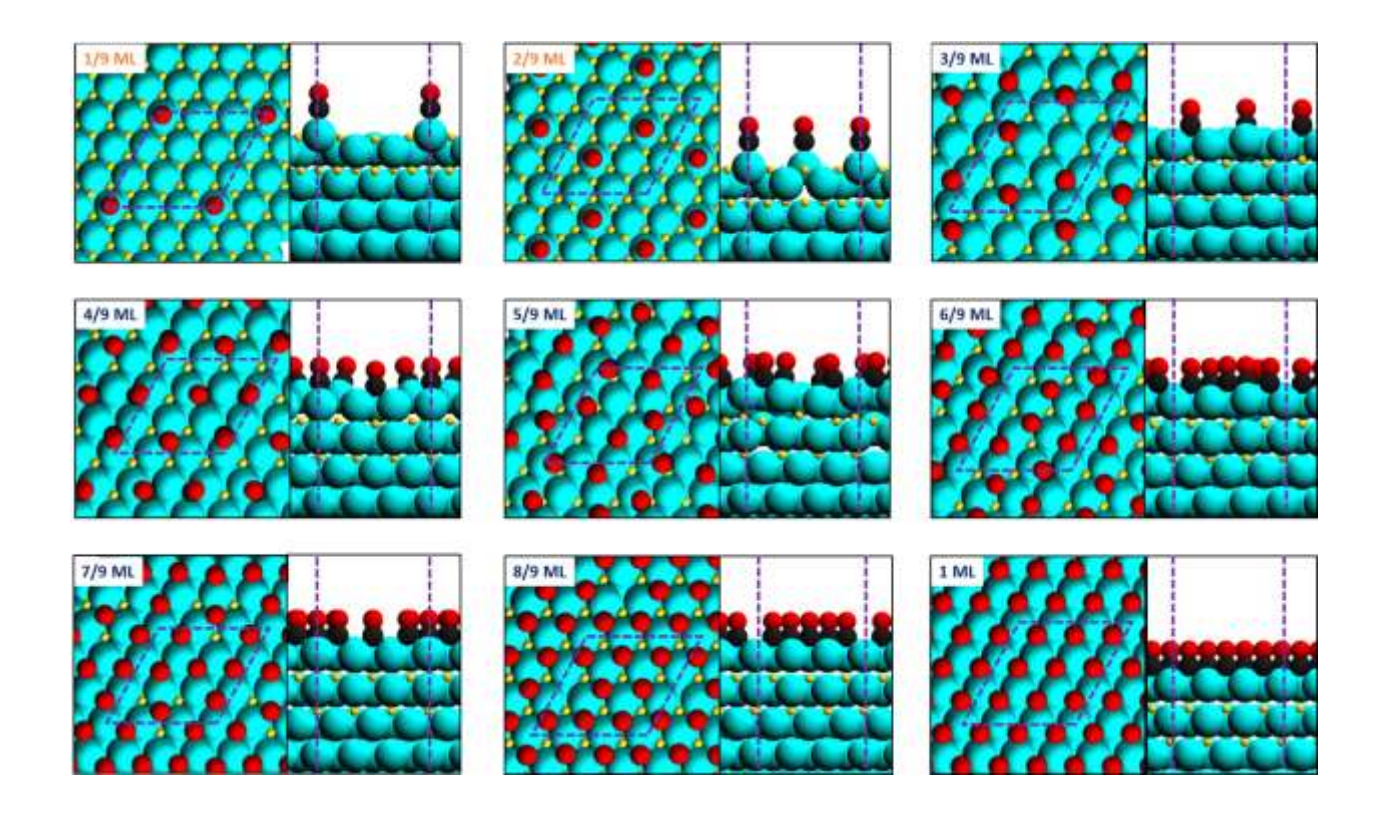


Figure S25. Minimum energy adsorption structures for CO adsorption on $PdH_{2L}/Pd(111)$ at 1/9 ML to 1 ML CO coverage, with top and side views being shown side by side in each pair of images. Color code: cyan – Pd; yellow – H; black – C; red – O. Dashed lines denote the (3×3) surface unit cell. On the top right corner of each image, orange label indicates that H termination is preferred; blue label indicates that Pd termination is preferred.

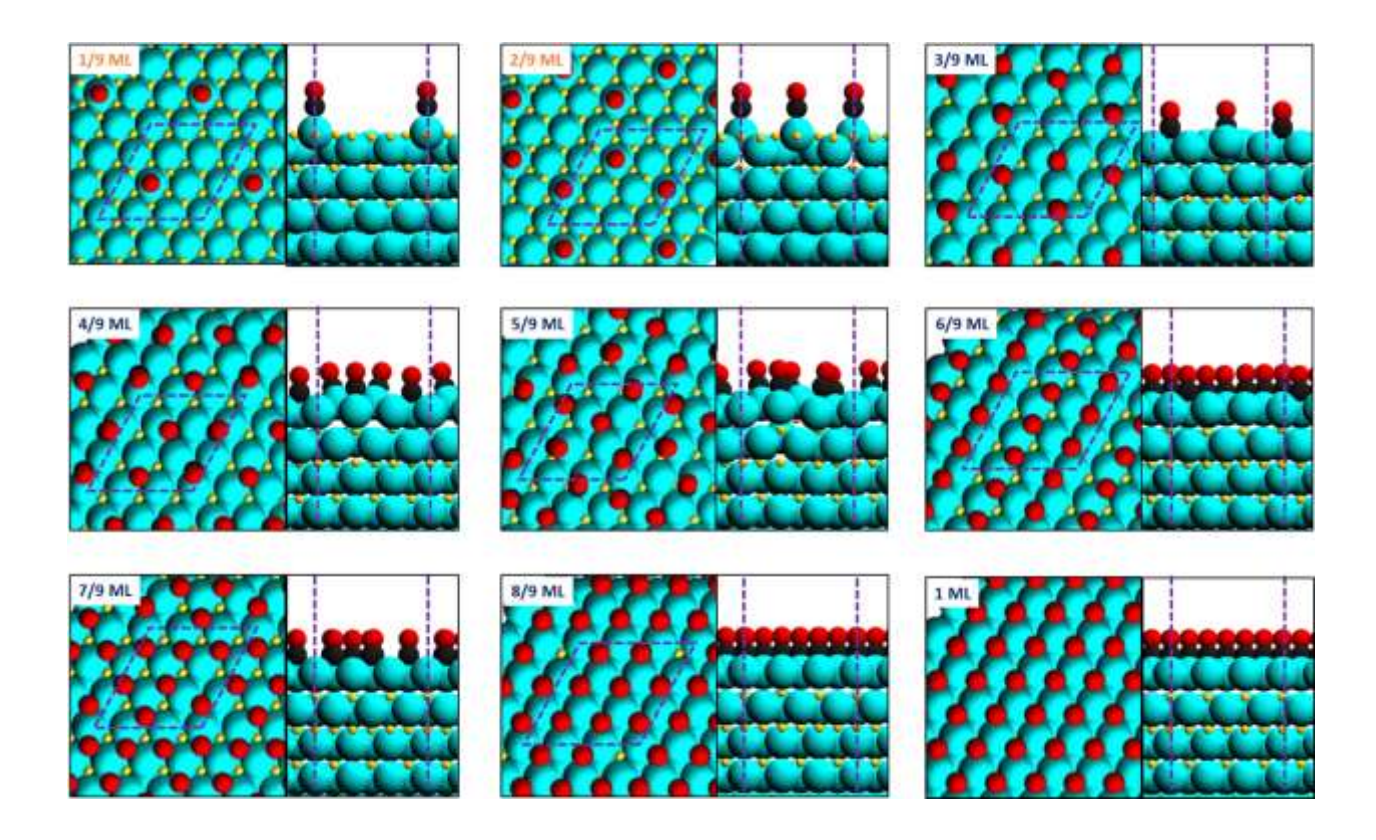


Figure S26. Minimum energy adsorption structures for CO adsorption on $PdH_{3L}/Pd(111)$ at 1/9 ML to 1 ML CO coverage, with top and side views being shown side by side in each pair of images. Color code: cyan – Pd; yellow – H; black – C; red – O. Dashed lines denote the (3 × 3) surface unit cell. On the top right corner of each image, orange label indicates that H termination is preferred; blue label indicates that Pd termination is preferred.

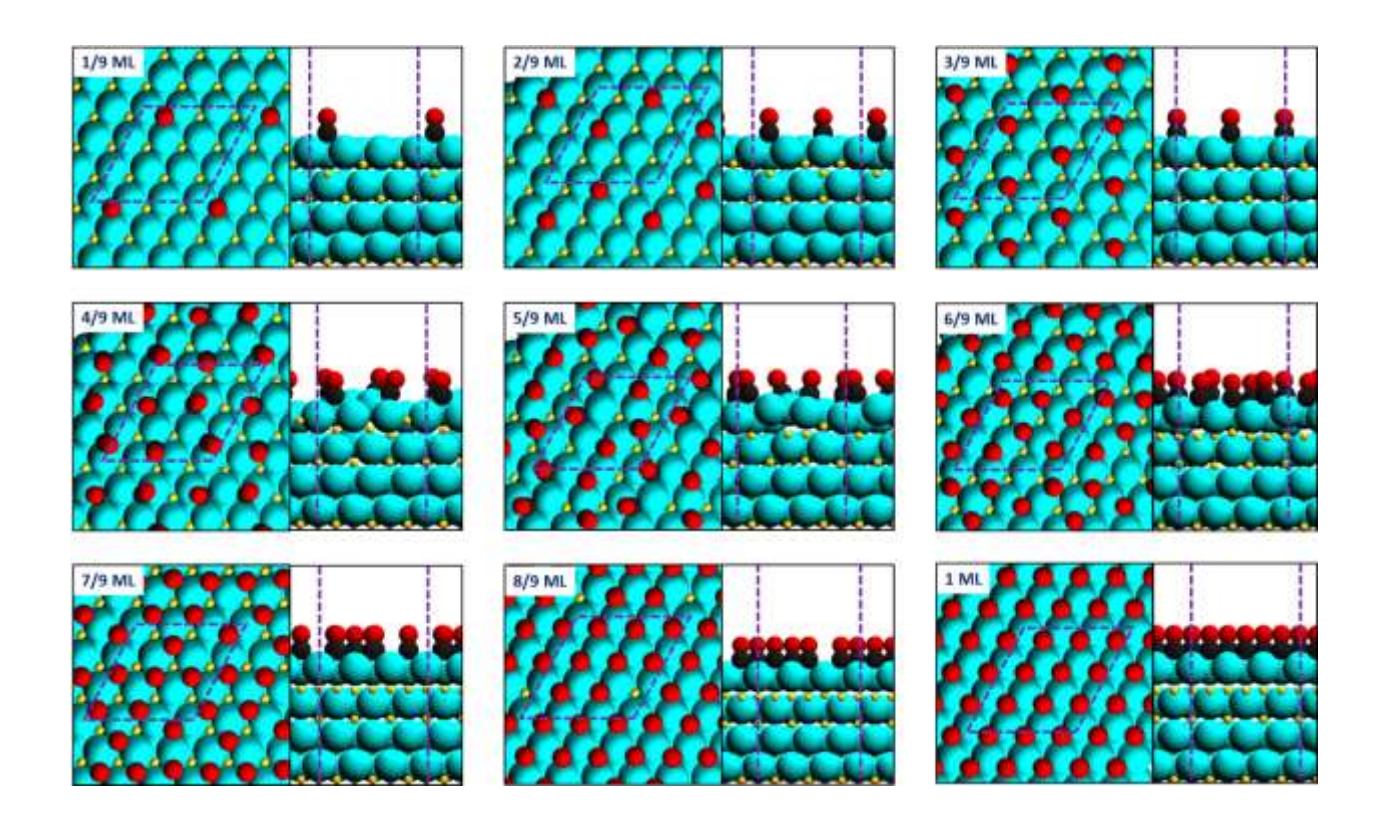


Figure S27. Minimum energy adsorption structures for CO adsorption on $PdH_{comp}(111)$ at 1/9 ML to 1 ML CO coverage, with top and side views being shown side by side in each pair of images. Color code: cyan – Pd; yellow – H; black – C; red – O. Dashed lines denote the (3×3) surface unit cell. On the top right corner of each image, orange label indicates that H termination is preferred; blue label indicates that Pd termination is preferred.

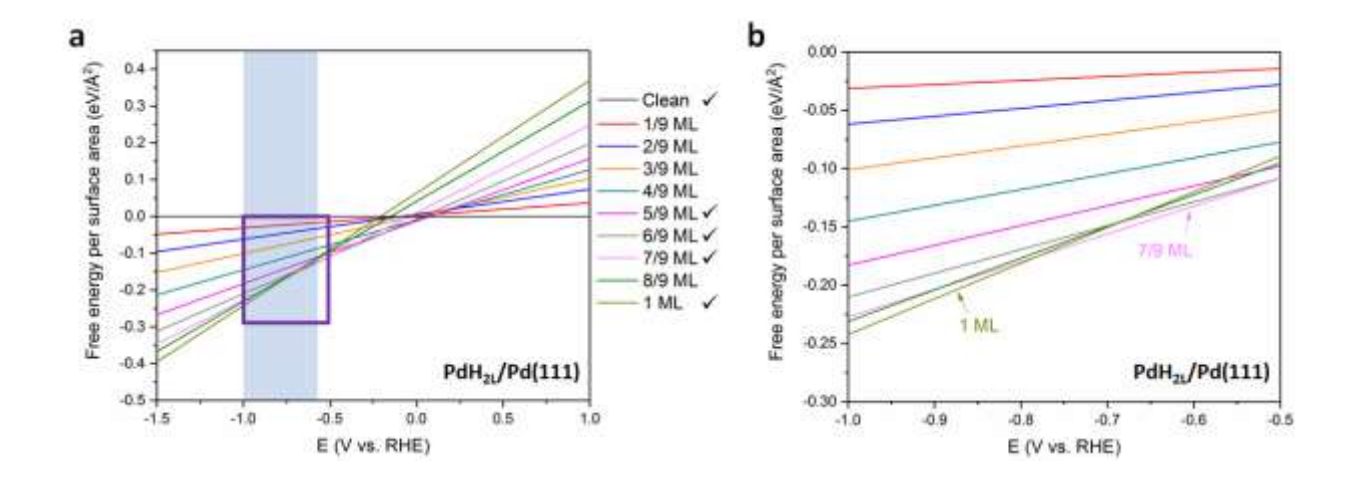


Figure S28. Calculated Pourbaix phase diagram for CO on $PdH_{2L}/Pd(111)$ at room temperature under the electrochemical conditions for CO_2 reduction. The free energy per surface area for each CO coverage up to 1 ML is plotted as a function of the applied potential. At each potential, the most stable surface coverage is the one with the lowest free energy value. In the legend, those coverages marked with tick marks appear as the most stable phases under certain potentials; the remaining phases are not expected to be observable. The range of applied potential evaluated experimentally in this work (-0.7 to -1.0 V_{RHE}) is denoted by the shaded area on (a). An enlarged view of the boxed area in (a) is shown in (b).

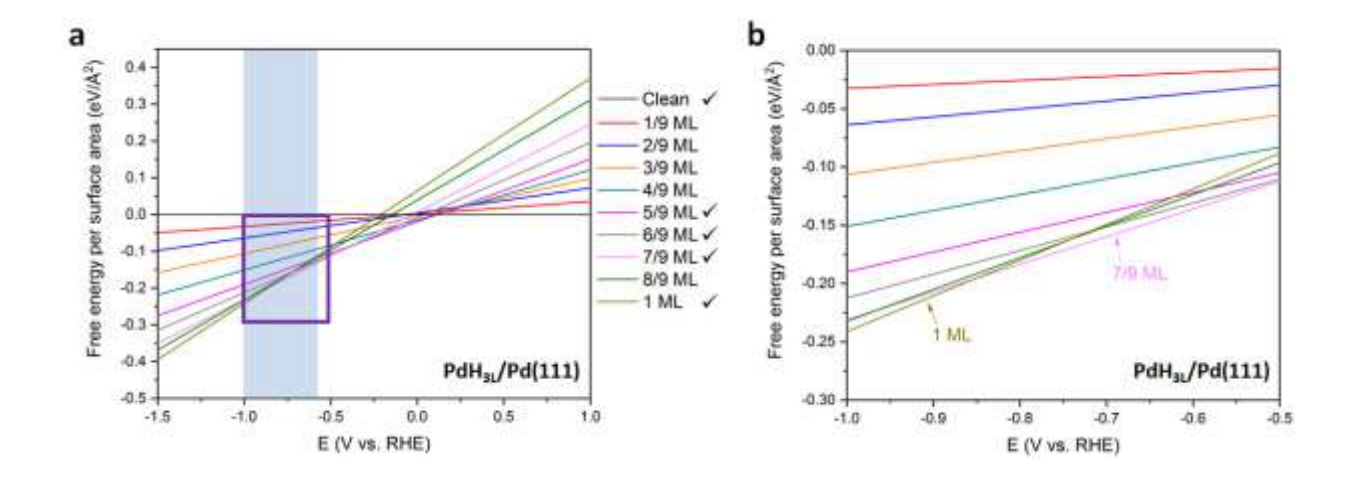


Figure S29. Calculated Pourbaix phase diagram for CO on $PdH_{3L}/Pd(111)$ at room temperature under the electrochemical conditions for CO_2 reduction. The free energy per surface area for each CO coverage up to 1 ML is plotted as a function of the applied potential. At each potential, the most stable surface coverage is the one with the lowest free energy value. In the legend, those coverages marked with tick marks appear as the most stable phases under certain potentials; the remaining phases are not expected to be observable. The range of applied potential evaluated experimentally in this work (-0.7 to -1.0 V_{RHE}) is denoted by the shaded area on (a). An enlarged view of the boxed area in (a) is shown in (b).

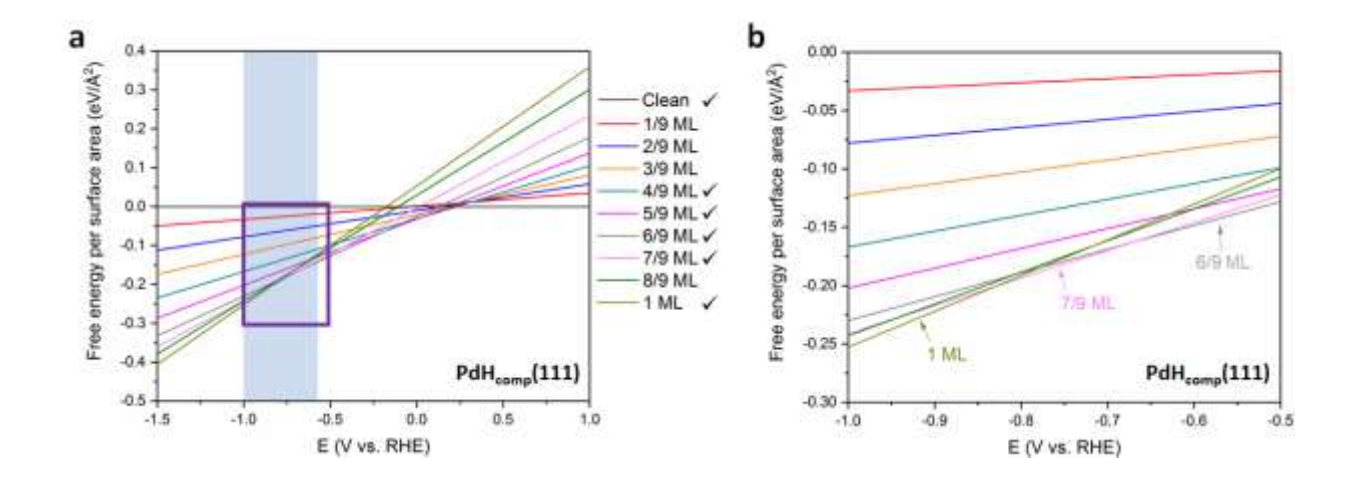


Figure S30. Calculated Pourbaix phase diagram for CO on $PdH_{comp}(111)$ at room temperature under the electrochemical conditions for CO_2 reduction. The free energy per surface area for each CO coverage up to 1 ML is plotted as a function of the applied potential. At each potential, the most stable surface coverage is the one with the lowest free energy value. In the legend, those coverages marked with tick marks appear as the most stable phases under certain potentials; the remaining phases are not expected to be observable. The range of applied potential evaluated experimentally in this work (-0.7 to -1.0 V_{RHE}) is denoted by the shaded area on (a). An enlarged view of the boxed area in (a) is shown in (b).

Density Functional Theory (DFT) Calculations. Periodic DFT calculations were performed using the Vienna ab initio simulation package (VASP) code. 14,15 The exchange-correlation functional was described by the generalized gradient approximation (GGA-PBE), 16 and the electron-ion interactions were described using the projector augmented-wave (PAW) potentials. ^{17,18} The D3 method developed by Grimme et al. was adopted to account for dispersive interactions. 19 The Kohn-Sham electron wave functions were expanded in plane-wave basis sets with a kinetic-energy cutoff of 400 eV. During each calculation on a metal surface, the bottom two atomic layers of the metal slab were fixed at their truncated bulk lattice positions, while all the remaining metal atoms as well as the adsorbate atom(s) were allowed to fully relax. Adsorption was allowed on only one side of the metal slab, and the electrostatic potential was adjusted accordingly.^{20,21} Any pair of successive slabs in the surface norm direction were separated by a vacuum layer of at least 12 Å in thickness. The calculated bulk lattice constants for Pd and Cu are 3.886 Å and 3.568 Å, respectively, which are in good agreement with the experimental values of 3.890 Å and 3.615 Å, respectively.²² The calculated bulk lattice constant for PdH in its NaCl crystal structure is 4.079 Å, in close agreement with the experimental value of 4.090 Å.²³

For the study of CO adsorption at different surface coverages on Pd(111) and Cu(111), the two close-packed metal surfaces were each modeled using a four-layer slab periodically repeated in a (3 × 3) surface unit cell, which corresponds to a surface coverage of 1/9 monolayer (ML) when a single adsorbate is present in the unit cell. The PdH(111) and PdH_{comp}(111) surfaces were modeled using (3 × 3) slabs consisting of four PdH bilayers, with the bottom two bilayers being fixed at the truncated bulk lattice positions featuring the lattice constants of PdH and metallic Pd, respectively. The PdH_{xL}/Pd(111) surfaces were constructed by placing x (x = 1–3) layers of PdH bilayers pseudomorphically on top of the four-layer (3 × 3) Pd(111) slab with the bottom two Pd layers fixed. For each PdH slab model, both H and Pd terminations were evaluated. For the PdH_{xL}/Pd(111) slabs, all possible PdH bilayer stacking sequences were examined and the lowest-energy one was identified and used for subsequent adsorption studies. The minimum energy structures of all the PdH slab models are shown in Figure S21. The first Brillouin zone of the (3 × 3) unit cell was sampled with a (4 × 4 × 1) Monkhorst-Pack k-point mesh.²⁴

The twin boundary regions on the Cu nanocrystals were modeled using a similar slab geometry as adopted in our previous studies for icosahedral nanocrystals (Figure S31),^{25,26} which

is consistent with the atomic stacking first reported by Mackay.²⁷ The slab consists of two four-layer (111) terrace regions, each consisting of six atomic rows, jointed by a twin-boundary edge (grey atoms in Figure S31). The slab is arranged in a (1×2) unit cell geometry (dashed lines in Figure S31), for which the first Brillouin zone was sampled using a $(1 \times 6 \times 1)$ Monkhorst-Pack k-point mesh. To compare the adsorption properties of the Cu twin boundaries with those on the (111) terrace of Cu, we also constructed a four-layer (4×2) Cu(111) slab. We previously demonstrated that this (4×2) unit cell size offers a reasonable comparison at similar surface coverage with the aforementioned Cu twin-boundary model.²⁵ The first Brillouin zone of the (4×2) unit cell was sampled with a $(4 \times 6 \times 1)$ Monkhorst-Pack k-point mesh.

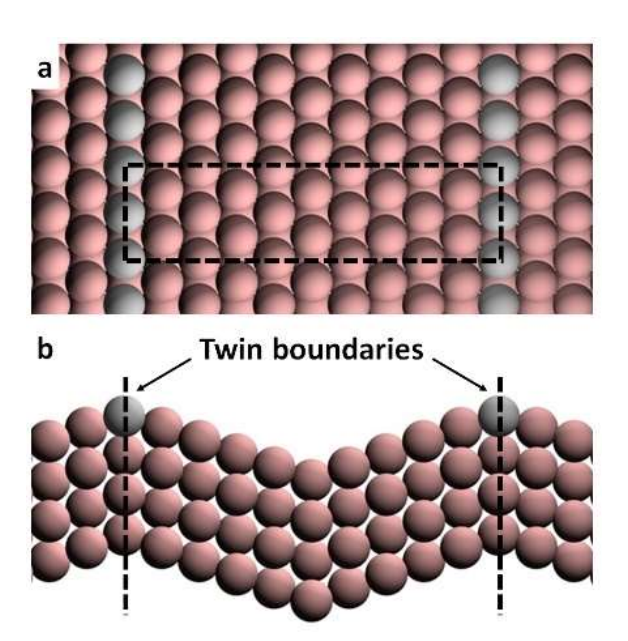


Figure S31. (a) Top and (b) side views of the Cu twin boundary slab model. Grey spheres denote the Cu atoms in twin boundary. Pink spheres denote the remaining Cu atoms. Dashed lines denote the (1×2) surface unit cell.

When a single adsorbate is present in each unit cell, we define the binding energy (BE) of this species as:

$$BE = E_{slab+species} - E_{slab} - E_{species(g)}$$

where, $E_{\text{slab+species}}$ is the total energy of the slab with the species adsorbed on its surface, E_{slab} is the total energy of the slab in the absence of any adsorbate, and $E_{\text{species}(g)}$ is the total energy of the species itself isolated in the gas phase. For adsorption studies on the PdH slab models, we

examined the adsorption on both the H- and Pd-terminated surfaces. E_{slab} , however, is always defined as the total energy of the minimum energy slab geometry (H-terminated) as shown in Figure S21. For the high-coverage CO adsorption studies, the average binding energy (BE_{avg}) when n CO molecules are adsorbed in each unit cell is defined as:

$$BE_{avg} = (E_{slab+nCO} - E_{slab} - nE_{CO(g)}) / n$$

where $E_{\text{slab+}n\text{CO}}$ is the total energy of the slab with n CO molecules adsorbed on its surface, and $E_{\text{CO(g)}}$ is the total energy of an isolated CO molecule in the gas phase. The differential binding energy (dBE) of CO is defined as the energy change induced by adding the nth CO molecule to a unit cell where n-1 CO molecules are already adsorbed on the slab, using the following equation:

$$dBE = E_{slab+nCO} - E_{slab+(n-1)CO} - E_{CO(g)}$$

Procedures for Constructing Pourbaix Phase Diagram. The free energy of a system with n CO molecules adsorbed on Pd(111) is evaluated by assuming the following electrochemical equilibrium (* denotes an empty surface site or an adsorbed species):

$$nCO_2(aq) + 2nH^+ + 2ne^- + * \leftrightarrow nCO^* + nH_2O(1)$$

The free energy (Ω) is then calculated as the Gibbs free energy of reaction for the equilibrium above:

$$\Omega = \mu_{nCO*}^0 + n\mu_{H_2O(l)}^0 - n\mu_{CO_2(aq)}^0 - 2n\mu_{H^+} - 2n\mu_{e^-} - \mu_*^0$$

where μ_X^0 denotes the standard chemical potential of Species X.

By the definition of RHE, at 0 V_{RHE}, the Gibbs free energy of reaction for the electrochemical equilibrium $H^+ + e^- \leftrightarrow 0.5 H_2(g)$ is zero at any pH. Therefore, the chemical potential of a proton-electron pair can be expressed in terms of the applied potential vs. RHE (U_{RHE}) as:

$$\mu_{H^+} + \mu_{e^-} = 0.5 \mu_{H_2(g)}^0 - e U_{RHE}$$

Note that this expression is independent of the pH value.

The chemical potential of CO₂(aq) is estimated using its Henry's constant of 0.034 mol/kg/bar at the standard condition.²⁸

$$\mu_{CO_2(aq)}^0 = \mu_{CO_2(g)}^0 + \Delta G_{solv}^0 = \mu_{CO_2(g)}^0 - \text{RTln}\left(H\frac{p_0}{c_0}\right)$$

where p_0 and c_0 denote the reference state for pressure (1 bar) and concentration (1 mol/kg), respectively.

The standard chemical potential of Species X is computed from its calculated energy using density functional theory (DFT) (E_{DFT}) at 0 K using:

$$\mu_X^0(T) = E_{DFT} + ZPE + H^0(T) - H^0(0K) - TS^0$$

where ZPE is the zero-point energy from DFT, and H^0 and S^0 are the standard enthalpy and entropy, respectively.

For gas-phase and liquid-phase species, H^0 and S^0 were obtained from the NIST database.²⁸ For the surface species (adsorbed CO), the temperature-dependent H^0 and S^0 values were derived

from the vibrational frequency values calculated at 1/9 ML CO coverage. The standard chemical potential of the clean Pd(111) slab (μ_*^0) was assumed constant at the calculated DFT total energy value for the entire four-layer slab in a (3 × 3) surface unit cell.

Adsorption of CO₂ Reduction Intermediates on Cu Twin Boundaries vs. Terrace. To further explore the role of under-coordinated sites at the Cu twin boundaries (Cu_{TB}) in the nanocrystals, we performed DFT calculations and compared the binding strength of common CO₂ reduction intermediates on Cu_{TB} with those on terrace Cu(111) sites. Seven strongly bound intermediates, namely, H, CO, OH, CH, CHO, COH, and CH₃O, were considered in this study. The preferred binding sites and the respective binding energies of these seven species on Cu_{TB} and Cu(111) are summarized in Table S9. For all the seven CO₂ reduction intermediates, we observed stronger binding on Cu_{TB} compared to Cu(111). It is worth noting that for CO and H, the binding energy difference between Cu_{TB} and Cu(111) is minimal (0.02 eV). For the other five species, the adsorption on Cu_{TB} is notably stronger, with binding energy differences ranging from 0.06 eV (for COH) to 0.23 eV (for OH). At room temperature, a difference of 0.06 eV in binding energy corresponds to one order of magnitude difference in the adsorption equilibrium constant. Therefore, under the reaction conditions, one would expect much higher coverages of OH, CH, and CH_xO_y species on Cu_{TB} than on Cu(111).

The higher surface coverage on the twin boundaries may lead to two possible scenarios for the following CO₂ reduction: (1) The under-coordinated sites on the twin boundaries are highly covered but remain active. In this case, the subsequent adsorption of C₁ intermediates on the twin boundaries becomes destabilized due to the high coverage, resulting in a reduced barrier for the C-C coupling and facilitating the formation of C₂₊ products. Examples of such coverage effects have been demonstrated previously in DFT studies for formic acid decomposition and Fischer-Tropsch synthesis.^{29,30} (2) The adsorption on the twin boundaries becomes so strong that the desorption of intermediates and even products is restricted, suppressing the activity of the catalysts. According to our experimental observations, the Pd-Cu truncated bitetrahedra with the largest size and lowest density of under-coordinated atoms on surface exhibited the highest current density (normalized to ECSA) toward the production of C₂₊ species, when compared to the pentagonal bipyramids and decahedra. This result suggested the detrimental role of undercoordinated atoms toward catalytic activity when they are presented in a very high proportion. A more explicit study of the twin-boundary effect would require the evaluation of the reaction kinetics for the C-C coupling steps as well as the diffusion of reaction intermediates from the twin boundary to the terrace, which is beyond the scope of this work.

Table S9. Comparison of energetically preferred structures of CO₂ reduction intermediates and their respective binding energies on Cu twin boundaries and on Cu(111) at the dilute limit (one adsorbate per unit cell).

| Species | Cu twin boundary | | | Cu(111) | | |
|---------|------------------|-----------------------|---------------------|---------|------------------|-------------------|
| | BE (eV) | | Site ^{a,b} | BE (eV) | | Site ^a |
| Н | -2.60 | hcp (TB) | S SO | -2.58 | fcc | |
| СО | -1.06 | fcc (TB) | | -1.04 | fcc | |
| СН | -5.26 | fcc (TB) | A SE | -5.12 | fcc | |
| ОН | -3.32 | bridge (TB) | | -3.10 | fcc | R. L. |
| СНО | -1.71 | tbt ^c (TB) | | -1.56 | tbt ^c | |
| СОН | -3.13 | fcc (TB) | | -3.06 | fcc | |
| CH₃O | -2.70 | hcp (TB) | | -2.52 | fcc | |

^a Insets show the top and side views of the preferred binding structures side by side. Color code: grey – twin boundary Cu atom; pink – other Cu atom; blue – H; black – C; red – O.

^b '(TB)' denotes a site which is either right on top of or adjacent to the twin boundary.

c 'tbt' denotes a binding structure across two adjacent top sites connected by a bridge site.

References

- (1) Wang, X.; Choi, S. Il; Roling, L. T.; Luo, M.; Ma, C.; Zhang, L.; Chi, M.; Liu, J.; Xie, Z.; Herron, J. A.; Mavrikakis, M.; Xia, Y. Palladium-Platinum Core-Shell Icosahedra with Substantially Enhanced Activity and Durability towards Oxygen Reduction. *Nat. Commun.* **2015**, *6*, 7594.
- (2) Wang, Y.; Shen, H.; Livi, K. J.; Raciti, D.; Zong, H.; Gregg, J.; Onadeko, M.; Wan, Y.; Watson, A.; Wang, C. Copper Nanocubes for CO₂ Reduction in Gas Diffusion Electrodes. *Nano Lett.* **2019**, *19*, 8461–8468.
- (3) Zhu, S.; Jiang, B.; Cai, W. B.; Shao, M. Direct Observation on Reaction Intermediates and the Role of Bicarbonate Anions in CO₂ Electrochemical Reduction Reaction on Cu Surfaces. *J. Am. Chem. Soc.* **2017**, *139*, 15664–15667.
- (4) Suen, N. T.; Kong, Z. R.; Hsu, C. S.; Chen, H. C.; Tung, C. W.; Lu, Y. R.; Dong, C. L.; Shen, C. C.; Chung, J. C.; Chen, H. M. Morphology Manipulation of Copper Nanocrystals and Product Selectivity in the Electrocatalytic Reduction of Carbon Dioxide. *ACS Catal.* **2019**, *9*, 5217–5222.
- (5) Liu, H.; Xiang, K.; Liu, Y.; Zhu, F.; Zou, M.; Yan, X.; Chai, L. Polydopamine Functionalized Cu Nanowires for Enhanced CO₂ Electroreduction towards Methane. *ChemElectroChem* **2018**, *5*, 3991–3999.
- (6) Weng, Z.; Zhang, X.; Wu, Y.; Huo, S.; Jiang, J.; Liu, W.; He, G.; Liang, Y.; Wang, H. Self-Cleaning Catalyst Electrodes for Stabilized CO₂ Reduction to Hydrocarbons. *Angew. Chem. Int. Ed.* **2017**, *56*, 13135–13139.
- (7) Kim, J.; Choi, W.; Park, J. W.; Kim, C.; Kim, M.; Song, H. Branched Copper Oxide Nanoparticles Induce Highly Selective Ethylene Production by Electrochemical Carbon Dioxide Reduction. *J. Am. Chem. Soc.* **2019**, *141*, 6986–6994.
- (8) Weng, Z.; Jiang, J.; Wu, Y.; Wu, Z.; Guo, X.; Materna, K. L.; Liu, W.; Batista, V. S.; Brudvig, G. W.; Wang, H. Electrochemical CO₂ Reduction to Hydrocarbons on a Heterogeneous Molecular Cu Catalyst in Aqueous Solution. *J. Am. Chem. Soc.* **2016**, *138*, 8076–8079.
- (9) Kim, D.; Lee, S.; Ocon, J. D.; Jeong, B.; Lee, J. K.; Lee, J. Insights Into an Autonomously Formed Oxygen-Evacuated Cu₂O Electrode for the Selective Production of C₂H₄ from CO₂. *Phys. Chem. Phys.* **2015**, *17*, 824–830.
- (10) Dutta, A.; Rahaman, M.; Luedi, N. C.; Mohos, M.; Broekmann, P. Morphology Matters: Tuning the Product Distribution of CO₂ Electroreduction on Oxide-Derived Cu Foam Catalysts.

- ACS Catal. 2016, 6, 3804–3814.
- (11) Li, Q.; Zhu, W.; Fu, J.; Zhang, H.; Wu, G.; Sun, S. Controlled Assembly of Cu Nanoparticles on Pyridinic-N Rich Graphene for Electrochemical Reduction of CO₂ to Ethylene. *Nano Energy* **2016**, *24*, 1–9.
- (12) Lyu, Z.; Xie, M.; Gilroy, K. D.; Hood, Z. D.; Zhao, M.; Zhou, S.; Liu, J.; Xia, Y. A Rationally Designed Route to the One-Pot Synthesis of Right Bipyramidal Nanocrystals of Copper. *Chem. Mater.* **2018**, *30*, 6469–6477.
- (13) Zhu, C.; Zeng, J.; Tao, J.; Johnson, M. C.; Schmidt-Krey, I.; Blubaugh, L.; Zhu, Y.; Gu, Z.; Xia, Y. Kinetically Controlled Overgrowth of Ag or Au on Pd Nanocrystal Seeds: From Hybrid Dimers to Nonconcentric and Concentric Bimetallic Nanocrystals. *J. Am. Chem. Soc.* **2012**, *134*, 15822–15831.
- (14) Kresse, G.; Furthmüller, J. Efficient Iterative Schemes for Ab Initio Total-Energy Calculations Using a Plane-Wave Basis Set. *Phys. Rev. B* **1996**, *54*, 11169–11186.
- (15) Kresse, G.; Furthmüller, J. Efficiency of Ab-Initio Total Energy Calculations for Metals and Semiconductors Using a Plane-Wave Basis Set. *Comput. Mater. Sci.* **1996**, *6*, 15–50.
- (16) Perdew, J. P.; Burke, K.; Ernzerhof, M. Generalized Gradient Approximation Made Simple. *Phys. Rev. Lett.* **1996**, *77*, 3865–3868.
- (17) Blöchl, P. E. Projector Augmented-Wave Method. *Phys. Rev. B* **1994**, *50*, 17953–17579.
- (18) Kresse, G.; Joubert, D. From Ultrasoft Pseudopotentials to the Projector Augmented-Wave Method. *Phys. Rev. B* **1999**, *59*, 1758–1775.
- (19) Grimme, S.; Antony, J.; Ehrlich, S.; Krieg, H. A Consistent and Accurate Ab Initio Parametrization of Density Functional Dispersion Correction (DFT-D) for the 94 Elements H-Pu. *J. Chem. Phys.* **2010**, *132*, 154104.
- (20) Neugebauer, J.; Scheffler, M. Adsorbate-Substrate and Adsorbate-Adsorbate Interactions of Na and K Adlayers on Al(111). *Phys. Rev. B.* **1992**, *46*, 16067–16080.
- (21) Bengtsson, L. Dipole Correction for Surface Supercell Calculations. *Phys. Rev. B* **1999**, *59*, 12301–12304.
- (22) Lide, D. R. CRC Handbook of Chemistry and Physics, 96th ed.; CRC Press: Boca Raton, FL, 2015.
- (23) Schirber, J. E.; Morosin, B. Lattice Constants of β -PdH_x and β -PdH_x with x near 1.0. *Phys. Rev. B* **1975**, *12*, 117–118.

- (24) Monkhorst, H. J.; Pack, J. D. Special Points for Brillouin-Zone Integrations. *Phys. Rev. B* **1976**, *13*, 5188–5192.
- (25) Zhao, M.; Xu, L.; Vara, M.; Elnabawy, A. O.; Gilroy, K. D.; Hood, Z. D.; Zhou, S.; Figueroa-Cosme, L.; Chi, M.; Mavrikakis, M.; Xia, Y. Synthesis of Ru Icosahedral Nanocages with a Face-Centered-Cubic Structure and Evaluation of Their Catalytic Properties. *ACS Catal.* **2018**, *8*, 6948–6960.
- (26) Gilroy, K. D.; Elnabawy, A. O.; Yang, T. H.; Roling, L. T.; Howe, J.; Mavrikakis, M.; Xia, Y. Thermal Stability of Metal Nanocrystals: An Investigation of the Surface and Bulk Reconstructions of Pd Concave Icosahedra. *Nano Lett.* **2017**, *17*, 3655–3661.
- (27) Mackay, A. L. A Dense Non-Crystallographic Packing of Equal Spheres. *Acta Crystallogr.* **1962**, *15*, 916–918.
- (28) Linstrom, P. J.; Mallard, W. G. *NIST Chemistry WebBook, NIST Standard Reference Database Number 69*, National Institute of Standards and Technology, Gaithersburg MD, **2017**.
- (29) Bhandari, S.; Rangarajan, S.; Maravelias, C. T.; Dumesic, J. A.; Mavrikakis, M. Reaction Mechanism of Vapor-Phase Formic Acid Decomposition over Platinum Catalysts: DFT, Reaction Kinetics Experiments, and Microkinetic Modeling. *ACS Catal.* **2020**, *10*, 4112–4126.
- (30) Ojeda, M.; Nabar, R.; Nilekar, A. U.; Ishikawa, A.; Mavrikakis, M.; Iglesia, E. CO Activation Pathways and the Mechanism of Fischer-Tropsch Synthesis. *J. Catal.* **2010**, *272*, 287–297.